DISSERTATION

MODEL EVALUATION USING SPACE-BORNE LIDAR OBSERVATIONS

Submitted by

Maike Ahlgrimm

Department of Atmospheric Science

In partial fulfillment of the requirements

For the Degree of Doctor of Philosophy

Colorado State University

Fort Collins, Colorado

Spring 2008

UMI Number: 3321252

INFORMATION TO USERS

The quality of this reproduction is dependent upon the quality of the copy submitted. Broken or indistinct print, colored or poor quality illustrations and photographs, print bleed-through, substandard margins, and improper alignment can adversely affect reproduction.

In the unlikely event that the author did not send a complete manuscript and there are missing pages, these will be noted. Also, if unauthorized copyright material had to be removed, a note will indicate the deletion.

UMI®

UMI Microform 3321252

Copyright 2008 by ProQuest LLC.

All rights reserved. This microform edition is protected against unauthorized copying under Title 17, United States Code.

ProQuest LLC
789 E. Eisenhower Parkway
PO Box 1346
Ann Arbor, MI 48106-1346

COLORADO STATE UNIVERSITY

December 13, 2007

WE HEREBY RECOMMEND THAT THE DISSERTATION PREPARED UNDER OUR SUPERVISION BY MAIKE AHLGRIMM ENTITLED MODEL EVALUATION USING SPACE-BORNE LIDAR OBSERVATIONS BE ACCEPTED AS FULFILLING IN PART REQUIREMENTS FOR THE DEGREE OF DOCTOR OF PHILOSOPHY.

Committee on Graduate Work

Wayne Schubert

David A. Krueger

Richard H. Johnson

D&S A. Randall

Adviser

Richard H. Johnson

Department Head

ABSTRACT OF DISSERTATION

MODEL EVALUATION USING SPACE-BORNE LIDAR OBSERVATIONS

In this study, the use of space-borne lidar observations for the comparison with, and evaluation of modeled clouds is explored. Four version of the ECMWF Integrated Forecast System and two versions of the Goddard Earth Observing System (GEOS-5) model are assessed for their ability to produce marine boundary layer clouds. The cause of some of the model deficiencies is investigated, and specific suggestions for improvements are made and tested. In order to do so, two cloud types are defined: a stratocumulus type (*Sc*), and a trade cumulus or transitional cumulus type (*TCu*). Samples in four oceanic regions are classified into those categories, and the frequency of occurrence, location, and properties of the samples compared between models and observations.

Both models have a tendency to produce clouds with small cloud fraction too frequently, and underestimate the occurrence of stratocumulus clouds. The ECMWF model underestimates the cloud top height of the stratocumulus clouds, while the GEOS -5 model produces an excess of fog. The introduction of an eddy diffusivity - mass flux boundary layer scheme in the ECMWF leads to an increase in stratocumulus clouds and a more realistic cloud-fraction distribution. Sensitivity tests show further improvement of the location and cloud top height of stratocumulus clouds when environmental mixing of the test parcel in the boundary layer is reduced, and less lower

level stability is required for generation of stratocumulus clouds. However, these improvements vary with region, indicating that the new parameterization cannot fully capture all the processes contributing to the generation of these clouds.

Improvement of the GEOS-5 model can also be demonstrated with a reduction of the fog.

In addition, Cloud-Aerosol Lidar and Infrared Pathfinder Satellite Observations provide an unprecedented global view of boundary-layer clouds, and illustrate the seasonal and diurnal cycles of low-cloud top height and frequency of occurrence in the subtropical belt. The cloud-top heights observed are generally consistent with previous ground-based observations of the inversion height.

Maike Ahlgrimm
Department of Atmospheric Science
Colorado State University
Fort Collins, CO 80523
Spring 2008

ACKNOWLEDGMENTS

Thanks, Dave! I truly appreciate all the opportunities I have had over the past six years, to meet other scientists, to travel and present my work, to learn. Thanks for taking a chance on a foreign student without a proper undergraduate degree or grades.

This work was made possible through the cooperation of the European Centre for Medium-Range Weather Forecasts and the Goddard Space Flight Center. In particular, I would like to thank Anton Beljaars, Martin Köhler and Martin Miller (ECMWF) for their collaboration. Caterina Tassone and Julio Bacmeister provided the model data from the Goddard Space Flight Center. Steve Palm, James Spinhirne, Dennis Hlavka and William Hart from the GLAS science team played a major role in helping me understand the GLAS retrieval algorithm, and working on the lidar simulator.

Many thanks also to Randall's Rabbits - you know who your are! Wish I could take you all with me.

This research was supported by NASA Contract NNG04GI25G (IDS), NSF Cooperative Agreement ATM-0425247 (CMMAP), DOE Cooperative Agreement DE-FC02-01ER63163, NOAA Contract NA17RJ1228, NASA Grant NAG5-11737 (CAPE), NASA Contract NNG06GB41G (CEAS fellowship).

TABLE OF CONTENTS

LIST OF TABLES

LIST OF FIGURES

Chapter 1: Introduction

History of space-borne lidars

Lidar observations from space have only recently become available. In 1994, the space shuttle "Discovery" carried a lidar in orbit for eleven days during the Lidar In-space Technology Experiment (LITE). The experiment provided a first data set, though for a rather short period (Winker et al., 1996). In January of 2003, the Ice, Cloud and Land Elevation Satellite (ICESat) was launched with the Geoscience Laser Altimeter System (GLAS) onboard. GLAS consisted of three redundant lidars, which were supposed to provide continuous coverage for three to five years. Unfortunately, equipment malfunction led to an early demise of the first lidar, and rapid power loss of the remaining two lidars. In order to extend the duration of the mission, the science team decided to switch the remaining lidars on for a few weeks only, several times a year. The atmospheric data of highest quality was retrieved during laser period 2A (L2A) in the fall of 2003. The retrieval algorithm has been optimized over many generations and provides very good secondary data products for this period.

Since May 2006, GLAS is no longer the only lidar in space. The Cloud-Aerosol Lidar and Infrared Pathfinder Satellite Observation (CALIPSO) satellite, and the CloudSat radar where launched together and have been providing observations for over a year now. In contrast to GLAS, CALIPSO provides data for a long period of time, spanning all seasons. In this study, we will be using both GLAS and CALIPSO observations.

What is new about lidars?

The lidar adds a new dimension to the already existing suite of passive satellite observations, namely a high vertical resolution with unprecedented accuracy, detection of multiple cloud layers and the ability to detect layers with very low optical thickness. In contrast to passive retrievals, the lidar detects layer heights directly, with a nominal vertical resolution of 76.8 m (GLAS) and 30 m (CALIPSO).

The vertical location of clouds is usually inferred from passive observations by using a combination of visible and infrared channels, and is limited to the topmost layer. The retrieval uncertainty is often in the hundreds of meters for a variety of reasons: a difficulty in separating multiple clouds at various heights in the same scene, isothermal regions in the atmospheric profile (in cases where cloud top temperature is compared with the environmental sounding to estimate cloud top height), and weak signal-to-noise ratio (CO2 slicing in the lower atmosphere) [Naud et al., 2005; Menzel et al., 2006; Wielicki and Coakley, 1981]. For semi-transparent cirrus clouds, passive sensors will often miss the high cloud and retrieve a lower cloud with stronger signal instead.

Strengths of the lidar

The lidar on the other hand is sensitive to an optical depth as low as 0.02 (Spinhirne et al., 2005) and is ideally suited for the retrieval of high, optically thin cirrus. The algorithms used to differentiate between aerosol layers and cloud layers are quite reliable (Spinhirne et al., 2005), even where clouds occur embedded in aerosol layers (Hart et al., 2005).

The lidar's ability to observe multiple cloud layers provides valuable statistics on cloud overlap (Wang and Dessler, 2006). The resolution of general circulation models

(GCMs) is too coarse to resolve small, individual clouds. As a result, assumptions about overlap have to be made. The lidar provides an unprecedented opportunity to evaluate overlap assumptions with global observations.

As briefly mentioned above, passive satellite observations of cloud top height suffer from a variety of problems. A comparison of the lidar retrievals with observations from passive instruments can be a valuable tool for improvement of the passive retrievals (e.g. Mahesh et al., 2004 and Wylie et al., 2007).

Another great, but less obvious quality of the lidar is its ability to detect the top of the boundary layer. Turbulence in the boundary layer carries aerosols and near-surface moisture upward, typically to the top of the boundary layer. The lidar can detect the gradient in particle concentration at the boundary layer top. For the first time, global observations of the boundary layer height are available. In the past, observations were ground based, and consequently limited to populated areas (i.e. land, individual ship tracks).

Limitations of the lidar

The lidar also has some inherent weaknesses. Its penetration depth is limited to an optical thickness of 3 to 4, for example. Most water clouds will fully attenuate the signal such that lower level clouds are missed. The near polar, sun-synchronous orbit of both ICESat and CALIPSO results in twice daily overpasses at the same approximate local time. This is insufficient to thoroughly sample the diurnal cycle, for example. The lidar's ground track is very narrow (around 70 m for GLAS), so the lidar actually observes only a very small fraction of the Earth's atmosphere. It is quite difficult to identify organized cloud systems, such as fronts or large convective systems from the

narrow lidar track alone. Because of the slow repeat orbit (180 days for GLAS), it is almost impossible to track the development of any individual cloud or system.

Levels of model evaluation

There is a range of levels at which lidar observations and model data can be compared. At one end of the spectrum, the raw backscatter can be compared to simulated backscatter from the model. At the other end, secondary lidar products can be averaged to fit the model grid, to be compared directly to the model properties.

Working with the backscatter allows more insight into the microphysical properties of the modeled clouds. The comparison will show whether the microphysical parameterizations in the model lead to the same radiative properties (at least in the visible range) as in the observations. This method has also the advantage of avoiding errors introduced by inverting the lidar backscatter to obtain secondary products, and signal attenuation is accounted for. At this end of the spectrum, the greatest errors are introduced by outright model errors in the placement and amount of clouds, the clouds' microphysical properties (e.g. particle size and concentration) as well as through imperfect simulation of the resulting backscatter.

On the other hand, the observations can be recast onto the model grid and compared directly to model properties, which are well known. Here, the greater error is likely introduced through uncertainties in the lidar retrieval algorithm and through the averaging process. Depending on the focus of the comparison, a point somewhere between these extremes will probably lead to the best results.

Previous lidar-to-model comparisons

Chepfer et al. (2007) use a lidar forward model previously tested with ground-based lidar observations (Chiriaco et al., 2006) to evaluate the NCAR Mesoscale Model's (MM5) ability to produce optically thin clouds over Europe. The raw GLAS backscatter observations over Europe are averaged for October 2003 and compared to simulated backscatter from the MM5 for the same area and time period. The MM5's averaged backscatter profile shows an overestimation of backscatter above 6 km height, but a lack at lower levels. The authors then use a simple backscatter threshold to identify the existence of clouds in the profile in order to investigate whether the discrepancies in the backscatter profile are a result of overestimation (underestimation) of cloud amount, or cloud optical thickness. The model apparently produces too few optically thin high clouds, but too many clouds with high optical depth above 6 km. The interpretation of the results for lower clouds is difficult, since the excess of optically thick high clouds in the model masks many of the lower clouds. The authors also suggest some possible sources of error in the MM5 and lidar forward model that may have led the these results.

Wilkinson et al. (submitted to *Mon. Wea. Rev.*) use a similar lidar forward model to compare fifteen days of GLAS observations to simulated backscatter profiles from the ECMWF model in zonally averaged latitude bands. A tendency to produce an overabundance of ice clouds is found. Another interesting result from this study is that the skill score for the correct prediction of clouds is best between 5 km and 10 km, but decreases significantly below and above. The authors estimate the error resulting from uncertainties associated with the parameter choices in the lidar forward model to be approximately 10%.

Both of theses studies are quite valuable. However, they address primarily clouds in the mid- and upper troposphere, since many lower clouds attenuate the lidar signal. Using the lidar forward model introduces uncertainties associated with the cloud overlap assumptions made, which are not discussed. While the MM5 distinguishes between snow, ice and liquid, the ECMWF model only accounts for one liquid and one ice phase. Neither model can account for the many ice species and habits that have been observed in ice clouds, and both assume that Mie theory applied to ice spheres can adequately describe the scattering behavior of the ice particles. The study of Chepfer et al. 2007 tries to make a connection between the model's thermodynamic conditions and the resulting backscatter behavior, but the conclusions are rather general. The simple backscatter threshold used by the authors is much less sophisticated than the GLAS retrieval algorithm, introducing additional uncertainty in the estimate of cloud amount and placement.

Miller et al. (1999) use a different approach comparing the nighttime LITE observations to the ECMWF model. Here, clouds in the backscatter profile were detected using a more sophisticated signal-to-noise algorithm and were then averaged onto the model grid. The model's ability to generate clouds at the right time and place is tested with a skill score that counts the cases of coincident cloud occurrence of each grid box in model and observations. However, this method does not evaluate whether the microphysical or macrophysical (i.e. cloud fraction) properties of the observed clouds agree. Neither does it account for the signal attenuation that would occur, where the lidar to observe the model clouds.

Palm et al. (2005) use the GLAS backscatter to calculate a cloud fraction to compare to the ECMWF model. As in Wilkinson et al. (submitted to *Mon. Wea. Rev.*), this study finds that the model overestimates the amount of high clouds. In addition, the authors find that the model's skill score drops with increased forecast time, and the overestimation of high clouds worsens.

Of the ECMWF model comparisons mentioned here, none address possible causes of the model's weaknesses, or make concrete suggestions for improvement of the model performance.

Focus of this study

This study focusses on the lidar's ability to provide accurate, global observations of the clear and cloudy boundary layer over ocean. Apart from a brief first glance at the GLAS-retrieved boundary layer in Palm et al. (2005), this aspect of the GLAS observations has been barely addressed, in contrast to the number of studies concentrating on high clouds (Dessler et al., 2006a and various papers cited above). Focussing on this particular regime has many advantages: Marine boundary layer clouds are very persistent and cover large areas that are quite well known. Thus, the lidar has many opportunities to observe these clouds. The clouds are optically thick, producing a very strong signal at the cloud top, not easily mistaken for aerosol, and adding to the confidence of the retrieval due to a large signal-to-noise ratio. Optically thick high clouds are rarely found above marine boundary layer clouds, minimizing errors due to cloud masking.

Not only are marine boundary layer clouds well observed by lidar, they have also a profound impact on the Earth's radiative balance. They provide a net-cooling effect by

reflecting the incoming sunlight, while radiating energy to space very efficiently. Since the ocean has very low albedo, a lack of these clouds, or in case of a model, under-prediction of these clouds, can lead to a significantly altered radiative balance. Yet, many current GCMs cannot predict the horizontal extent and vertical location of marine boundary layer clouds correctly (Jakob, 1999; Duynkerke and Teixeira, 2001; Chevallier et al., 2001).

Understanding and modeling the marine boundary layer and associated clouds is not a trivial matter. A variety of observational studies have provided insights into the cloud regimes commonly found in the subtropical oceans, such as stratocumulus [East Pacific Investigation of Climate Experiment (Bretherton et al. 2004), First and Second Dynamics and Chemistry of Marine Stratocumulus field studies (Lenschow et al., 1988 and Stevens et al., 2003), FIRE 1 Marine Stratocumulus Intensive Field Observations (Minnis et al., 1992)] and trade cumulus regimes [Atlantic Trade Wind Experiment (Augstein et al.,1973), Rain in Cumulus over Ocean Experiment, (Rauber et al., submitted to *Bull. Amer. Meteor. Soc.*)], as well as the transition between these regimes [Atlantic Stratocumulus Transition Experiment, (Albrecht et al., 1995)]. This has lead to a better understanding of these regimes, but it remains a challenge to encapsulate all the turbulent and convective processes forming the marine boundary layer and clouds in the form of parameterizations. Most GCMs use separate parameterizations to represent boundary layer processes, shallow and deep convection. However, cloud formation, particularly in the stratocumulus regime, is closely connected to the boundary layer processes.

The goal of this study is to assess the abilities of two models to correctly forecast marine boundary layer clouds. We will also try to understand the cause of the model deficiencies, make specific suggestions for improvement and test the outcome of the changes made.

Overview

In the following two chapters, the lidar observations, as well as the two models discussed in this study will be described. The lidar forward model adapted from Chiriaco et al. (2006) and used here is shown in Chapter 4. Chapter 5 of this study uses the unique cloud layer observations from GLAS to evaluate the ability of two models to generate marine boundary layer clouds. In Chapter 6 we take advantage of CALIPSO's longer record to examine seasonal changes in the boundary layer clouds.

Chapter 2: Observational data

The data used in this dissertation are primarily observations of clouds and the boundary layer (BL) by space-borne lidar. Following are brief descriptions of these observational datasets, focussing on their use in this work. More detailed information can be found in the Appendix.

2.1. Geoscience Laser Altimeter System (GLAS) observations

The Geoscience Laser Altimeter System is a dual-frequency lidar onboard the Ice, Cloud and Land Elevation Satellite (ICESat). It was launched in January of 2003 with three lasers on board. Unfortunately, the first laser failed quickly. During the period from September 25th 2003 to November 8th 2003 (period L2A), the second laser performed well and with enough power to produce good observations of tenuous clouds and aerosols at the shorter of the two observational wavelengths (532 nm). The cloud layer and boundary layer height products from this period are used in this study (Zwally et al., 2003a and 2003b).

The primary task of ICESat is the monitoring of the polar ice caps. Accordingly, the satellite's orbit has good coverage in the near-polar regions, but is not as well suited to observations in the tropical belt. The repeat orbit is 180 days, too long to re-sample the same site within the L2A period. Overpasses occur around 7 am and 7 pm at the Equator, which makes it difficult to observe the diurnal cycle. Additionally, the priority for the ice monitoring project is to observe the ice caps over as long a period of time as

possible. With the rapid decline of the three lasers, the science team decided to switch the lasers off in between short observational periods, and to operate the lasers at lower power. The data from L2A remains the best available for cloud and aerosol observations.

Despite these issues, the observations from GLAS are an exciting new data set. The cloud-layer product provides cloud-base and -top heights for up to ten layered clouds, with an accuracy between 78 m and 156 m under most circumstances. The optical depth of thin clouds (up to optical depth 3) can be estimated, and under most circumstances, the BL height can be observed using the aerosol gradient across the BL top as a proxy.

A more detailed description of the retrieval algorithms for these data products, as well as the horizontal resolution of the different products is provided in the Appendix.

2.2. Cloud-Aerosol Lidar and Infrared Pathfinder Satellite Observations (CALIPSO)

The Cloud-Aerosol Lidar and Infrared Pathfinder Satellite Observation (CALIPSO) satellite represents the next generation of space-borne lidar observations. The satellite is part of the Earth Observing System's A-train constellation, in which five satellites with various instruments orbit the Earth only minutes apart. The A-train, or afternoon-train, crosses the Equator around 1:30 PM and 1:30 AM local time in its ascending and descending tracks, respectively. The Cloud-Aerosol Lidar with Orthogonal Polarization (CALIOP) operates at 532 nm and 1064 nm wavelengths, same as GLAS, but has two channels at 532 nm wavelength to observe the orthogonally polarized components of this wavelength. The lidar operates at 20.25 Hz, about half the frequency of GLAS, which

leads to a horizontal spacing of footprints of 333m. The vertical resolution is 30 m to 60 m, which is more accurate than GLAS' vertical resolution.

CALIPSO was launched in May 2006, and observations are available starting mid-June 2006. In this study, data from the months of July and October 2006, as well as January and April 2007 are used. The data product of choice is the Lidar Level 2, 5 km cloud layer product, V1-10. Similar to GLAS, the backscatter profiles in this product have been averaged to a horizontal resolution of 5 km (comparable to LR in GLAS) in order to provide better signal-to-noise ratios. This resolution was chosen over a higher resolution (1 km or 1/3 km) because at the time this work was done (Spring 2007), flags indicating signal attenuation were only available at 5 km resolution. Only the cloud-top and -base altitude information, as well as the attenuation flag, were used from this product. This may not do justice to the suite of additional data products available from CALIPSO, but the goal here is to use the observations as an extension of the GLAS observations, keeping the two data sources as comparable as possible.

Chapter 3: Model data

3.1. Integrated Forecast System (IFS) of the European Centre for Medium-Range Weather Forecasts (ECMWF)

The model runs presented in this work were created by the ECMWF's Integrated Forecast System (IFS) in the cycle configurations CY28R3 and CY29R1. The data were kindly provided by Martin Köhler at the ECMWF. The runs have the same semi-Lagrangian dynamical core and differ only in the boundary layer (BL) parameterization schemes. A more detailed description of the BL parameterizations and convective schemes can be found in Appendix B. To summarize briefly, run CY28R3 employs a dry diffusive boundary layer scheme and three convective parameterizations for shallow, deep and mid-level convection.

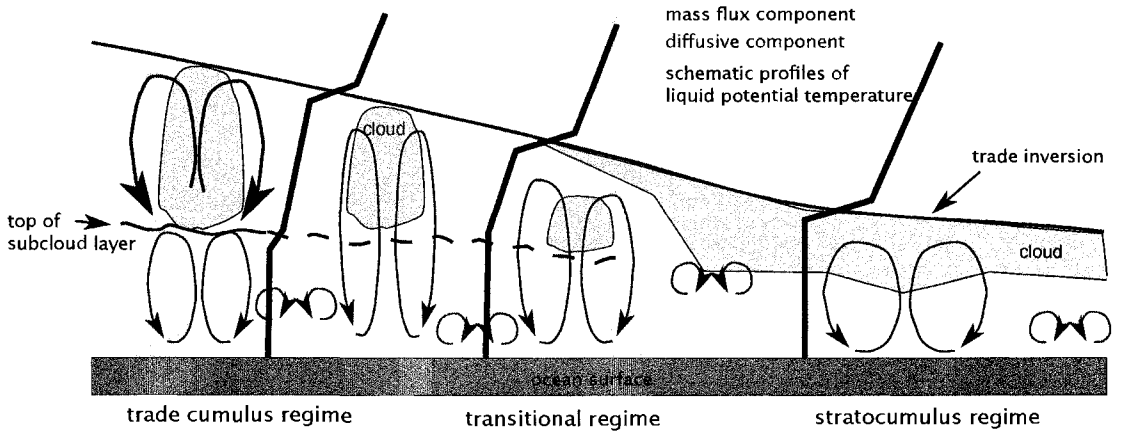

Fig. 3.1 Schematic of marine boundary layer. Blue arrows indicate the effect of the mass flux component in the EDMF scheme: mixing throughout the depth of the layer. Red arrows indicate the diffusive component of the scheme: down-gradient local mixing. The typical liquid water potential temperature (θ_l), a moist-conserved variable in the absence of precipitation, is shown on green for profiles typical in the various regimes.

CY29R1 and variations thereof use a newer eddy diffusivity - mass flux (EDMF) boundary layer scheme with moist-conserved variables (Fig. 3.1). The diffusive component of this scheme handles the down-gradient mixing of local properties, while the mass-flux component carries near-surface properties throughout the depth of the layer, mimicking the effect of large eddies. The EDMF scheme is better equipped to handle the variety of situations encountered in the subtropical oceans, from the well-mixed cloud capped stratocumulus regime to small trade cumuli decoupled from the subcloud layer. The use of moist-conserved variables allows the scheme to treat the moisture content of the air as an integral part of the boundary layer processes. As a result, the scheme "knows" the saturation state of the air and can produce stratocumulus-type clouds when the lower atmosphere is sufficiently moist and stable, as is the case over the subtropical eastern ocean basins. The convective parameterizations are the same as in the previous run, except that a cloudy boundary layer produced by the EDMF prohibits shallow or deep convection in the same model column.

The model is run on a reduced Gaussian grid (Hortal and Simmons, 1991) at T511 resolution. On the reduced Gaussian grid, the number of grid points around a latitude circle decreases towards the pole, such that the zonal distance between grid points remains approximately constant from Equator to pole. Resolution "T511" refers to the triangular truncation of the spherical harmonics at wave number 511, and is equivalent to approximately 40 km grid spacing. The model data are then mapped onto a 1°×1° latitude-longitude grid, using nearest-neighbor resampling. Documentation on the IFS can be found on the ECMWF website (http://www.ecmwf.int).

3.2. Goddard Earth Observing System Model, Version 5 (GEOS-5)

The GEOS-5 model has a finite-volume dynamical core (Lin and Rood, 1996). Clouds and convection are represented through the relaxed Arakawa-Schubert (RAS) scheme (Moorthi and Suarez, 1992) and the prognostic stratiform cloud scheme of Bacmeister et al. (2006).

The moist physics parameterization works as follows: The RAS scheme calculates the mass flux for a sequence of convective plume types. Each plume type detrains mass and cloud condensate, and adjusts the environmental profiles of temperature, moisture and horizontal wind. Then the large-scale prognostic parameterization for stratiform clouds is called to determine cloud fraction and condensate, using an assumed PDF shape. The scheme distinguishes between "anvil" clouds, whose source is detrainment form the RAS plumes, and "large-scale" clouds, the source of which is the large-scale grid box moisture. Evaporation, auto-conversion, sedimentation of frozen condensate and accretion of falling precipitation then act on the condensate, regardless of its source.

Radiation follows Chou and Suarez (1999). The land-surface interaction is modeled using the catchment-based scheme described in Koster et al. (2000). The boundary layer is modeled using the scheme of Lock et al. (2000). This scheme uses moist-conserved variables. Here, the buoyancy of an undilute test parcel lifted from the surface, and lowered from the cloud top (in cases where layer clouds exist) is used to identify stable and unstable regions in the atmosphere. Well-mixed layers are then treated using the scheme of Holtslag and Boville (1993) in which the profile shape of the layer is prescribed, and the strength of the layer-deep mixing is related to the strength of the surface fluxes, as well as radiative and evaporative cooling a the top of the layer (in

cloudy cases). In cases where the boundary layer is not well mixed and cumulus convection is present, the mass flux scheme of Gregory and Rowntree (1990) is used instead.

Chapter 4: GLAS simulator

One aspect of the lidar observations that introduces problems in a comparison with model data is signal attenuation. Parts of the atmosphere remain unsampled by the lidar due to overlying optically thick clouds. This poses the question: how can quantitative measures of cloud occurrence be compared between the two data sources, considering that the lidar leaves certain areas of the atmosphere unsampled? One solution to this problem is to simulate the backscatter that the lidar would observe were it to investigate the modeled atmosphere. How cloud particles scatter the light emitted by the lidar varies with the microphysical properties of the cloud. In the model, clouds are described by bulk variables, such as cloud liquid water content (CLWC), cloud ice water content (CIWC) and cloud fraction (CF). In order to translate these bulk properties into microphysical properties, a number of assumptions have to be made. Chiriaco et al. (2006) and Wilkinson et al. (submitted to *Mon. Wea. Rev.*) both use versions of a lidar forward model to simulate model backscatter for comparison with GLAS. To date, no CALIPSO simulator exists, though the principles are the same as for GLAS, and the forward model can be easily adapted for CALIPSO. Currently, a combined CALIPSO, CloudSat and ISCCP simulator ("CICCS") is under development as part of the Cloud Feedback Model Intercomparison Project - Phase 2 (CFMIP-2).

The lidar simulator used here is based on the equations outlined by Chiriaco et al. (2006), with some modifications. Instead of the particle size distributions described in

the paper, the same assumptions are made as in the ECMWF short wave scheme. The simulated normalized backscatter signal in $m^{-1}sr^{-1}$ is

$$P(z)z^2 = [\beta_{mol}(z) + \beta_{par}(z)]\exp\left\{-2\int_0^z \left[\eta\alpha_{par}(z') + \alpha_{mol}(z')\right]dz'\right\} \tag{4.1}$$

Indices *mol* and *par* refer to molecular (i.e. air molecules) and particular (i.e. cloud droplet) properties. Alpha (α) is the attenuation, β is the backscatter coefficient. Following Collis and Russel (1976), the molecular backscatter can be approximated using the following equation, which is based on Rayleigh theory:

$$\beta_{mol}(z) = \frac{p(z)}{kT(z)} 5.45 \times 10^{-32} \left[\frac{\lambda(\mu m)}{0.55}\right]^{-4.09} m^2 sr^{-1} \tag{4.2}$$

where k=1.38·10^{-23}J/K is the Boltzmann constant, p is pressure in Pa and T is temperature in Kelvin.

The effective size of ice particles in clouds needs to be estimated in order to convert the model-generated CIWC into a number concentration of ice particles. Ou and Liou (1995) have empirically related quasi-spherical ice effective size with temperature:

$$r_i = 326.3 + 12.42T + 0.197T^2 + 0.0012T^3 \tag{4.3}$$

where T is temperature in degrees Celsius and r_i is the effective ice radius in μm. The ice particle density in m^{-3} can then be determined from CIWC assuming spherical ice particles:

$$N_i = \frac{CIWC\rho_{air}}{\frac{4}{3}\pi\left(r_i \times 10^{-6}\right)^3 \rho_{ice}} \tag{4.4}$$

CIWC is cloud ice water content in kg/kg. It is multiplied with air density at each model level to get ice water content per volume. The ice density ρ_{ice} is chosen to be the solid

ice density 917 kg m^{-3}. The ice effective size ($r_{i)}$ is still in μm. The factor of 10^{-6} converts it to m.

The ECMWF microphysics assume droplet size to be linear with pressure, with 10μm at the surface, linearly increasing to 45μm at the top of the atmosphere. The drop number concentration can then be calculated similar to the one for ice, also assuming sphericity.

Following the Chiriaco paper, the absorption by particles α_{par} is the sum of the absorption of ice and liquid particles, which can be calculated as:

$$\alpha_{l/i} = \pi r_{l/i}^2 Q N_{l/i} \tag{4.5}$$

where Q is the particle scattering efficiency, which is approximately equal to 2 at 532nm (Ulaby et al. 1943). The multiple scattering correction parameter is taken to be η=0.5 (Platt 1973).

Molecular absorption is

$$\alpha_{mol} = \frac{\beta_{mol}}{0.119} \tag{4.6}$$

The GLAS algorithm uses a fixed backscatter-to-extinction ratio for water, and a function of temperature for ice:

$$S_l = 17.8 \tag{4.7}$$

$$S_i = 2.4385777 \times 10^{-3} T^2 - 0.43187856T + 12.961138 \tag{4.8}$$

where T is temperature in degrees Celsius.

The backscatter coefficients can then be calculated from the extinction coefficients (or absorption) above:

$$\beta_{l/i} = \frac{\alpha_{l/i}}{S_{l/i}} \tag{4.9}$$

While the lidar equation itself accurately describes the radiation's behavior, a number of assumptions about the model clouds' microphysics must be made. For example, sphericity of ice particles is assumed and particle sizes are approximated by simple linear functions. These assumptions introduce uncertainties in the resulting backscatter. Wilkinson et al. (submitted to *Mon. Wea. Rev.*) test the sensitivity of some of these parameters and find that changes in backscatter intensity and cloud fraction for clouds below 5 km is generally small. In any case, the simulator is used in this study only to determine the level of full signal attenuation. Small errors in the backscatter will probably not alter the level of attenuation much since the signal of the attenuated cloud is very strong.

A stochastic method for determining cloud overlap (Räisänen et al., 2004) is used to find the same number of subcolumns within a model grid column as there are HR GLAS lidar shots.

Chapter 5: Model evaluation

As stated in the introduction, the goal of this study is to assess the abilities of two models to correctly forecast marine boundary layer clouds. We will also try to understand the cause of some of the model deficiencies and make specific suggestions for improvement and test the outcome of the changes made.

Marine stratus clouds exist primarily in the eastern ocean basins. Trade cumulus clouds are much more widely distributed throughout the oceans, but are ubiquitous just to the west of the marine stratocumulus decks. A number of processes combine to maintain these persistent clouds. Subtropical high pressure centers are located to the west of the continents, driving the ocean current equatorward along the coastlines. Ekman transport leads to upwelling of cool waters along the coast. The high pressure regions are part of the descending branch of the Hadley cell and are areas of weak subsidence. The subsiding air is very dry due to its origin near the tropopause, and warms dry-adiabatically as it sinks. The turbulent boundary layer over cool sea surface temperatures (SSTs) meets the free tropospheric air at the trade inversion, so called due to the temperature inversion marking the interface of the two air masses. The depth of the boundary layer is maintained against the free-tropospheric subsidence through entrainment across the inversion. Turbulence at the boundary layer top captures pockets of free-tropospheric air, which are carried down into the boundary layer where they are cooled and moistened by heat and moisture flux divergence that is concentrated near the boundary layer top.

Close to the coasts, the trade inversion is strong, and the ocean temperatures are coolest. Here, the boundary layer is typically well-mixed to the inversion. The air saturates below the inversion, leading to persistent stratocumulus clouds under the inversion (stratocumulus regime). Radiative cooling at the cloud top helps maintain the layer-deep mixing.

Further away from the coast, the trade inversion is weaker and higher, and the ocean temperatures are warmer. Trade cumulus clouds are common (trade cumulus regime), but due to their small size make up only a relatively small cloud fraction. The subcloud layer is still well mixed, but a layer with slightly negative buoyancy near the cloud base separates it from the less well-mixed cloud layer above. Most cumuli grow to the trade inversion, but some have enough buoyancy to penetrate it.

In the transition region from stratocumulus to trade cumulus, cumulus-under-stratocumulus clouds are often observed. The details of how and under what conditions the stratus deck breaks up are still under investigation (Albrecht et al., 1995; Norris, 1998; Krueger et al., 1995; Ciesielski et al., 1999; Ciesielski et al., 2001).

It is thought that with the warming of the SSTs and deepening of the boundary layer, the moisture and temperature fluxes are not longer sufficient to cool and moisten the entrained air to match the conditions in the boundary layer (Bretherton and Wyant, 1997; Ciesielski et al., 2001). Instead, the entrained warm air is carried downward and creates a weak stable layer at the cloud base. Only the most energetic rising plumes are then able to penetrate in to the cloud layer to form cumulus under stratocumulus clouds. The detraining plumes help maintain the stratus clouds.

Wyant et al. (1997) suggest that even farther downstream, strong updrafts penetrate into the inversion layer and entrain sufficient amounts of dry air to dilute the cloud water they detrain to the point where the stratus deck breaks up. Drizzle (e.g. Khairoutdinov and Kogan, 2000) and cloud-top entrainment instability (Randall, 1980; Deardorff, 1980) have also been implicated as contributing to stratus breakup.

Modeling these regimes requires adequately representing cloudy mixed layers, updrafts and plumes, and the effects of entrainment. A scheme like the EDMF, which explicitly represents both turbulent mixing and mass fluxes, appears to be a step in the right direction.

5.1. Threat score analysis

The first lidar observations from space were obtained during the Lidar In-space Technology Experiment (LITE), an eleven-day-long experiment in 1994 during which a lidar onboard the space shuttle Discovery orbited the earth (Winker et al., 1996). In his 2000 dissertation, Steven Miller examines differences between cloud distributions observed during LITE and those predicted by the ECMWF short-term forecast. Miller analyzed 66 night-time orbits by recasting the high resolution lidar data onto the ECMWF model grid, calculating a cloud fraction (i.e. the ratio of cloudy to total lidar samples within a model grid box), and comparing it to the cloud fraction of the model forecast. Since the lidar's footprint is very narrow, it cannot fully sample the area covered by a model grid box. Hence, the lidar cloud fraction is only an estimate of the true fractional cloudiness within the grid box area. Miller used hit rate statistics to test how well the model forecast agrees with the observations. The uncertainty associated

with the lidar cloud fraction was taken into account as a weight applied to the false-alarm-rate.

As an alternative to Miller's hit rate, an equitable threat score following Schaefer (1990) is used here. The equitable threat score takes into account that it is far more likely that a grid point will be clear, than that it will be cloudy, and does not reward the model excessively for its skill to correctly forecast clear conditions. The equitable threat score is defined as

$$ETS = \frac{HIT - CHA}{F + O - HIT - CHA} \tag{5.1}$$

where HIT is the number of grid points along the transect where the existence of a cloud was correctly forecast, F is the number of grid points where the model forecasts clouds, O the number of grid points where clouds are observed, and CHA is a measure of the number of grid points where a correct forecast would occur by chance. CHA is defined as

$$CHA = O\frac{F}{V} \tag{5.2}$$

where V is the total number of grid points evaluated. The bias is defined as

$$BIAS = \frac{F}{O}. \tag{5.3}$$

In order to exclude errors due to full signal attenuation, only grid boxes that could be sampled by the lidar are included in the calculations, i.e. any layers below the level of full signal attenuation are excluded. There is also a threshold of 1% cloud fraction for a

grid point to be considered cloudy. This is approximately the smallest cloud fraction observable in the HR GLAS data.

This equitable threat score can only assess whether the model forecasts clouds in the correct location, at the correct time. It does not evaluate whether the cloud fraction is similar, nor does it give credit for existing clouds which are only slightly misplaced.

The results for the four ECMWF model runs are not encouraging (Table 5.1). According to the ETS, there is very little difference between the four runs, and in fact, switching from the dry diffusive BL to the EDMF BL scheme initially lowers the score. However, modifying the run (CY29R1-S) leads to a slight improvement.

Table 5.1 Equitable Threat Score

Model	ETS	BIAS
CY28R3	0.289987	0.954243
CY29R1	0.288955	0.942745
CY29R1-E	0.286878	0.935600
CY29R1-S	0.292319	0.969873

The fact that the misplacement of a cloud even by one model layer can produce a miss is especially problematic in regions with boundary layer clouds. Here, the lidar's signal is often fully attenuated one or two model layers into the cloud, and any layers below are excluded from the comparison. If the model's boundary layer clouds are just slightly displaced, they will not be counted. This can be alleviated by matching GLAS clouds in a given model layer not just with the model results in the same layer, but also the layer above or below, allowing a certain error margin in the vertical placement of the cloud layer. This, however, leads to further problems, since a model layer near the

surface may be only several tens of meters thick, while layers in the upper atmosphere span several kilometers.

In this particular situation, where the only major differences between model runs are the boundary layer clouds, it seems prudent to abandon the threat score as a measure of model improvement, as it is particularly unsuited to assess the model's performance in the boundary layer. Instead, a more appropriate way to address the problem will be demonstrated in the following section.

5.2. ECMWF model evaluation

Using Steven Miller's work as a starting point, roughly 1500 tracks, both night- and daytime, from GLAS are used and compared to four versions of the ECMWF IFS model, and two versions of the GEOS-5 model.

Following Miller's method, each track (partial orbit between 40°N and 40°S) is co-located in space and time with the nearest 3-hourly model forecast. Within each 3D model grid box transected by the lidar, the mean and standard deviation of the cloud top height and cloud base height, as well as a cloud fraction are calculated. Several additional variables are tracked: the total number of lidar shots within the box, the number of transitions from clear to cloudy, or cloudy to clear shots, and how many of the shots are flagged for full attenuation.

This process is repeated for each of the four lidar resolutions. At MR, the average optical depth is saved as well.

5.2.1. Cloud type compositing

Cloud type compositing can be a helpful tool to examine how well the model forecasts a certain cloud type. As mentioned in the introduction, many GCMs, including the ECMWF model, have difficulties in forecasting marine boundary layer clouds correctly. The ECMWF has worked on and recently implemented a new boundary layer and shallow cloud scheme hoping to improve model performance.

The two most common boundary-layer cloud types found in the subtropical oceans are stratocumulus and trade cumulus clouds. They can be identified using location, cloud top height and cloud fraction as criteria. Four regions in the eastern ocean basins of the North and South Pacific, and the South Atlantic and Indian Ocean have been identified as regions with frequent stratocumulus and trade cumulus occurrence (Fig. 5.1 and Table 5.2).

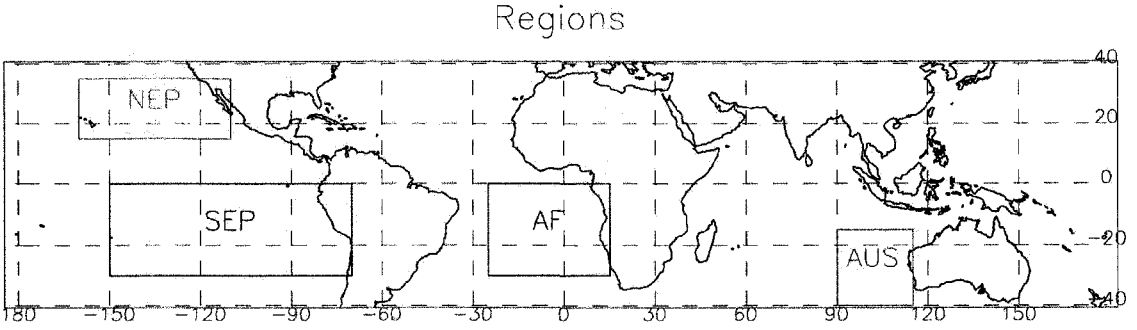

Fig. 5.1 Regions that are searched for *Sc* and *TCu* type clouds: North East Pacific (NEP), South East Pacific (SEP), Atlantic west of the African coast (AF) and Indian ocean west of the Australian coast (AUS).

Table 5.2 Latitude and longitude of regions shown in Fig. 5.1.

Region	Latitude Range	Longitude Range
AF	0° to 30°S	25°W to 15°E
NEP	35°N to 15°N	160°W to 110°W
SEP	0° to 30°S	150°W to 70°W
AUS	15°S to 40°S	90°E to 115°E

Within these regions, a stratocumulus-type cloud is identified as a cloud with no more than 2 km cloud top height, and 80% or higher cloud fraction (type: *Sc*). A trade cumulus or transition type cloud is identified by a cloud top height not exceeding 3 km, and a cloud fraction of less than 80% (type: *TCu*).

Table 5.3 Criteria for cloud type categories.

Cloud Type	Cloud Fraction	Cloud Top Height
Sc	≥ 80%	≤ 2 km
TCu	< 80%	≤ 3 km

Cloud fraction is a grid variable in the model, and easily available. In the lidar observations, the ratio of cloudy to total shots within a grid box is identified as the cloud fraction.

The lidar cloud product provides cloud top and base height for every shot. As shown in Fig. 5.2, the distance between cloud top and base in a single shot can span multiple cloud layers. The shot is counted as 'cloudy' in each of those model layers. The cloud top height (CT) and cloud base height (CB) associated with the shot is the average of true value detected by GLAS in all the vertical layers spanned by the cloud. That is, the cloud top height (base) in a given grid box is the average of the detected CT (CB) of each cloudy shot passing through the grid box.

The gridded lidar observations and the model data are searched independently for samples meeting the cloud type criteria. The lowest 2 km (3 km) of each model column are searched for the layer with the highest cloud fraction. This cloud fraction is compared to the threshold of 80%. In case of the GLAS data, the average cloud top of

the layer with highest cloud fraction is chosen to represent the cloud top height value for the sample. The higher the cloud fraction, the more shots are averaged together to obtain

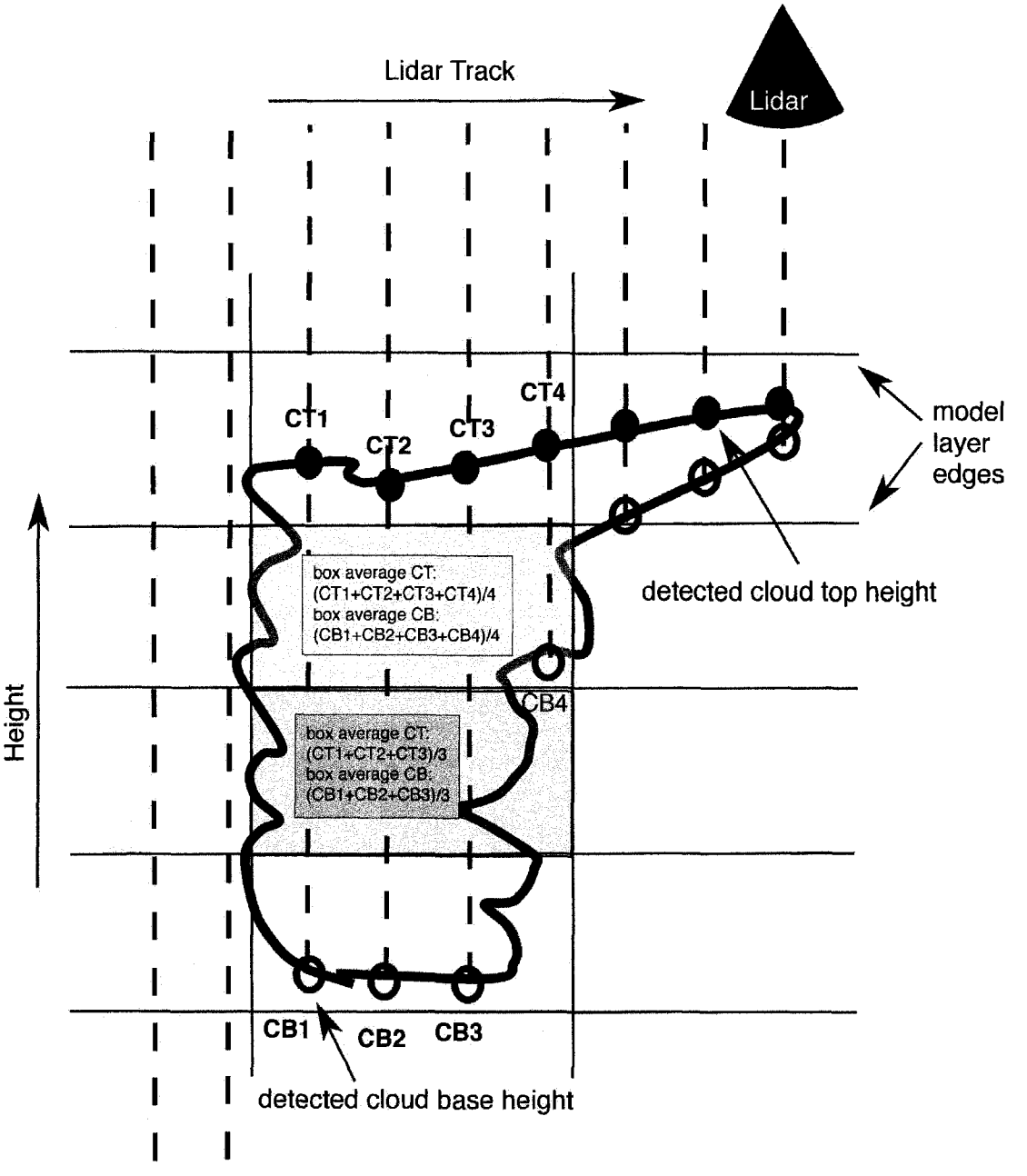

Fig. 5.2 Schematic illustrating how the average cloud top and base height of the remapped lidar data is calculated for each grid box. CB and CT stands for "cloud base" and "cloud top", respectively.

the cloud top height, which will presumably give the best estimate. In case of the model data, the layer edge of the highest, still-cloudy model layer above the maximum cloud fraction layer is chosen as the cloud top height.

Once all model columns within the four regions have been checked against the criteria and tagged for a cloud type, statistics for the cloud types can be calculated. The figures at the end of the chapter (Fig. 5.35 through Fig. 5.47) show histograms of the cloud fraction, cloud top and base height, both for samples from all regions combined, and for individual regions. In case of the model data, composite temperature, moisture and vertical velocity profiles are shown as well (Fig. 5.48 through Fig. 5.55).

A sample plot for observations (Fig. 5.3) and the model versions (Fig. 5.4 through Fig. 5.7) is described here for the cloud type *Sc* and results from all four regions combined. Equivalent figures exist for the individual regions and for cloud type *TCu*. Those figures will be referred to throughout the text, but due to the volume of figures are collected at the end of the chapter so as not to interrupt the discussion too much. The following table (Table 5.4) is a navigation aid to find the appropriate figures.

PAGE NUMBERS FOR FIGURES AT THE END OF THE CHAPTER	**GLAS**		**CY28R3**		**CY29R1**			**CY29R1-E**			**CY29R1-S**		
	Sc	*TCu*	*Sc2*	*TCu*	*Sc*	*Sc2*	*TCu*	*Sc*	*Sc2*	*TCu*	*Sc*	*Sc2*	*TCu*
Number of samples per 1°x1° bin	67	67	68	68	69	69	69	70	70	70	71	71	71
Cloud fraction, base and top height histograms by region	72	73	74	75	76	77	78	79	80	81	82	83	84
Composite temperature and moisture profiles			85	86	87		88	89		90	91		92

	GLAS		**GEOS1**		**GEOS2**	
	Sc	*TCu*	*Sc*	*TCu*	*Sc*	*TCu*
Number of samples per 1°x1.25° bin	93	93	94	94	95	95
Cloud fraction, base and top height histograms by region	96	97	98	99	100	101
Composite temperature and moisture profiles			102	103	104	105

Table 5.4 Table referencing the figures at the end of the chapter by page number.

Fig. 5.3 Histogram of cloud fraction and cloud top height of all GLAS samples classified as *Sc*. In the left panel, the blue line indicates the cloud fraction calculated from HR GLAS data, the red line the cloud fraction calculated from FR GLAS data. In the right panel, the blue, red and green lines show the histogram for the grid box average cloud top height calculated from LR, MR and HR GLAS data, respectively. The total number of GLAS samples classified as *Sc* is shown in the upper left corner of the left panel.

In Fig. 5.3, the histograms for cloud fraction and cloud top height for the GLAS observations meeting *Sc* criteria in all regions are shown. A cloud base height histogram is not shown, since most lidar shots are fully attenuated in marine boundary layer clouds, and the few retrieved cloud bases are from optically thin clouds that are not representative of the cloud regime. The label 'ALL' refers to the combined samples from all four regions (for individual regions, see Fig. 5.35). Both the cloud fraction from the HR and the FR lidar data are plotted in the left panel. Due to the nature of the lidar cloud fraction (ratio of cloudy to total shots per grid column), the cloud fraction distribution is limited to discrete values, depending on the number of shots per column. Hence, the FR distribution appears smoother than the HR distribution. The total number of *Sc* samples found in all regions is printed in the upper left corner of the left panel.

The right panel shows the histogram of cloud top height, for high, medium and low resolution. This is the box average height described in the section above, not the height directly measured by the lidar in each shot. The total number of samples included in

each of the histograms is the same as in the cloud fraction histogram. Since the HR cloud fraction is used as for the sample classification, there are some samples in the FR distribution with cloud fractions below 80%. In these cases, the HR and FR observations are not consistent.

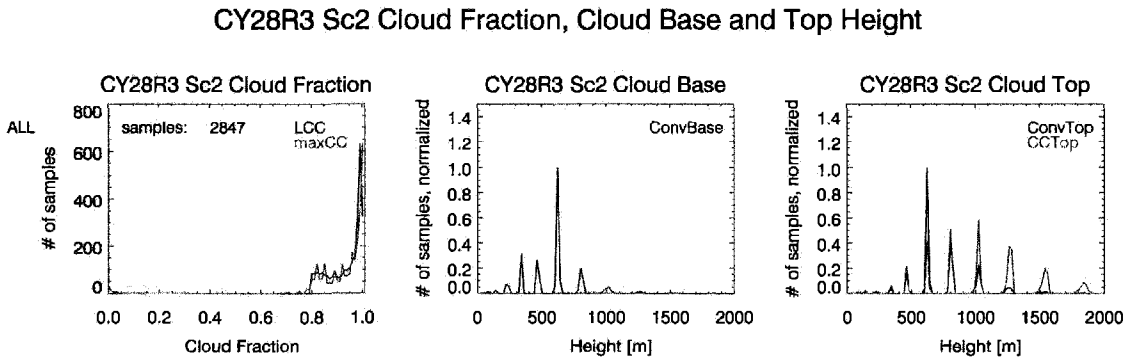

Fig. 5.4 Histogram of cloud fraction, cloud base height and cloud top height for all CY28R3 samples classified as *Sc2*. The number of samples classified as *Sc2* in all four regions is printed in the upper left corner of the left panel. The variable abbreviations used in the labels are explained in the paragraph below.

Fig. 5.4 shows the corresponding histograms for the ECMWF model version CY28R3 (see Fig. 5.37 for individual regions). 'LCC' is the low cloud cover variable of the model, which is the area cloud fraction of the lowest 4 km of the model atmosphere. 'maxCC' is the largest cloud fraction encountered in the model column in any level below 2 km (3 km for *TCu*). The two measures of cloud fraction differ if high cloud fractions exist at a level above the 2 km (3 km) level prescribed by the selection criteria, but below 4 km. In the regions examined here, cloudiness just above the boundary layer is not very common, so the two measures usually agree well.

The middle panel shows a histogram of the convection base as a measure of the cloud base, determined by the shallow convection scheme. The discrete model layers lead to distinct maxima in the distribution. Widening the histogram's bins would smooth

out the curve somewhat, but irregularities would remain due to the increasing layer thickness with height, and some of the detail might be lost. The right panel shows the convection top as a measure of the cloud top. The convection base and top refer to the model layers over which the convective parameterization is active. The height corresponding to the upper (lower) layer interface is shown in the histograms for the convection top (base). As an alternative measure, 'CCTop' is the upper interface of the highest cloudy model layer belonging to the boundary layer cloud. It is obvious from the graph above that the two measures of the cloud top do not agree well. This will be discussed further below.

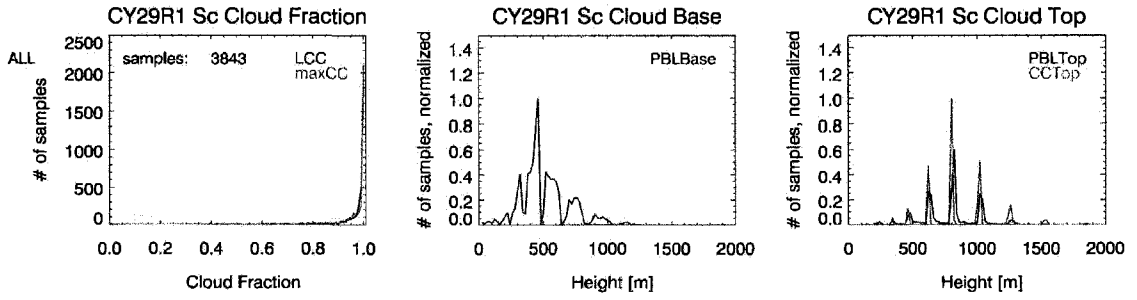

Fig. 5.5 Histogram of cloud fraction, cloud base height and cloud top height for all CY29R1 samples classified as *Sc*. The number of samples classified as *Sc* in all four regions is printed in the upper left corner of the left panel. The variable abbreviations used in the labels are explained in the paragraph below.

For the three versions of CY29R1, two different ways of identifying *Sc* clouds are used. *Sc* clouds are now defined as clouds generated by the new eddy diffusivity mass flux scheme. The scheme determines the cloud base via test parcel ascent ('PBLbase'), and the BL top is coincident with the cloud top ('PBLTop'). As an alternative, the same criteria as for CY28R3 (i.e. only cloud fraction and cloud top height) are used to identify stratocumulus-type samples, regardless of how the samples were generated. These are

labeled *Sc2* in the figures and tables below. The category *Sc2* normally contains more samples, since clouds generated by the convective parameterization that fulfill the criteria are also included (*Sc* is usually a subset of *Sc2*). Otherwise, the variables plotted are the same as for CY28R3. To remain consistent, the sole *Sc*-type category in CY28R3 will be labeled *Sc2*. The figures containing histograms for individual regions, and for the sensitivity runs CY29R1-E and CY29R1-S can be found at the end of the chapter (Fig. 5.39, Fig. 5.42 and Fig. 5.45).

Fig. 5.6 and Fig. 5.7 show composite temperature, specific humidity and relative humidity profiles for all detected *Sc2/Sc* samples in the model versions CY28R3 and CY29R1 (for individual regions see Fig. 5.48 and Fig. 5.50). The atmospheric profiles for each sample grid column on model levels are interpolated onto an evenly spaced height grid with layer thickness 20 m. Then all samples identified as *Sc2/Sc* are averaged, and the standard deviation from the mean is calculated at each level.

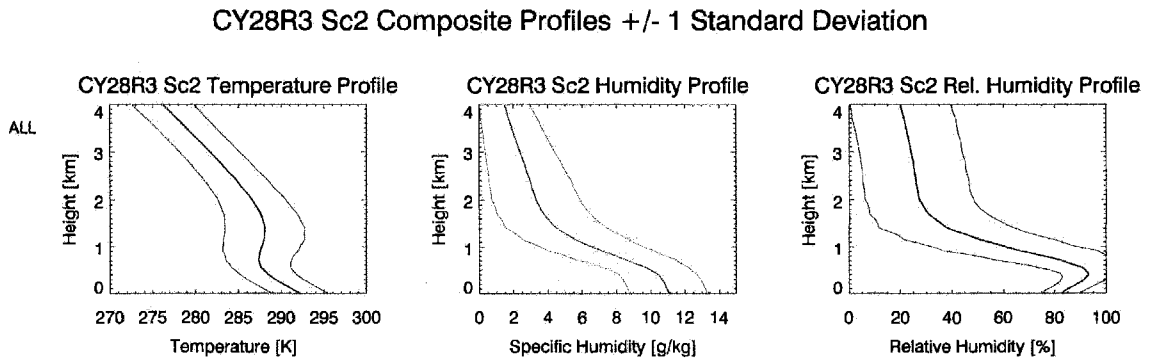

Fig. 5.6 Composite profiles of model temperature, specific and relative humidity for all CY28R3 model columns containing clouds classified as *Sc2* (thick lines). The thin lines indicate the plus/minus one standard deviation range.

It is worth noting that the composite profiles reflect the locations of the samples. Comparing Fig. 5.50 and Fig. 5.54, it would appear that the temperature inversion is

more pronounced for *Sc* clouds in CY29R1, compared to CY29R1-S. However, a look at Fig. 5.26 and Fig. 5.32 shows that run CY29R1-S produces *Sc* samples farther west in

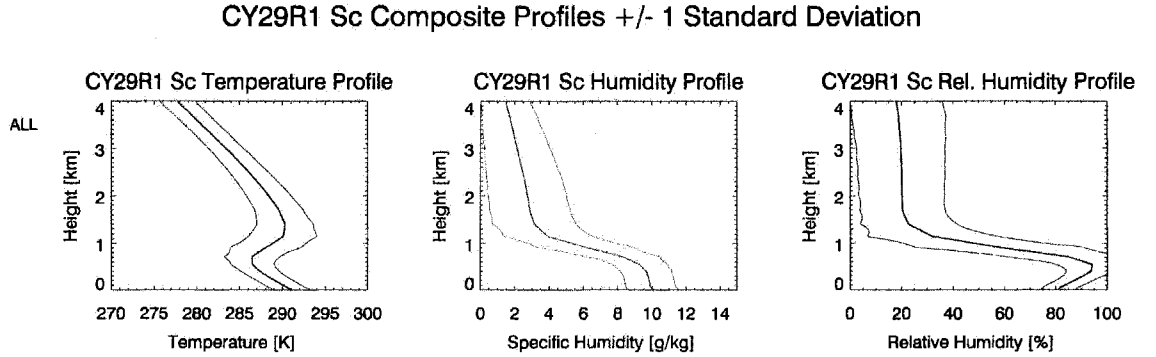

Fig. 5.7 Composite profiles of model temperature, specific and relative humidity for all CY29R1 model columns containing samples classified as *Sc* (thick lines). The thin lines indicate the plus/minus one standard deviation range.

the ocean basins. The weakened inversion in the composite temperature profile does not necessarily indicate that at a given grid point in the model, the inversion is weaker, but may simply reflect that additional *Sc* clouds are generated in areas with weaker inversions. This may seem to be counter-intuitive, since fewer stratocumulus clouds are found in regions with weaker inversions. However, the change here is the result of relaxing an overly strict constraint that artificially confined the *Sc* samples to regions with very high lower level stability. Finding more *Sc* samples to the west is a welcome change, as the model underestimates the amount of clouds with high cloud fraction. The sensitivity runs are discussed in more detail in the next section.

5.2.2. Frequency of occurrence and location of samples

The total number of 1°x1° grid boxes sampled by the lidar within each region is independent of the model version (Table 5.5). The fraction of those samples classified as either *Sc* or *TCu* then represents the frequency of occurrence of these cloud types in each

region, or all regions combined. These frequencies of occurrence are listed in the following tables.

Table 5.5 Total number of 1°x1° samples transected by a GLAS track in all four regions, over ocean.

Region	Number of Samples
ALL	25830
NEP	5312
SEP	11786
AF	5552
AUS	3180

Table 5.6 Percentage of samples with occurrence of *Sc*, *Sc2* and *TCu* type clouds in all four regions. The rightmost column shows the percentage of samples classified into any of the low cloud categories. For CY29R1 and CY29R1-E, the *Sc* category is a subset of the *Sc2* category, so the total is the sum of the *Sc2* and *TCu* categories. For CY29R1-S, some of the clouds generated by the EDMF exceed the 2 km cloud top limit and hence do not fall into the *Sc2* category. Here, the total is the sum of the *Sc* and *TCu* categories.

ALL	% *Sc*	% *Sc2*	% *TCu*	% total
GLAS	31.2		41.8	73.0
CY29R3		11.8	72.8	84.6
CY29R1	14.9	19.4	66.7	86.0
CY29R1-E	20.5	22.6	62.7	85.3
CY29R1-S	23.7	22.5	63.4	87.1

The numbers listed in Table 5.6 show what percentage of samples is classified as *Sc*, *Sc2* or *TCu* in all regions combined. Fig. 5.22 through Fig. 5.34 at the end of the chapter show the corresponding locations of the samples. GLAS detects 31.2% *Sc*, and 41.8% *TCu* samples, for a total of 73% classified as low clouds. All of the model versions sort around 12% more samples into one of the two categories. As the cloud fraction within a model grid box shrinks, the chance that the lidar will miss the clouds within the area increases. It is possible that part of this discrepancy is due to sampling errors of the

lidar. This analysis will show evidence, though, that the model has a tendency to produce an overabundance of low clouds with very low cloud fraction.

Table 5.6 also shows that CY28R3 underestimates the frequency with which *Sc* clouds are observed by about 2/3. Instead, the model produces clouds with lower cloud fraction, which fall into the category *TCu*. In each model column, the type of convection parameterization active is flagged. The types are listed briefly in Table 5.7, but are explained fully in Appendix B. Table 5.8 shows that roughly a third of the *Sc* samples are produced at model grid points where no convection parameterization is active. In this case, it is likely that the existing cloud is left over from a previous time step. Another third of the samples exist where mid-level convection is active. Since mid-level convection refers to convection above 500 hPa, any clouds below that level are again leftover from previous time steps, or produced by the large-scale moisture scheme. Only about a third of the *Sc* samples are found at grid points with active shallow convection. It is possible that this is the model's attempt to represent cumulus under stratus clouds, which have been frequently observed in areas where stratocumulus clouds transition into the trade cumulus regime (e.g. during ASTEX; Albrecht et al., 1995). In the *TCu* category, the majority of grid columns have active shallow convection.

Table 5.7 Convection and PBL types explained. PBL Types are only available for the CY29R1 runs.

	Convection Type	**PBL Type**
Type 0	no convection	stable PBL
Type 1	deep convection	dry convective PBL
Type 2	shallow convection	cloudy PBL ("stratocumulus")
Type 3	mid-level convection	dry PBL below convection ("cumulus")

Table 5.8 Frequency of occurrence of convection types for CY28R3 samples classified into the *Sc2* and *TCu* categories.

CY28R3	Convection Type *Sc* [%]	Convection Type *TCu* [%]
Type 0	34.2	14.5
Type 1	0.6	0.3
Type 2	28.5	81.1
Type 3	36.8	4.1

The occurrence of *Sc* increases with the introduction of the new EDMF boundary layer scheme. This is a positive change, since CY28R3 underestimated the frequency of occurrence of *Sc* by about 2/3, compared to the GLAS observations. As a reminder, two categories of *Sc* clouds are distinguished in the CY29R1 run: *Sc2* denotes stratocumulus samples identified only by cloud fraction and -top height (just as in CY28R3), whereas samples labeled as *Sc* were generated by the EDMF scheme. Generally speaking, the *Sc* samples are a subset of the *Sc2* category, since most clouds generated by the EDMF scheme fulfill the cloud fraction and -top height criteria. Table 5.9 shows that the majority (66.6%) of the samples identified as *Sc2* are generated by the new boundary layer scheme (PBL type 2 active), i.e. *Sc* samples make up about 2/3 of the *Sc2* category.. The remainder of *Sc2*-type clouds are either generated by the shallow convective scheme (15.8%) or are left over from previous time steps.

Table 5.9 Frequency of occurrence of convection and PBL types for CY29R1 samples classified into the *Sc*, *Sc2* and *TCu* categories.

CY29R1	PBL Type *Sc* [%]	PBL Type *Sc2* [%]	PBL Type *TCu* [%]	Conv. Type *Sc* [%]	Conv. Type *Sc2* [%]	Conv. Type *TCu* [%]
Type 0	0.0	1.3	2.0	70.6	52.4	18.1
Type 1	0.0	13.2	84.1	0.1	0.3	0.6
Type 2	100.0	66.6	2.9	0.0	15.8	76.4
Type 3	0.0	20.0	11.1	29.3	31.5	5.0

The number of *TCu* samples decreases by about the same amount as the *Sc2* category has increased, indicating that samples switch categories as the cloud fraction increases. Curiously, the majority of *TCu* samples (84.1%) are found at grid points where the boundary layer is "dry convective". That is, the test parcel never reaches the lifting condensation level. Nonetheless, the shallow convective parameterization produces clouds above this boundary layer. Clearly, this is somewhat inconsistent. One would expect to find a boundary layer of type 3 (dry convective underneath cloud) more often. Why is the test parcel so dry? A possible explanation may be the formulation of the entrainment term used in the test parcel ascent. Entrainment here refers to horizontal mixing of the test parcel, imbued with a temperature and moisture excess, with the environmental air of the form

$$w_e = \frac{1}{\tau w_u} + \frac{1}{z}, \tag{5.4}$$

where τ is a time scale of 500 s, w_u is the updraft velocity, and z is height above ground. Since w_u is zero at the surface, both terms in the sum have a strong dependence on inverse height, which may lead to excessive dilution and drying of the test parcel. In the entrainment run CY29R1-E, the second term 1/z is dropped in the entrainment formulation, reducing the dilution of the test parcel.

As a result, the fraction of *Sc*-type samples increases further, and a larger portion (77.3%) or the samples classified *Sc2* are generated by the EDMF scheme (Table 5.10). Also notable is that about two-thirds of the *TCu* samples (61.3%) now come from grid points where the "dry convection under cloud" scheme is active (previously only 11.1%). This seems to be a more physical representation of the processes predominant

Table 5.10 Frequency of occurrence of convection and PBL types for CY29R1-E samples classified into the *Sc*, *Sc2* and *TCu* categories.

CY29R1-E	PBL Type *Sc* [%]	PBL Type *Sc2* [%]	PBL Type *TCu* [%]	Conv. Type *Sc* [%]	Conv. Type *Sc2* [%]	Conv. Type *TCu* [%]
Type 0	0.0	1.1	2.1	66.4	52.6	23.6
Type 1	0.0	4.6	32.1	0.0	0.3	0.5
Type 2	100.0	77.3	4.5	0.0	10.0	68.5
Type 3	0.0	16.9	61.3	33.6	37.1	7.4

in the four oceanic regions discussed here.

Comparing Fig. 5.22, Fig. 5.24 and Fig. 5.26, it is evident that GLAS not only detects more *Sc* samples, but also that more of those samples are located in the western half of the four regions than can be found in the model versions CY28R3 and CY29R1. The Klein & Hartmann stability criterion employed in CY29R1 requires lower level atmospheric stability of $\theta_{700\ hPa}-\theta_{sfc} > 20$ K. This confines the *Sc* samples generated by the EDMF scheme to the regions of greatest stability. As a sensitivity study, CY29R1-S relaxes this stability criterion to $\theta_{700\ hPa}-\theta_{sfc} > 16$ K.

Table 5.11 Frequency of occurrence of convection and PBL types for CY29R1-S samples classified into the *Sc*, *Sc2* and *TCu* categories.

CY29R1-S	PBL Type *Sc* [%]	PBL Type *Sc2* [%]	PBL Type *TCu* [%]	Conv. Type *Sc* [%]	Conv. Type *Sc2* [%]	Conv. Type *TCu* [%]
Type 0	0.0	1.2	2.2	67.3	55.3	20.8
Type 1	0.0	15.2	88.4	1.7	0.2	0.5
Type 2	100.0	81.2	7.0	0.0	12.2	72.6
Type 3	0.0	2.3	2.4	31.1	32.3	6.1

Fig. 5.32 clearly shows that the EDMF produces more *Sc* samples in the western half of the four regions in the CY29R1-S run. An even higher fraction of the *Sc*-type samples

(81.2% vs. 66.6% previously) are now generated by the EDMF scheme (Table 5.11). This indicates that samples that where previously generated by the convective schemes now fall within the area where the stability criterion is satisfied. A little more than 3% of *TCu* samples shift over to the *Sc2* category compared to CY29R1. This shift is of a similar magnitude as the resulting shift of samples in the CY29R-E sensitivity run.

Table 5.12 Percentage of samples with occurrence of *Sc*, *Sc2* and *TCu* type clouds in the North East Pacific region. The rightmost column shows the percentage of samples classified into any of the low cloud categories. For CY29R1 and CY29R1-E, the *Sc* category is a subset of the *Sc2* category, so the total is the sum of the *Sc2* and *TCu* categories. For CY29R1-S, some of the clouds generated by the EDMF exceed the 2 km cloud top limit and hence do not fall into the *Sc2* category. Here, the total is the sum of the *Sc* and *TCu* categories.

NEP	*% Sc*	*% Sc2*	*% TCu*
GLAS	45.8		22.3
CY29R3		10.6	68.2
CY29R1	8.8	14.3	67.6
CY29R1-E	11.6	13.9	66.0
CY29R1-S	21.1	17.4	64.2

So far, the analysis has only considered the total of samples from all four regions. However, regional variations exist (Fig. 5.35 through Fig. 5.55). The NEP and AF regions have a particularly high percentage of *Sc* samples in the lidar observations. Proportionally, this is true in the model versions also. The sensitivity to changes in the EDMF formulation varies with region. In the NEP for example, CY29R1 produces only 8.8% of *Sc* samples with the EDMF scheme. Weakening the parcel entrainment increases this fraction only by 2.8%. Relaxing the stability criterion on the other hand leads to an additional 12.3 percent of samples being generated by the EDMF. Clearly, a weak inversion seems to be more of a limiting faction in this region than a dry boundary layer. However, out of those 21.1% samples generated by the EDMF, only some still

fulfill the cloud fraction and cloud top height criteria necessary for category *Sc2*. That is, while more samples are being generated with the EDMF, some of those samples either have a cloud height exceeding 2 km, or a cloud fraction less than 80%.

In the SEP region, the reverse is true: The response to the altered entrainment formulation is more pronounced (7.4% additional EDMF samples). The response to the stability criterion is a bit weaker (5% additional EDMF samples), but most of the additional EDMF-generated samples still fulfill the *Sc2* criteria. The changes in the AF region resemble those in the NEP regions, but on a much smaller scale.

Table 5.13 Percentage of samples with occurrence of *Sc*, *Sc2* and *TCu* type clouds in the South East Pacific region. The rightmost column shows the percentage of samples classified into any of the low cloud categories. For CY29R1 and CY29R1-E, the *Sc* category is a subset of the *Sc2* category, so the total is the sum of the *Sc2* and *TCu* categories. For CY29R1-S, some of the clouds generated by the EDMF exceed the 2 km cloud top limit and hence do not fall into the *Sc2* category. Here, the total is the sum of the *Sc* and *TCu* categories.

SEP	*% Sc*	*% Sc2*	*% TCu*
GLAS	28.7		41.9
CY29R3		8.8	74.6
CY29R1	16.2	19.1	65.6
CY29R1-E	23.6	24.2	60.7
CY29R1-S	21.2	20.4	64.1

Table 5.14 Percentage of samples with occurrence of *Sc*, *Sc2* and *TCu* type clouds in the African region. The rightmost column shows the percentage of samples classified into any of the low cloud categories. For CY29R1 and CY29R1-E, the *Sc* category is a subset of the *Sc2* category, so the total is the sum of the *Sc2* and *TCu* categories. For CY29R1-S, some of the clouds generated by the EDMF exceed the 2 km cloud top limit and hence do not fall into the *Sc2* category. Here, the total is the sum of the *Sc* and *TCu* categories.

AF	*% Sc*	*% Sc2*	*% TCu*
GLAS	44.4		37.8
CY29R3		15.2	75.4
CY29R1	22.0	26.5	66.6
CY29R1-E	28.1	30.6	61.7
CY29R1-S	31.5	30.2	62.8

The increase in EDMF samples with the relaxed stability criterion is most pronounced in the AUS regions. Three times as many samples are generated by the EDMF, and the great majority of them fulfill the *Sc* criteria for cloud fraction and cloud top height. In CY29R1, where the EDMF is disallowed from generating clouds more often due to lacking lower level stability, the convective parameterizations cannot generate the same amount of low, high-fraction clouds.

Table 5.15 Percentage of samples with occurrence of *Sc*, *Sc2* and *TCu* type clouds in the Australian region. The rightmost column shows the percentage of samples classified into any of the low cloud categories. For CY29R1 and CY29R1-E, the *Sc* category is a subset of the *Sc2* category, so the total is the sum of the *Sc2* and *TCu* categories. For CY29R1-S, some of the clouds generated by the EDMF exceed the 2 km cloud top limit and hence do not fall into the *Sc2* category. Here, the total is the sum of the *Sc* and *TCu* categories.

AUS	***% Sc***	***% Sc2***	***% TCu***
GLAS	32.7		41.9
CY29R3		12.6	69.6
CY29R1	7.8	16.7	69.3
CY29R1-E	10.7	17.4	66.1
CY29R1-S	24.1	24.9	60.8

Considering the figures and tables just discussed, an improvement (as measured in the agreement with GLAS observations) can be demonstrated in both the frequency of occurrence and location of *Sc*-type clouds from model version CY28R3 to CY29R1. Both sensitivity runs further increase the numbers of *Sc*-type samples, and the CY29R1-S run in particular also improves agreement in the location of the samples with the GLAS observations.

In the *TCu* category, the models consistently produce *TCu* samples more frequently than observed by GLAS. As mentioned above, it is possible that GLAS mis-classifies some of the cloudy grid boxes as clear, particularly if the cloud fraction is very low. The

location and number of *TCu* samples in the models changes primarily through re-classification of samples from the *TCu* category to the *Sc* or *Sc2* categories. This is to be expected, since only the boundary layer parameterization varies between the model runs, but the majority of the *TCu*-type clouds are generated by the convective parameterizations, which remain the same.

5.2.3. Characteristics of cloud type categories

Now that the frequency of occurrence and location of the cloud type samples have been discussed, does each cloud type have distinct characteristics? If so, are these characteristics realistic?

The GLAS *Sc* cloud fraction distribution is characterized by a smooth, exponential increase in samples from 80% to 100% cloud fraction (Fig. 5.35). CY28R3 starts out with slight drop in sample numbers from 80% to 90%, and then a rapid increase to 100% cloud fraction (Fig. 5.37). All other model versions of category *Sc* mirror the behavior of the GLAS distribution (Fig. 5.39, Fig. 5.42 and Fig. 5.45). Categories *Sc2*, which contain a mixture of samples generated by the EDMF, and samples generated by the convective scheme, look like a mixture of the distributions from CY28R3 and CY29R1 *Sc* (Fig. 5.40, Fig. 5.43 and Fig. 5.46). This suggests that the EDMF produces clouds with a cloud fraction distribution similar to that observed by GLAS, while clouds generated by other means, but still fulfilling the *Sc*-criteria, have cloud fractions consistent with the model's convective parameterization.

The cloud-top height distribution from the GLAS *Sc* category has a broad maximum around 1300 m. Regions SEP and AF favor lower cloud tops (maximum around 1200

m), regions NEP and AUS have distributions skewed towards higher cloud tops (1600 m NEP, 1900 m AUS).

The two measures of cloud-top height plotted for the models are clearly inconsistent for CY28R3. The model level up to which the convective parameterization is active ('ConvTop') is much lower than the highest model level with positive cloud fraction ('CCTop'). Since samples can fulfill the criteria without any convective parameterization being active ("leftover" cloudiness from previous time steps, or large-scale moisture), there are samples for which no ConvTop exists. But even when only samples generated with the shallow convective parameterization are considered, the inconsistency remains. Clearly, positive cloud fraction (and cloud water) extend well above the layer to which the convective parameterization is active. In fact, the shallow convective scheme detrains moisture into the model layer above the convection top. But even this cannot explain the 400 m difference in the maximum peak of ConvTop and CCTop in the CY28R3 cloud top height histogram.

As it turns out, the convective scheme periodically pumps moisture deeper into the boundary layer, where it remains under the inversion. This is illustrated in the following figure (Fig. 5.8). The CY29R1 configuration of the ECMWF model was run for the 1st of October, 2003, and every 900 s time step was saved. The model column in the figure below has a low cloud cover throughout the day, generated by the shallow convective parameterization. It is quite evident that the convection top is located around 500 m most of the time, but occasionally jumps up to 1000 m to deposit cloud liquid water into the layer above. This periodic pumping seems to explain why the top of the cloudy layer (CCTop) is not in agreement with the convection top (ConvTop). The grid box

resolution of the model doesn't allow representation of individual clouds. The pumping may be an attempt of the model to represent a situation it is no well suited to, such as cumulus under stratus clouds, or individual cumulus clouds penetrating the trade inversion. It appears that CCTop is the better representation of the actual location of the cloud top. Since the shallow convective scheme is the same in all the ECMWF runs, this conclusion would apply to CY28R3 as well.

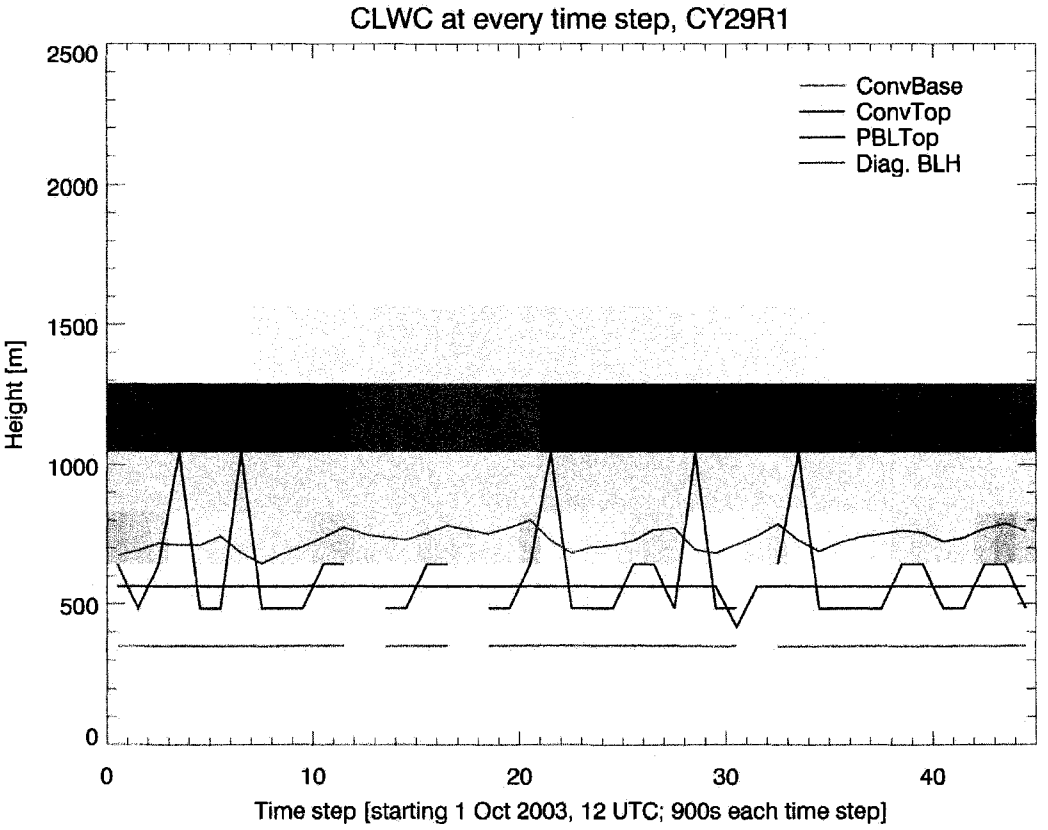

Fig. 5.8 Figure showing the cloud liquid water content (gray shading, scaled between 0 and 0.2 g/kg), the height of the convection base and top, the heigh of the boundary layer top (PBLTop), and the level of the diagnostic boundary layer height (Diag. BLH) for one model column in the CY29R1 run. The model column is centered at 1°N and 88°W. Values for each 900 s time step are shown, starting on October 1st 2003 at 12 UTC.

In all versions of CY29R1, the category *Sc* contains only samples generated by the EDMF. Here, the PBLTop (level to which EDMF scheme is active) and CCTop are consistent. Category *Sc2* contains a mixture of EDMF and convectively generated samples, and so not every sample has a ConvTop or PBLTop. If we consider CCTop to be the best measure of the model's cloud top height, The cloud top heights in CY28R3 are somewhat lower than observed, with a maximum at 1000 m. A slight shift towards higher values is evident in regions NEP and AUS, but much less pronounced than in the GLAS data.

The region-averaged cloud top height maximum for CY29R1 (*Sc2*) is even lower, at 800 m. This is partially due to the fact that a larger fraction of the samples originates in the eastern ocean basins in this model run. But the shift towards higher values in NEP and AUS is better represented than in CY28R3.

With the relaxed entrainment formulation in CY29R1-E (*Sc2*), the maximum in the cloud height distribution is still too low in the region average, but is quite good in regions NEP and SEP. The distribution in CY29R1-S quite closely resembles CY29R1, with only slightly higher values in the AUS region.

It is apparent that changing the entrainment formulation also changed the characteristic of the clouds generated by the EDMF. The moister test parcel can rise higher, leading to a shift in the cloud top height distribution. The relaxed stability criterion on the other hand does not change the characteristic of the clouds generated by the EDMF, but instead allows more samples to be generated.

In the cloud base distribution, a peak around 500 m dominates. It is clear that a cloud-free subcloud layer exists in virtually all of the *Sc* and *Sc2* samples. Since no

reliable GLAS observations exist for the cloud base height, we cannot say whether or not the modeled cloud base agrees with observations based on the lidar data.

For the *TCu* category, the GLAS cloud fraction distribution is quite noisy. This is largely due to the discrete HR cloud fraction. The HR cloud fraction is used to test against the <80% cloud fraction criterion. Occasionally, the FR cloud fraction does not agree well with the HR cloud fraction, hence some of the samples in this category have FR cloud fraction above 80%. The GLAS distribution shows a very broad maximum at 20% HR cloud fraction, but is relatively flat for fractions larger than 20%.

All the model versions show a very peculiar cloud fraction behavior: The distribution increases from low cloud fractions to 50%, where it suddenly drops significantly (Fig. 5.38, Fig. 5.41, Fig. 5.44 and Fig. 5.47). In addition, CY28R3 has preferred fractions at 50% and around 66% (spikes in the distribution, Fig. 5.38). The reason for this behavior is unclear. One might speculate that the sharp drop-off in the distribution is tied to an if-statement in the shallow convection parameterization, or some artificial threshold in the code (Martin Köhler, ECMWF, personal communication).

The cloud top height distribution has a very broad maximum in GLAS between 1500 m and 1700 m, depending on resolution. The NEP and AUS regions have a slightly higher maximum, in the AF region the maximum is a bit lower.

The model versions all reproduce this distribution rather well, including the regional variations. The maximum in the cloud base distribution is located slightly higher than in the *Sc* category, between 500 m and 700 m. There is not much difference between model versions. This is to be expected, considering that the convective schemes, largely responsible for the generation of *TCu* samples, have not changed.

Overall, the cloud top height of the *TCu* samples matches the distribution obtained from GLAS observations fairly well. The cloud fraction distribution on the other hand shows that the model has a tendency to produce more low clouds with less than 50% cloud fraction than the GLAS observations would indicate.

5.2.4. Sensitivity of the analysis to uncertainties in the lidar-derived cloud fraction

Uncertainty in the above analysis is introduced through the cloud fraction estimate obtained from the lidar observations. The lidar can only sample part of each 1°x1° grid box along its track. Astin and van de Poll (2001) propose a method to estimate the statistical error associated with sampling an area with a transect. The underlying assumption is an exponential distribution of cloud fields (Astin & DiGirolamo, 1999), i.e. the distribution of observed cloudy and clear intervals along the transect is of an exponential form. There is evidence that this assumption is accurate for cloud fields (Astin and Latter, 1998). Following this assumption and using Bayes' theorem, Astin and van de Poll (2001) provide a way to calculate the 90% confidence interval associated with a cloud fraction estimated from the lidar observations. That is, for a given lidar-observed cloud fraction, the 90% confidence interval spans the range of true cloud fractions within the grid box that were likely observed by the lidar. The larger the number of lidar shots that sample the grid box, the narrower the confidence interval. The exponential distribution assumed has no memory, i.e. a clear or cloudy interval intersecting the box boundary is assumed to be of unknown extent beyond the box boundary. The error estimate can only be calculated when there is at least one clear or

one cloudy interval completely contained within the grid box. This excludes completely clear or cloudy transects, as well as transects that start out clear, then become cloudy (both the clear and cloudy interval intersecting the boundary) or the reverse. The following illustration is an example:

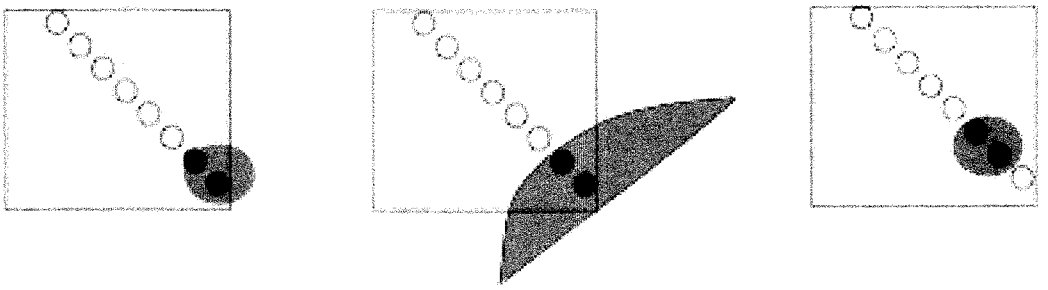

Fig. 5.9 Schematic showing the uncertainty associated with clear and cloudy regions intersecting the box boundary in the Astin et al. (2001) scheme.

In the left and middle grid boxes, the cloud lidar shots are located at the box boundary. They could either be sampling a small cloud (left) or a much larger cloud extending beyond the grid box (middle). Since the extent of the cloud is unknown, no estimate can be calculated. If the lidar shots lie in the interior of the grid box, the size of cloud associated with the cloudy interval is relatively well known, assuming exponential distribution of cloud intervals (right).

It turns out that the number of lidar shots within a box at high resolution (~90) is too small to give a reasonable error estimate. As a consequence, the confidence interval spans almost the entire range of cloud fractions. At full resolution (FR) however, the number of samples is sufficient for a good error estimate (~720). At FR, only one cloud layer is registered in the GLAS products. If high clouds exist, only the topmost cloud layer will be registered. Since marine boundary layer clouds exist most often in regions

of subsidence with little cloudiness above, the number of those samples is relatively small (around 4.5% of the total, Table 5.16). To avoid contamination, a FR cloud fraction is only calculated if at least 70% of the shots in the grid box are free of clouds with a top above 4 km. To establish a base line, the GLAS samples are re-classified using the FR cloud fraction estimate. The result is shown in Table 5.17. In the all-region average, a higher percentage of samples have low clouds, but the ratio of *TCu* to *Sc* samples is greater. Several things may contribute to this shift. It is unknown what kind of clouds the samples contained that have been excluded because no FR low cloud fraction was observed. It is also possible that the averaging process implemented at HR favors higher cloud fractions.

All FR samples are then re-classified once more, this time using the lower boundary of the confidence interval instead of the observed cloud fraction. In cases where no confidence estimate can be calculated, the original observed cloud fraction is retained. The argument here is that the lack of an error estimate often occurs for very high or very low cloud fractions, because the transect is either all cloudy or all clear. In this case, we argue that if the lidar observes 100% cloud fraction, it is not unreasonable to assume that

Table 5.16 Number of samples in regions for HR GLAS data, and FR GLAS data. There are fewer samples considered in the FR case because samples where no low cloud fraction can be determined are excluded. Since only one cloud layer is recorded at FR, this can be the case when clouds in the mid and upper troposphere are detected.

Region	HR	FR	% loss
ALL	25830	24655	4.5
NEP	5312	5037	5.2
SEP	11786	11287	4.2
AF	5552	5285	4.8
AUS	3180	3046	4.2

Table 5.17 Percent of samples classified as *Sc* and *TCu* in the four regions when classified with HR GLAS cloud fraction, FR GLAS cloud fraction, and the lower boundary of the Astin et al. error estimate derived from the FR GLAS cloud fraction.

ALL	**% *Sc***	**% *TCu***	**% total**
GLAS HR	31.2	41.8	73.0
GLAS FR	26.2	50.5	76.7
GLAS LOW	21.6	57.5	79.1

the grid box is indeed filled with 80% or higher cloud fraction, and the sample classification won't be affected. The number of re-classified samples due to the shift in cloud fraction will show how sensitive the results found in the above sections are to errors in the cloud fraction estimate.

Table 5.18 shows the fraction of FR samples classified as *Sc* and *TCu* respectively, using the observed FR cloud fraction, and then using the lower limit of the Bayesian confidence interval. Roughly 4-5% of the samples previously classified as *Sc* shift to the category *TCu* when the lower limit estimate of cloud fraction is used.

Table 5.18 Percent of samples classified as *Sc* or *TCu* depending on whether the FR cloud fraction or the lower boundary of the error estimate is used.

Region	**FR % *Sc***	**FR % *TCu***	**LOW % *Sc***	**LOW % *TCu***
ALL	26.2	50.5	21.6	57.5
NEP	20.3	51.6	16.4	58.3
SEP	24.3	49.8	20.4	55.6
AF	35.3	49.6	27.6	60.0
AUS	27.6	52.5	23.8	59.3

Assuming that about 5% of the *Sc* samples observed by GLAS are possibly mis-classified due to an overestimation of the cloud fraction sampled along the transect, the fraction of *Sc* samples in Table 5.6 is still larger than in any of the model runs. Therefore, the qualitative analysis given in the previous sections appears to be robust.

5.2.5. Low cloud fraction in the tropical-subtropical belt

The cloud fraction distribution in the tropical-subtropical belt (40°N to 40°S), over both land and ocean is shown in the following figures. For the model, the low cloud fraction "LCC" (fraction below 4 km) is chosen, for the GLAS observations, the highest HR cloud fraction in the layers below 4 km is used as a comparable measure. Both land and ocean samples are considered. However, the 4 km lid is with respect to the mean sea level, i.e. in regions where the topography exceeds 4 km, the samples are discarded. In order to account for signal attenuation, bins with more than 50% attenuated shots are flagged as unreliable. In case of the model, the attenuation status for each model level is derived from the GLAS simulator. Only when at least one unattenuated level exist below 4 km is the low cloud fraction ("LCC") counted.

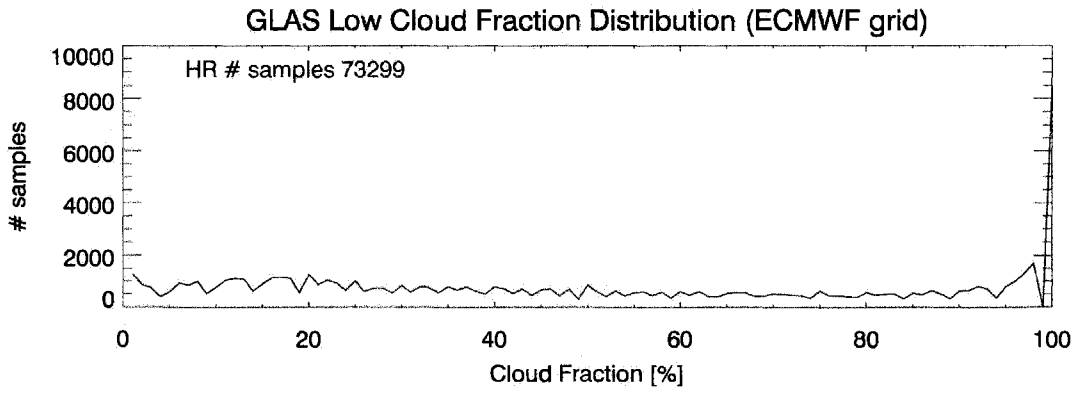

Fig. 5.10 Histogram of GLAS low (< 4 km) cloud fraction between 40°N and 40°S, calculated from HR data. The lowest bin (cloud fraction less than 0.01) is not plotted. The number in the upper left corner includes all samples with cloud fraction of 0.01 and above.

Fig. 5.10 shows the low cloud fraction distribution of the GLAS observations on the ECMWF grid. The lowest bin (0 to 1% cloud fraction) is not plotted. The noise in the distribution is due to the discrete nature of the HR cloud fraction. The distribution has

two maxima, in the lowest bin (not shown) and highest bin. Between these two maxima, the distribution has an overall slightly negative slope.

Out of the total number of columns in the subtropical belt transected by the lidar track (148,707), GLAS discards 20% (29,927) for having either topography above 4 km or being fully attenuated below 4 km. The number shown in Fig. 5.10 is the number of samples with observed cloud fraction of 1% or more, which amounts to approximately 62% or unattenuated samples. That is, GLAS observes approximately 62% of cloudy and 38% of clear samples in the subtropical belt.

The cumulative distribution in Fig. 5.11 is smoother, and hence easier to compare to the model versions. The slope of the cumulative distribution is relatively constant between 20% and 98% cloud fraction, with a slightly steeper slope below 20%, and above 98%.

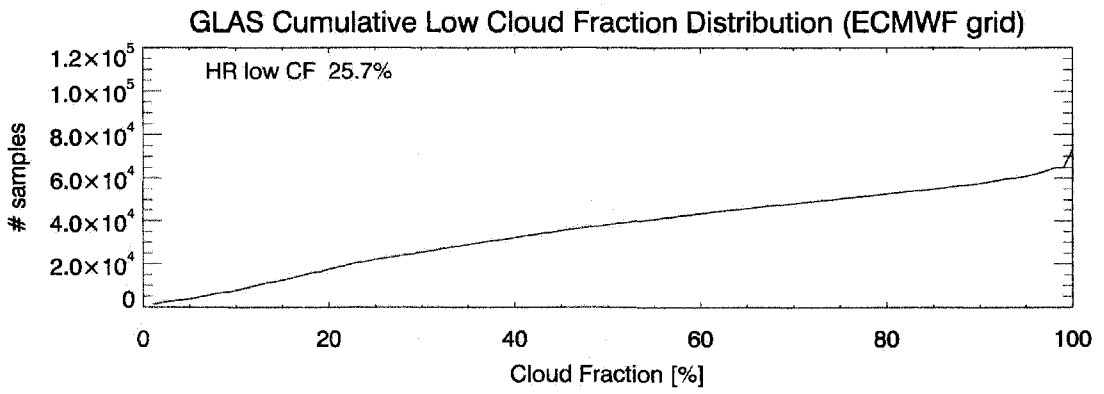

Fig. 5.11 Cumulative distribution of the HR cloud fraction histogram shown in Fig. 5.10. The low cloud fraction shown in the upper left corner is calculated as the product of the number of samples times the cloud fraction of each bin, divided by the total number of samples.

The cloud fraction distribution from CY28R3 in Fig. 5.12 shows the same preferred cloud fractions (peaks) at 50% and 66% that were discussed above. However, the drop-off at 50% cloud fraction is less pronounced for the entire subtropical belt compared to

the four low-cloud regions alone. In all four versions of the model, about 26% (between 37,474 and 38,740) of columns are flagged as attenuated according to the lidar simulator, or having topography above 4 km. That is 6% more than in the observations. This is consistent with studies that show that the ECMWF model tends to produce too much optically thick ice clouds (see e.g. Wilkinson et al., submitted to *Mon. Wea. Rev.*), which may mask more of the lower clouds. But we cannot exclude uncertainties in the lidar simulator formulation as a possible source of error either. Out of the unattenuated samples, approximately 73% (corresponding to the numbers in Fig. 5.12) have cloud fraction above 1%, with little variation between models. The models generate 10% more cloudy samples than GLAS observes. The distribution in Fig. 5.12 shows that all three versions of CY29R1 have distinctly more 100% cloud fraction samples than CY28R3, and lack the peaks at 50% and 66%, which is in better agreement with the GLAS observations.

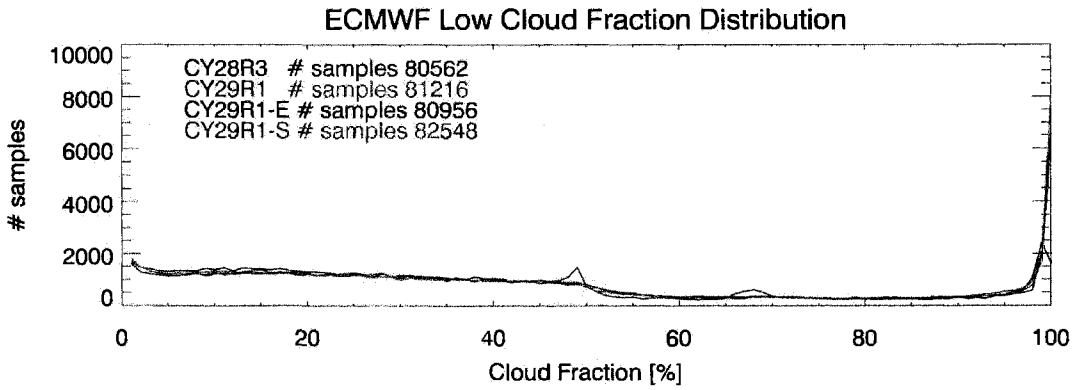

Fig. 5.12 Histogram of the ECMWF's low (< 4 km) cloud fraction between 40°N and 40°S for the four runs. The lowest bin (cloud fraction less than 0.01) is not plotted. The number in the upper left corner includes all samples with cloud fraction of 0.01 and above.

In the cumulative distribution (Fig. 5.13) all four model versions have a steeper slope below 50% cloud fraction, and a flatter slope above 50% cloud fraction than the GLAS

distribution. From version CY28R3 to CY29R1, to CY29R1-E/S, there are slightly fewer samples with low cloud fraction, but the difference is balanced almost completely by additional samples with near-100% cloud fraction.

The numbers in Fig. 5.11 and Fig. 5.13 are the total low cloud fraction calculated as the product of the samples in each bin of the histogram times the cloud fraction associated with each bin. Consistent with the changes made to the model formulation,

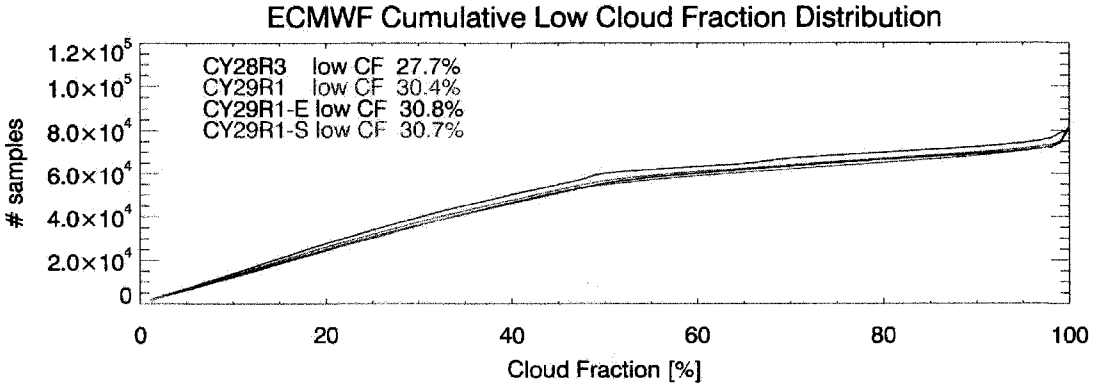

Fig. 5.13 Cumulative distribution of the model low cloud fraction histogram shown in Fig. 5.12. The low cloud fraction shown in the upper left corner is calculated as the product of the number of samples times the cloud fraction of each bin, divided by the total number of samples.

the low cloud fraction increases from CY28R3 to CY29R1 and the versions thereof. The total low cloud fraction of the models is 2% to 5% greater than in the GLAS observations, though. This seems to indicate that the model overestimates low cloudiness in all versions, and appears to contradict the results from the previous chapters.

In fact, these results are consistent: As shown in Table 5.6, the model generates low clouds more often than observed (about 12% higher frequency of occurrence). The majority of these clouds have low cloud fraction, though. The percentage of clouds with 95% or higher cloud fraction out of all unattenuated samples in the subtropical belt is

11.1% for GLAS. In the four model versions, this percentage is 6.0%, 9.0%, 9.5% and 11.3% (for CY28R3, CY29R1, -E, -S, respectively). Clearly, the increased number of high-fraction clouds is an improvement. It appears however that the model compensated for its lack of high-fraction clouds with more numerous low-fraction clouds. As a result, the model versions CY29R1 have an improved representation of high-fraction clouds, but an overabundance of low-fraction clouds, leading to a total low cloud fraction larger than observed.

5.3. GEOS model evaluation

5.3.1. Cloud type compositing

The GEOS model evaluation follows the same steps as the analysis of the ECMWF model. There are some notable differences however: The GEOS data are available on a 1° latitude by 1.25° longitude grid. Therefore the GLAS data, though identical to the data used above, must be averaged onto the new model grid. Consequently, the number of samples in the four regions is different as well. The new numbers are listed in Table 5.19. The frequency-of-occurrence maps (Fig. 5.56 through Fig. 5.61) also look slightly different since they now show the number of samples per 1°x1.25° grid box. For the GEOS runs, there is no information on particular parameterizations available. Instead, the model provides information about the source of the cloud properties (cloud liquid and ice water content, cloud fraction) by distinguishing between properties generated by the large-scale moisture scheme, and properties detrained by convective cores. Both GEOS runs (labeled "GEOS1" and "GEOS2") are intermediate steps toward a new and improved boundary layer scheme in GEOS-5, made available in the winter and spring of

2007. Unfortunately, details on these intermediate versions are not available, but nonetheless, improvement can be demonstrated from one version to the next.

Table 5.19 Number of 1°x1.25° grid columns transected by a GLAS track in the four regions, and over ocean.

Region	Number of Samples
ALL	25036
NEP	5144
SEP	11413
AF	5394
AUS	3085

The cloud type categories are essentially the same as those used for the ECMWF model. Since there is no special boundary layer scheme used to produce stratocumulus-type clouds, the cloud type criteria are treated as for category *Sc2* above, i.e. the model's low cloud fraction ("LCC", cloudiness below 700 hPa) and the topmost cloudy layer height ("CCTop") are used to sort each sample.

In the regional average, GLAS observes 30.4% *Sc*-type clouds, and 43.1% *TCu*-type clouds, for a total of 73.5% (Table 5.20). GEOS1 produces 32.% *Sc* and 52.7% *TCu*.

Table 5.20 Percentage of samples in all four regions that are classified as *Sc*, *TCu*, or in either one of the two categories (total).

ALL	% *Sc*	% *TCu*	% total
GLAS	30.4	43.1	73.5
GEOS1	32.0	52.7	84.7
GEOS2	24.7	50.6	75.3

However, a look at the cloud top height distribution of the GEOS1 run shows a large number of clouds with very low cloud top, both in the *Sc* category (Fig. 5.64) and the *TCu* category (Fig. 5.65). In the middle panel of Fig. 5.14, two measures of the BL height are plotted. "PBLTop" is the boundary layer height as calculated using Lock's

scheme (Lock at al. 2000) at every time step. "DiagBLH" is a diagnostic measure of the boundary layer height. The two measures seem to be almost identical, apart from a shift by half a model layer. Presumably, one of the two BL measures identifies the layer edge as the BL top, while the other identifies the layer center. However, both BL measures show the same peak at very low boundary layer heights as are seen in the cloud top distribution.

Fig. 5.15 shows the composite *Sc* profiles of cloud fraction and cloud liquid water content in the middle and right panels. The profiles show the largest values close to the

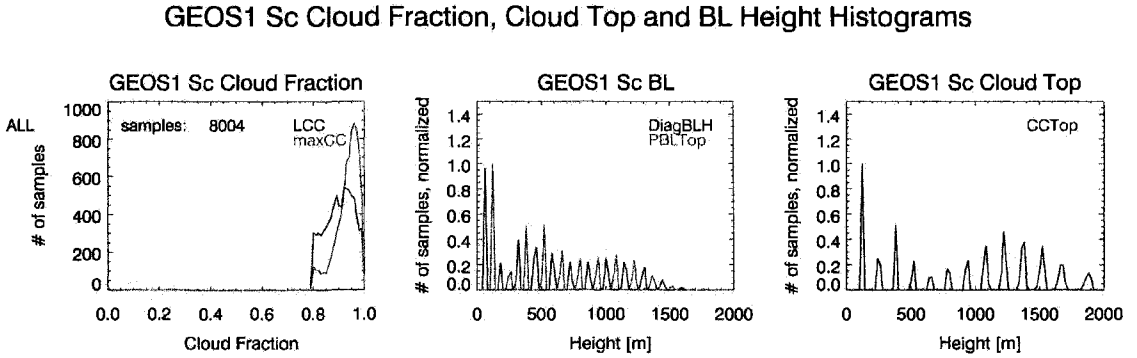

Fig. 5.14 Histogram of cloud fraction, cloud base height and cloud top height for all GEOS1 samples classified as *Sc*. The number of samples classified as *Sc* in all four regions is printed in the upper left corner of the left panel. The variable abbreviations used in the labels the same as those in Fig. 5.4.

surface. Apparently, a significant fraction of the *Sc*-type samples is in fact fog sitting directly on the ocean surface. While fog is commonly observed along the Californian coast, it is usually confined to the near-costal areas. Ship track observations cannot confirm the existence of fog in the South East Pacific, for example (EPIC, Bretherton et al. 2004). In the case of GEOS1, samples with fog are not confined to the coastal regions, but appear throughout the four regions (Fig. 5.58). The large-scale moisture

scheme seems to contribute more to this problem than the convective scheme (right panel Figure Fig. 5.15).

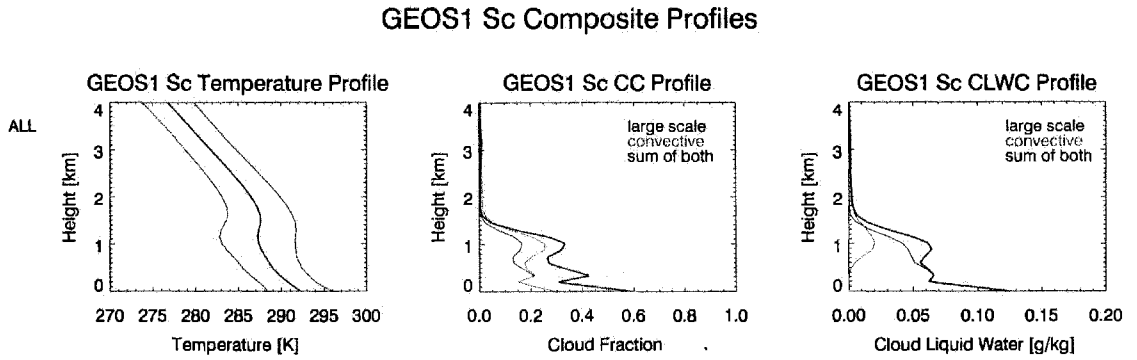

Fig. 5.15 Composite profiles of temperature, cloud fraction and cloud liquid water content for all GEOS1 samples classified as *Sc*. In the left panel, the thick line is the average, and the plus/minus one standard deviation range is marked by the thin lines. In the middle and right panel, the contributions to the total (green) from the convective cores (red) and the large scale moisture scheme (blue) are shown separately.

The major improvement from version GEOS1 to version GEOS2 in this model is the reduction of these fog clouds. Fig. 5.16 shows clearly that almost all of the very low cloud tops are gone in *Sc*. The peaks in the BL height and cloud top height distributions are clearly elevated now, and sit around 1000 m and 1200 m respectively. A similar improvement can be seen for the *TCu* category (Fig. 5.65 and Fig. 5.67).

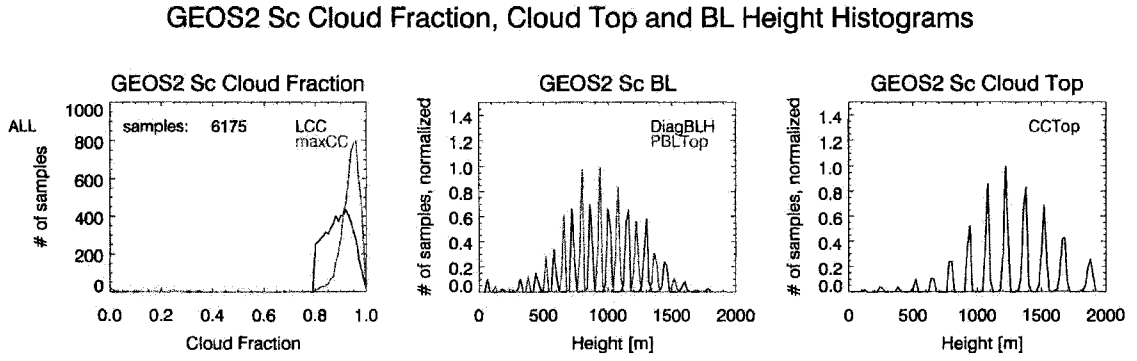

Fig. 5.16 Same as Fig. 5.14, but for samples from GEOS2.

As Fig. 5.17 illustrates, the cloud fraction and liquid water maxima are now raised well above the surface at around 1 km. Without the fog, the percentage of both *Sc* and

TCu samples shrinks to 24.7% and 50.6%, respectively (Table 5.20). While GEOS2 produces about 6% fewer *Sc* samples than observed by GLAS, the cloud top height distribution is quite good and captures most of the regional differences (Fig. 5.62 and Fig. 5.65). In the *TCu* category, GEOS2 captures the cloud top distributions quite well in all but the SEP region (Fig. 5.63 and Fig. 5.66).

For some reason, the GEOS model rarely ever generates full cloud cover in the four regions (Fig. 5.64 and Fig. 5.66). Also notable is that there are quite a few instances in the *TCu* category where the low cloud cover "LCC" (cloud fraction below 700 hPa) is less than 80%, but the three-dimensional cloud fraction below 3 km is greater than 80% (Fig. 5.65 and Fig. 5.67). The three-dimensional cloud fraction is split into the fraction generated by the large-scale scheme, and the fraction generated by the convective scheme, though the sum of both is considered when searching for the highest cloud fraction in the layers below 3 km ("maxCC")..

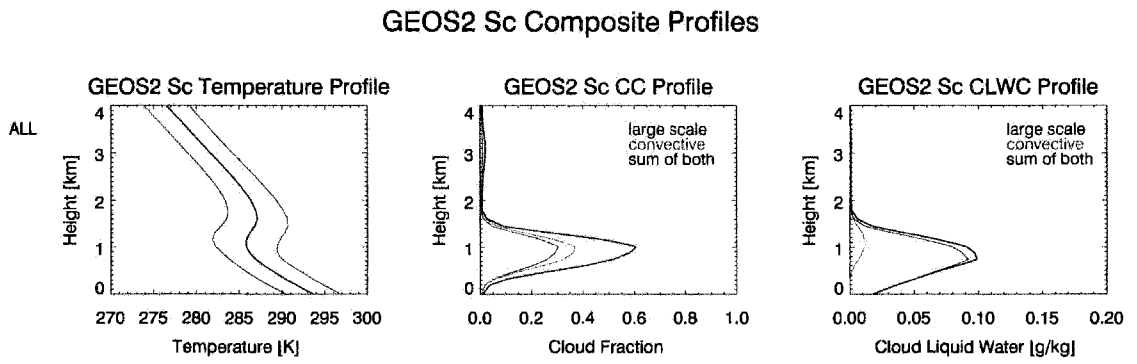

Fig. 5.17 Same as Fig. 5.15, but for samples from GEOS2.

Fig. 5.64 through Fig. 5.71 show the histograms and composite profiles of both *Sc* and *TCu* categories for all regions, and both model versions.

5.3.2. Low cloud fraction in the tropical-subtropical belt

The low cloud fraction in the tropical-subtropical belt calculated from GLAS uses the highest cloud fraction found below 700 hPa in the observations, in order to be consistent

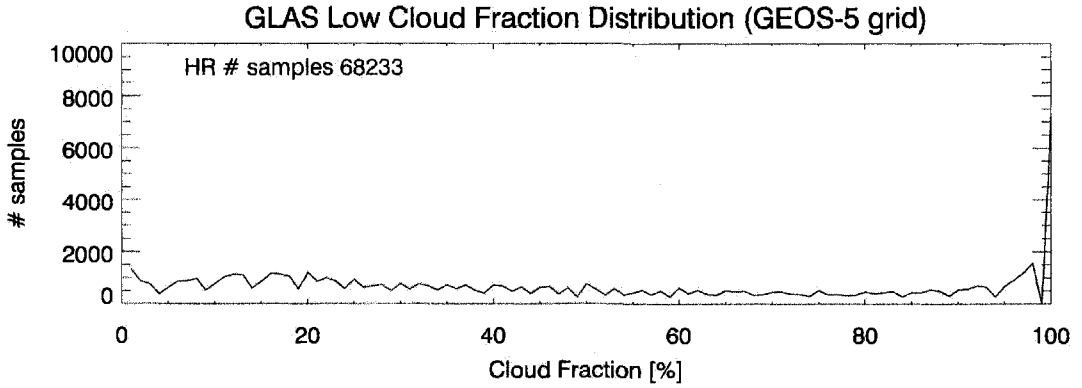

Fig. 5.18 Same as Fig. 5.10, but for a HR GLAS cloud fraction calculated on the GEOS-5 grid.

with the definition of the low cloud fraction (LCC) in the GEOS-5 model. As with the ECMWF model, only unattenuated samples are included.

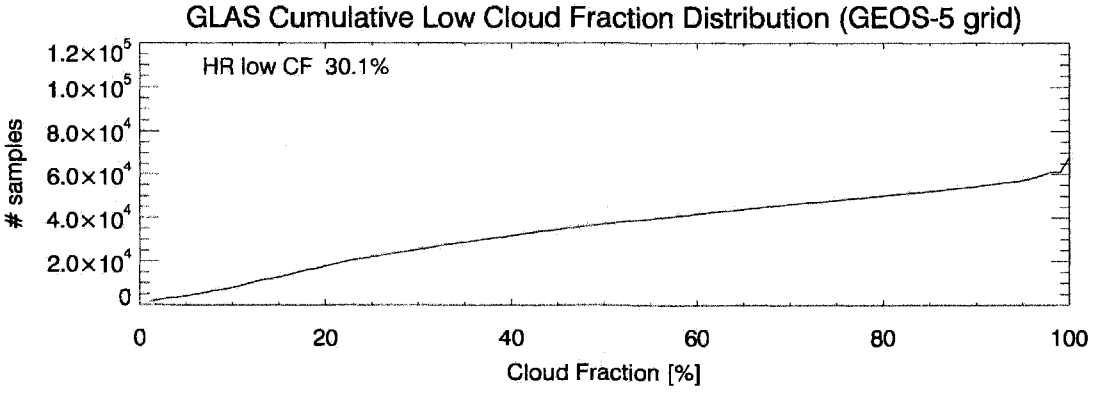

Fig. 5.19 Same as Fig. 5.11, but for a HR GLAS cloud fraction calculated on the GEOS-5 grid.

Out of the total number of intersected model columns (144,532), 78.5% are unattenuated in GLAS. In GEOS1, this fraction is 67.7%, in GEOS2 it is 78.0%. Apparently, about 10% more samples are flagged as attenuated below 700 hPa in GEOS1, compared to version GEOS2. Out of the unattenuated columns, both GEOS-5

versions have a large number of samples with cloud fractions 10% and less. In fact, the cumulative distribution in Fig. 5.21 shows that the two model runs vary almost exclusively in the number of low-fraction (<10%) samples, though a small reduction in high-fraction samples is also apparent in GEOS2. While most high-fraction samples are

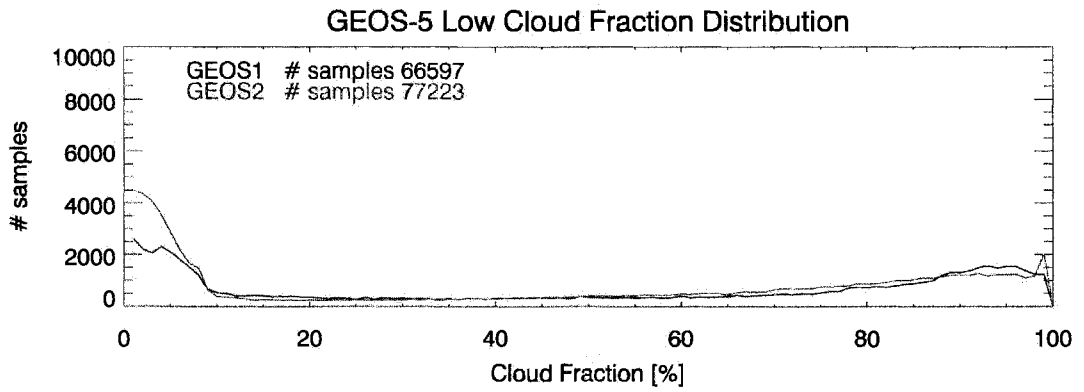

Fig. 5.20 Same as Fig. 5.12, but for the two runs of the GEOS-5 model.

found at cloud fractions above 95% in GLAS, both models lack samples with 100% fraction, but have too many samples in the range between 75% and 95%.

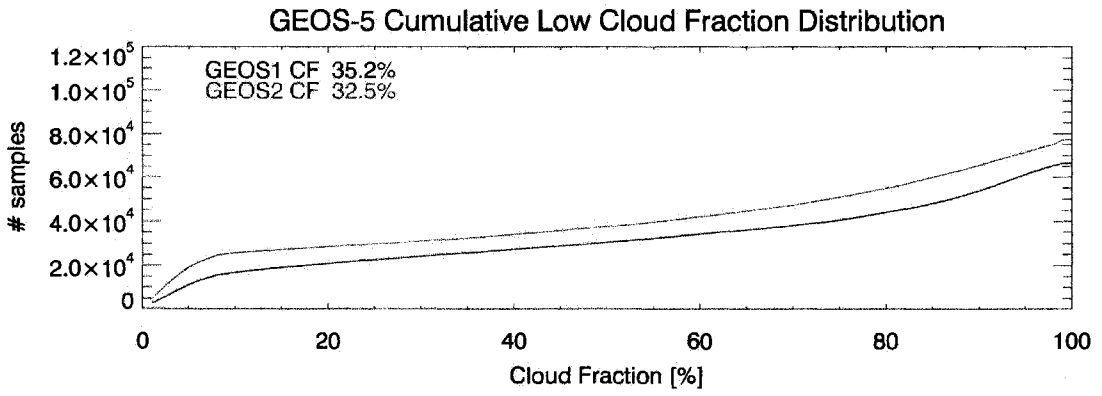

Fig. 5.21 Same as Fig. 5.13, but for the two runs of the GEOS-5 model.

The number of samples in Fig. 5.18 and Fig. 5.20 refers to the total number of samples in the distribution, excluding the lowest bin (0 to 1%). In the observations, this number corresponds to 60.2% of the unattenuated samples. In the two model versions, the percentages are 68.1% (GEOS1) and 68.54% (GEOS2). This shows that both model

versions produce clouds with fractions above 1% more often than observed. As a result, the average low cloud fraction across the subtropical belt in the two model versions is greater by 5.1% (GEOS1) and 2.4% (GEOS2) than in the observations. A combination of fewer cloud samples and a better cloud fraction distribution would be necessary to match the GLAS observations.

5.4. Summary

The model evaluation described in this chapter shows that version CY28R3 of the ECMWF model underestimates the frequency of occurrence and cloud fraction of stratocumulus clouds in the eastern part of the ocean basins. The height of the modeled stratocumulus clouds is on average 300 m lower than observed.

With the introduction of the EDMF scheme (CY29R1), stratocumulus clouds become more frequent and have higher cloud fraction, which is an improvement over the previous model version. However, the top height of these clouds is underestimated even more severely (~500 m), and stratocumulus clouds still occur less frequently than observed.

Weakening the environmental mixing of the lifted test parcel in the EDMF scheme (CY29R1-E) improves the average cloud top height of the modeled stratocumulus clouds somewhat, but a discrepancy of 200 to 300 m remains. Relaxing the lower atmospheric stability criterion (CY29R1-S) leads to a frequency of occurrence of high-fraction clouds comparable to those observed.

The analysis also shows that the ECMWF model in all versions produces an over-abundance of low-fraction clouds, leading to an overestimation of low cloudiness in the subtropical belt.

Clouds generated by the model's shallow convective scheme appear to have a built-in and artificial preference for cloud fractions less than 50%. The EDMF, on the other hand, produces a distribution of cloud fractions comparable to that observed.

All versions of the ECMWF model are able to qualitatively capture regional differences in the frequency of occurrence and top height of marine boundary layer clouds.

The evaluation of the GEOS-5 model shows an excess of fog in the first version of the model (GEOS1), together with a higher-than-observed frequency of occurrence of low clouds. The number of fog clouds is greatly reduced in the second version (GEOS2), where most clouds are elevated off the ocean surface with cloud-top levels in good agreement with observations. However, both model versions have a strong preference for clouds with small fraction (<10%) and an avoidance of large cloud fraction (90%). These may be related to artificial conditional statements in the model code. The errors in the cloud fraction distribution, together with a higher-than-observed fraction of cloudy samples, leads to an overestimate of total low cloudiness in the subtropical belt compared to GLAS observations.

5.5. Figures

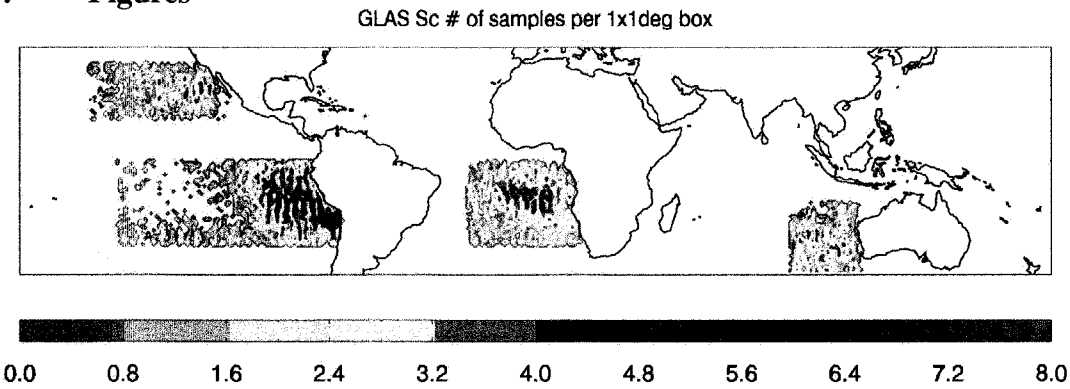

Fig. 5.22 Number of GLAS samples per 1°x1° grid box classified as *Sc*.

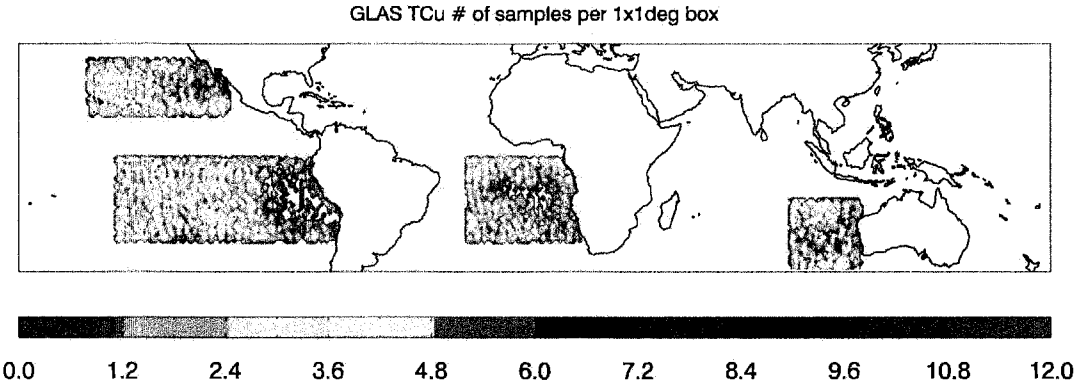

Fig. 5.23 Number of GLAS samples per 1°x1° grid box classified as *TCu*.

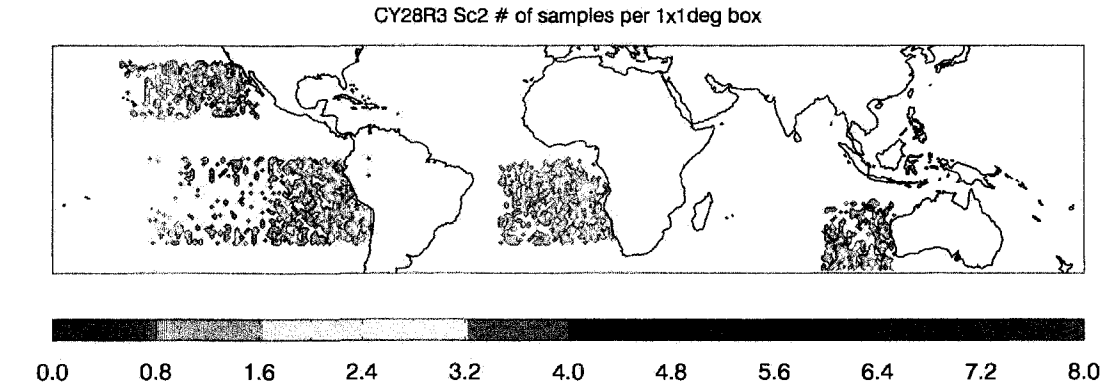

Fig. 5.24 Number of samples per 1°x1° grid box classified as *Sc2* from the ECMWF model run CY28R3.

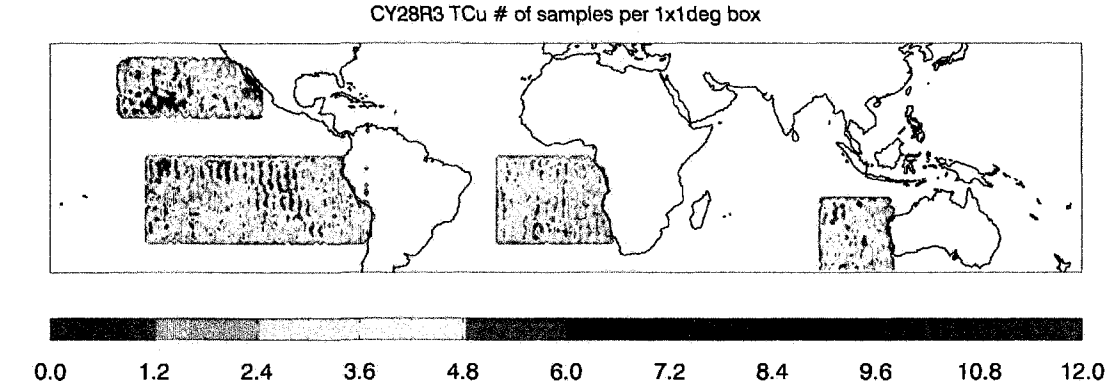

Fig. 5.25 Number of samples per 1°x1° grid box classified as *TCu* from the ECMWF model run CY28R3.

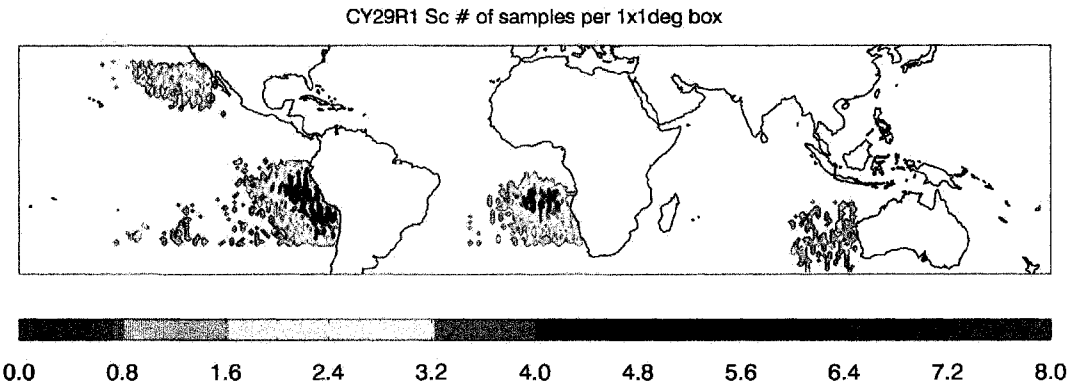

Fig. 5.26 Number of samples per 1°x1° grid box classified as *Sc* from the ECMWF model run CY29R1.

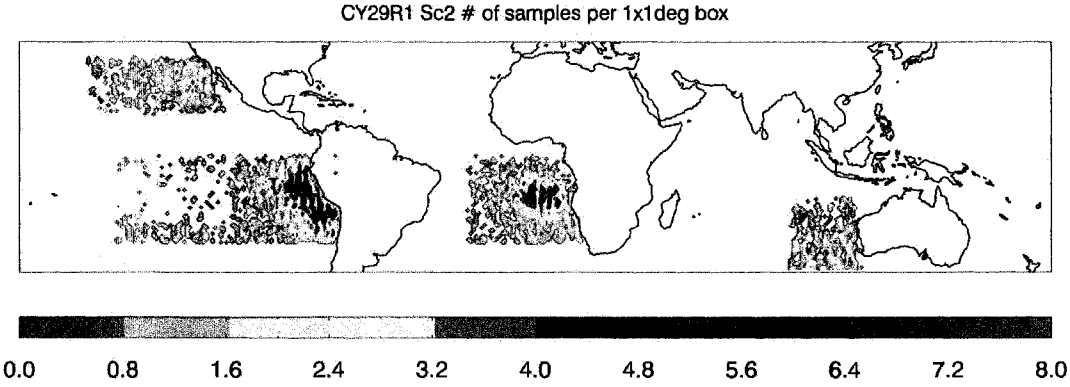

Fig. 5.27 Number of samples per 1°x1° grid box classified as *Sc2* from the ECMWF model run CY29R1.

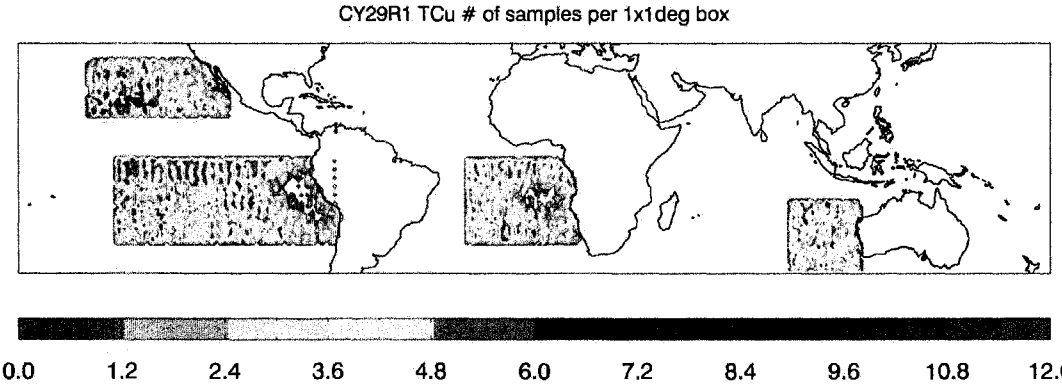

Fig. 5.28 Number of samples per 1°x1° grid box classified as *TCu* from the ECMWF model run CY29R1.

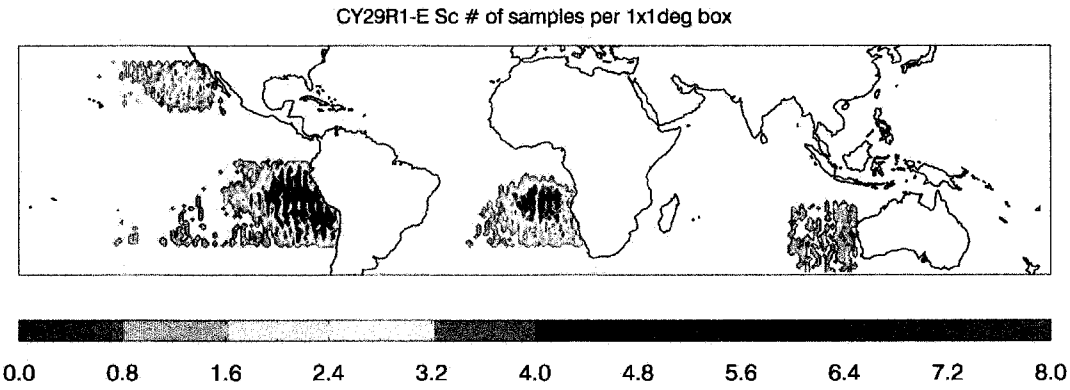

Fig. 5.29 Number of samples per 1°x1° grid box classified as *Sc* from the ECMWF model run CY29R1-E.

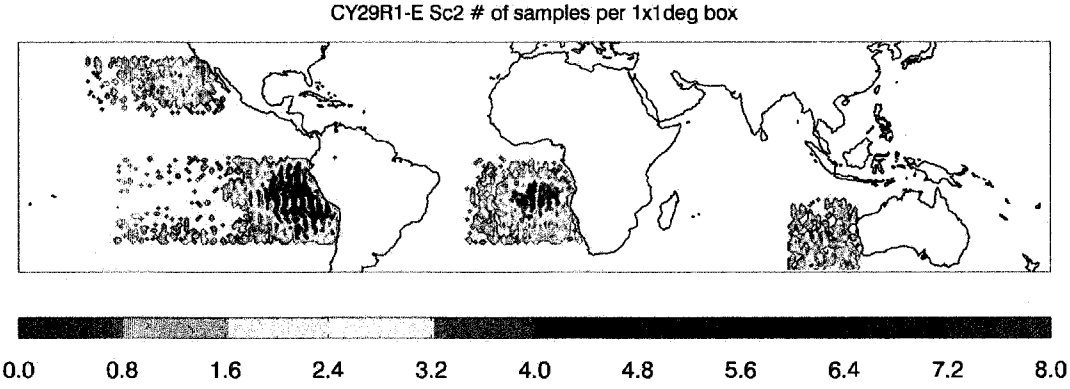

Fig. 5.30 Number of samples per 1°x1° grid box classified as *Sc2* from the ECMWF model run CY29R1-E.

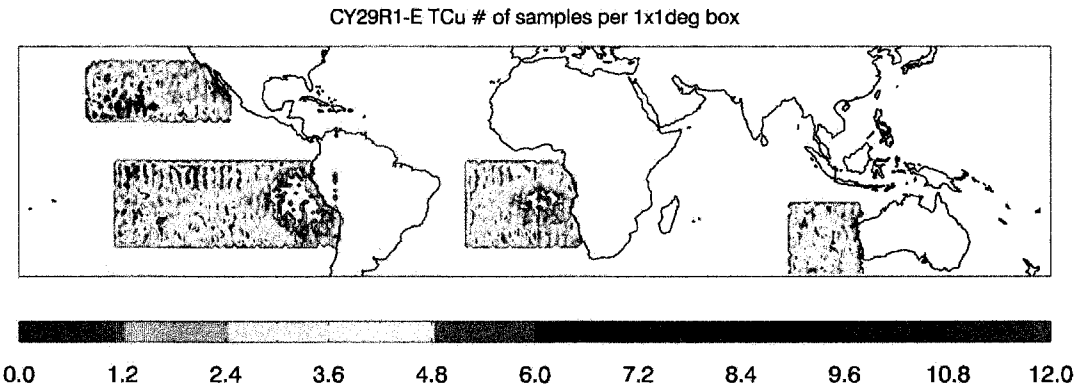

Fig. 5.31 Number of samples per 1°x1° grid box classified as *TCu* from the ECMWF model run CY29R1-E.

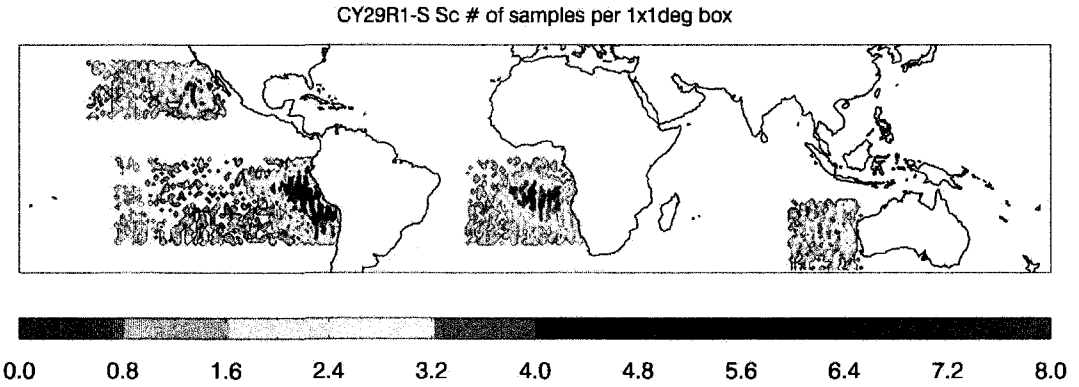

Fig. 5.32 Number of samples per 1°x1° grid box classified as *Sc* from the ECMWF model run CY29R1-S.

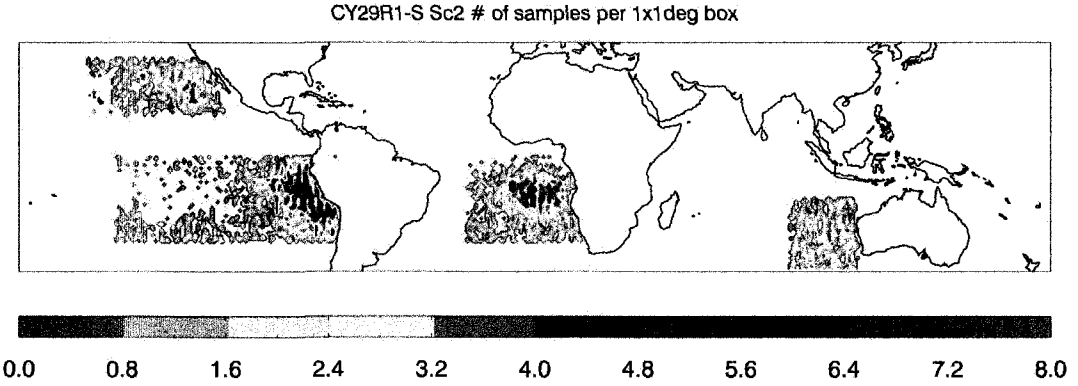

Fig. 5.33 Number of samples per 1°x1° grid box classified as *Sc2* from the ECMWF model run CY29R1-S.

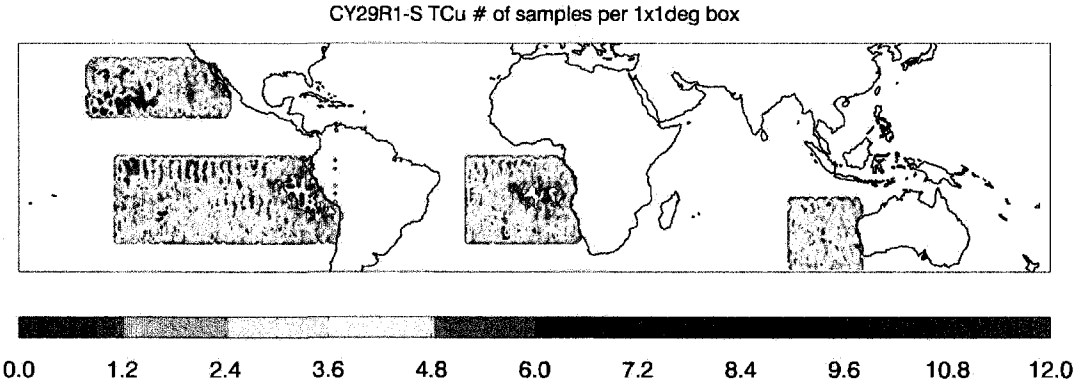

Fig. 5.34 Number of samples per 1°x1° grid box classified as *TCu* from the ECMWF model run CY29R1-S.

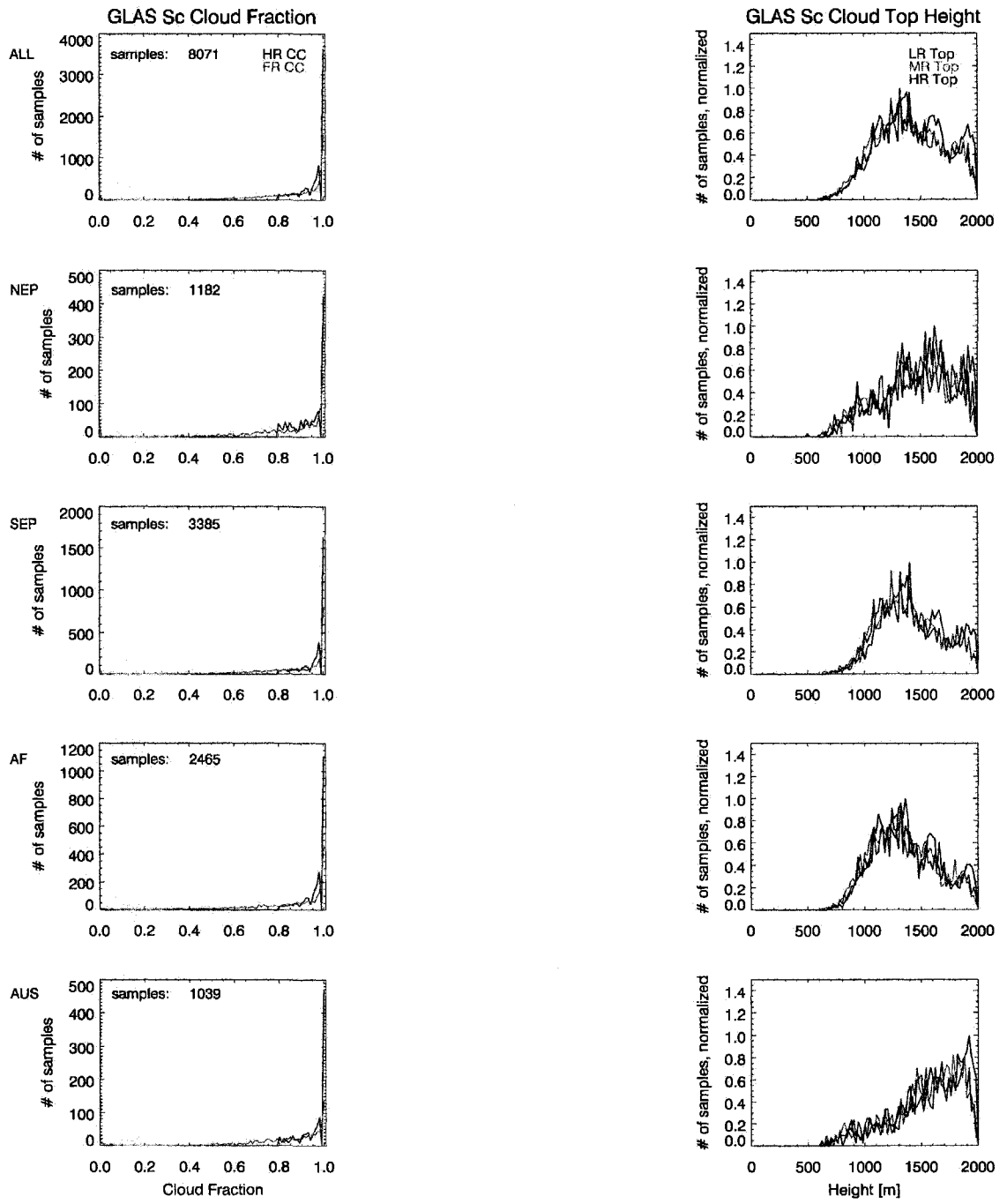

Fig. 5.35 Histogram of cloud fraction and cloud top height for GLAS samples classified as *Sc*. The first row shows histograms for samples from all regions, the following rows for samples from the individual regions. The number of samples is shown in the upper left corner of the left panels. "HR CC" and "FR CC" refers to the cloud fraction calculated from HR and FR GLAS data, respectively. "LR Top", "MR Top" and "HR Top" refers to the grid-point average cloud top height calculated from the LR, MR and HR GLAS data products.

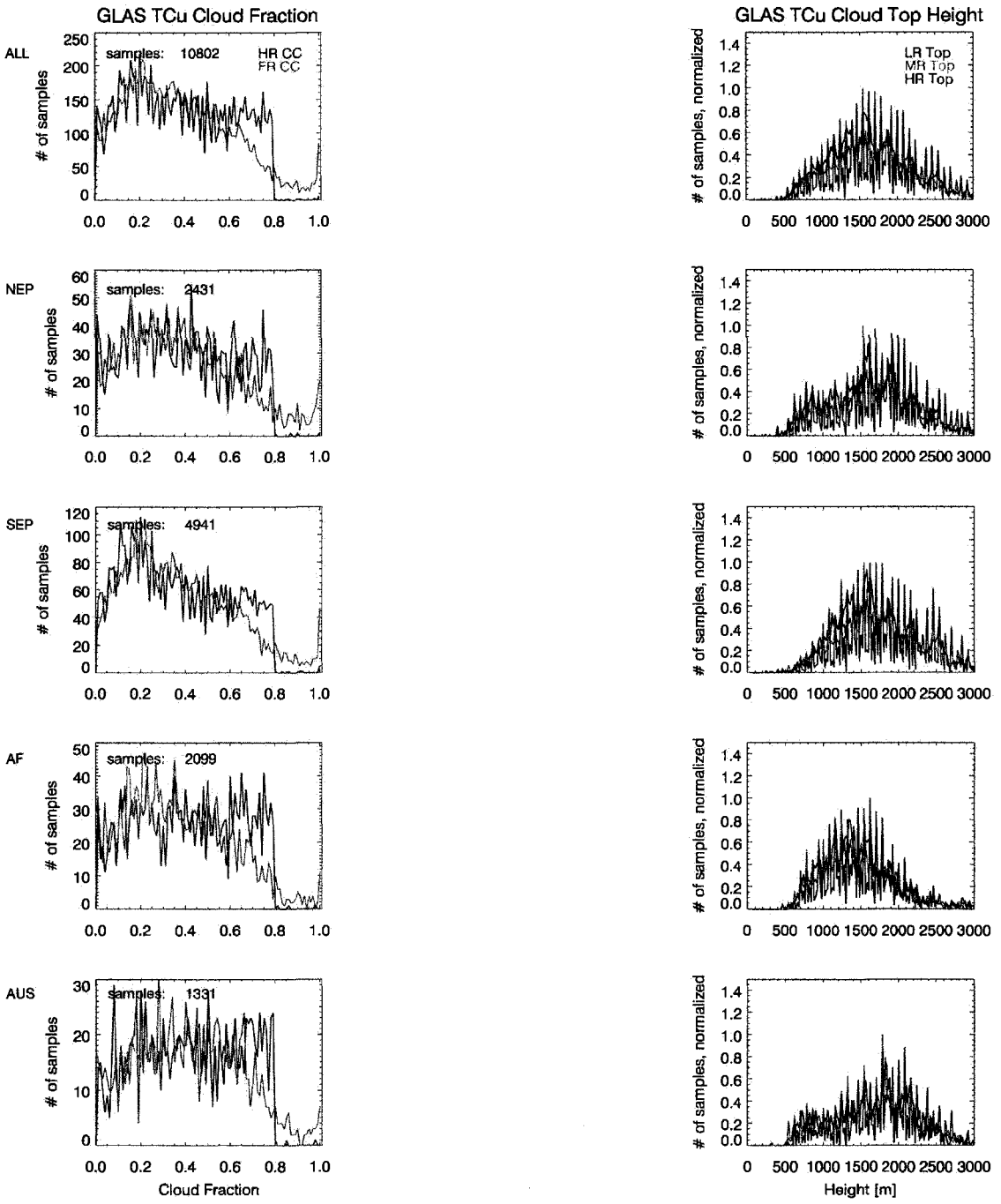

Fig. 5.36 Same as Fig. 5.35, but for samples classified as *TCu*.

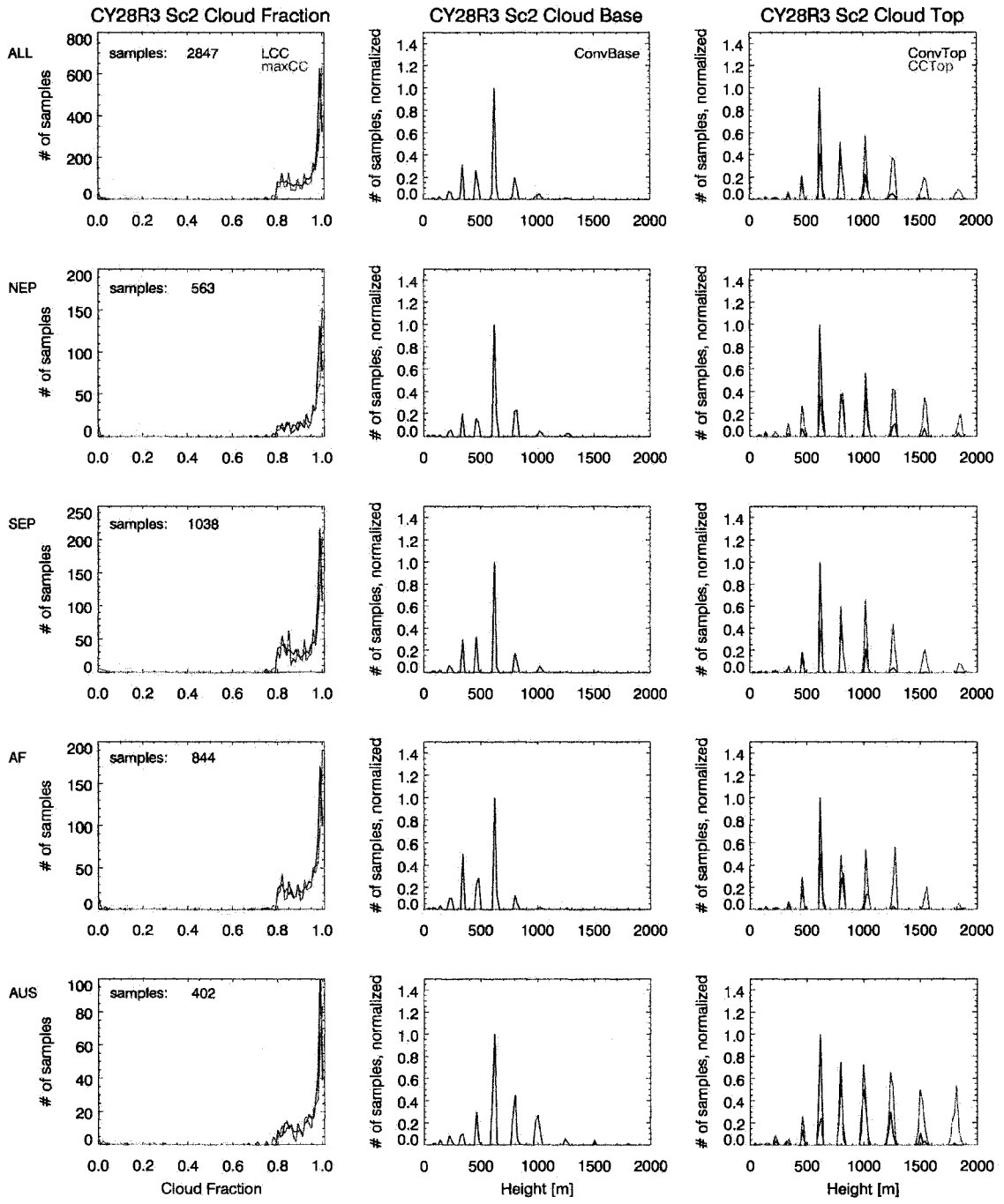

Fig. 5.37 Histogram of cloud fraction, cloud base height and cloud top height for CY28R3 samples classified as *Sc2*. Histograms for all samples are shown in the first row, for individual regions in rows two through 5. The number of samples classified as *Sc2* in all four regions is printed in the upper left corner of the left panel. The variable abbreviations used in the labels are explained in detail in section 5.2.1.

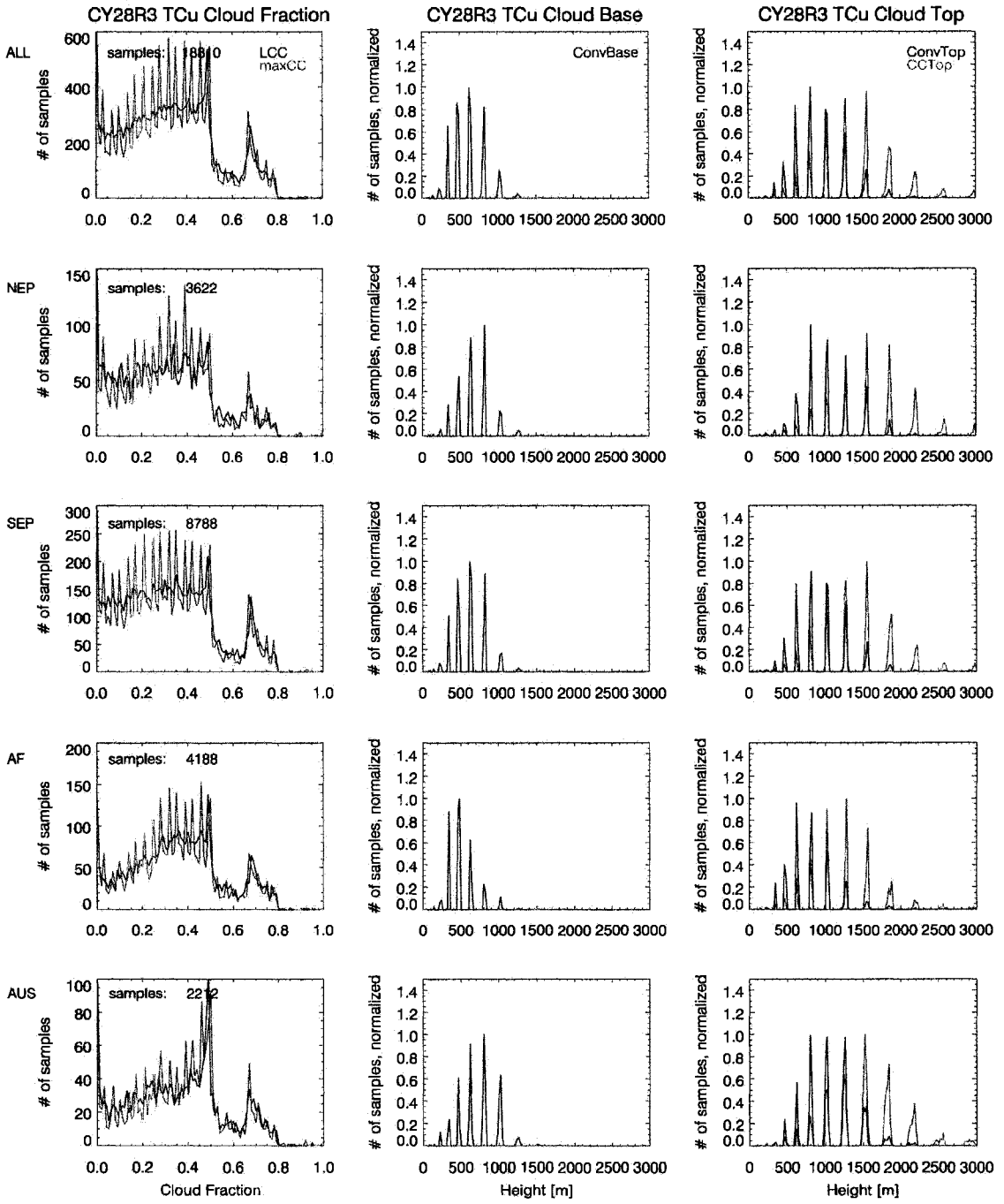

Fig. 5.38 Same as Fig. 5.37, but for samples classified as *TCu*.

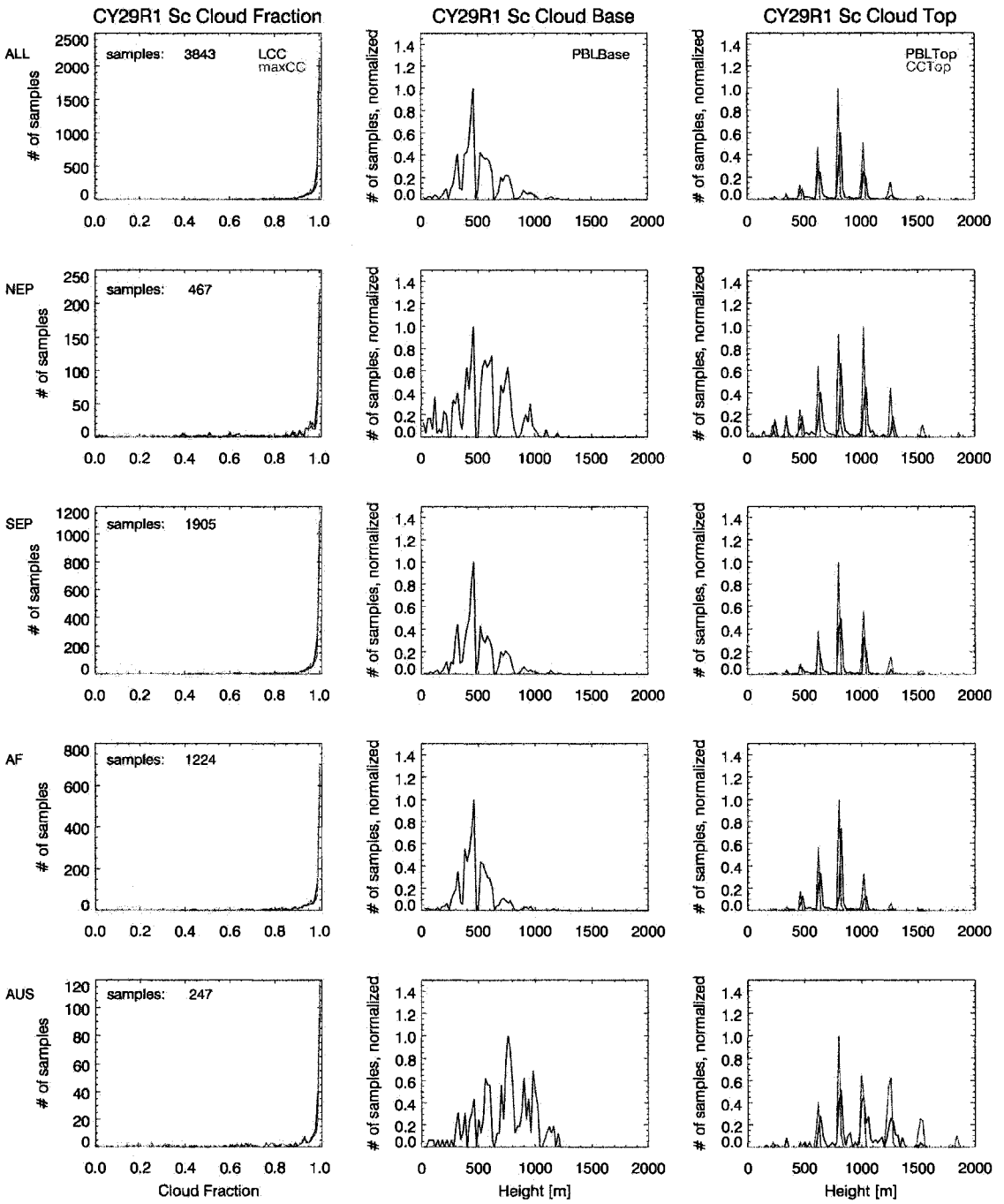

Fig. 5.39 Histogram of cloud fraction, cloud base height and cloud top height for CY29R1 samples classified as *Sc*. Histograms for all samples are shown in the first row, for individual regions in rows two through five. The number of samples classified as *Sc* in all four regions is printed in the upper left corner of the left panel. The variable abbreviations used in the labels are explained in detail in section 5.2.1.

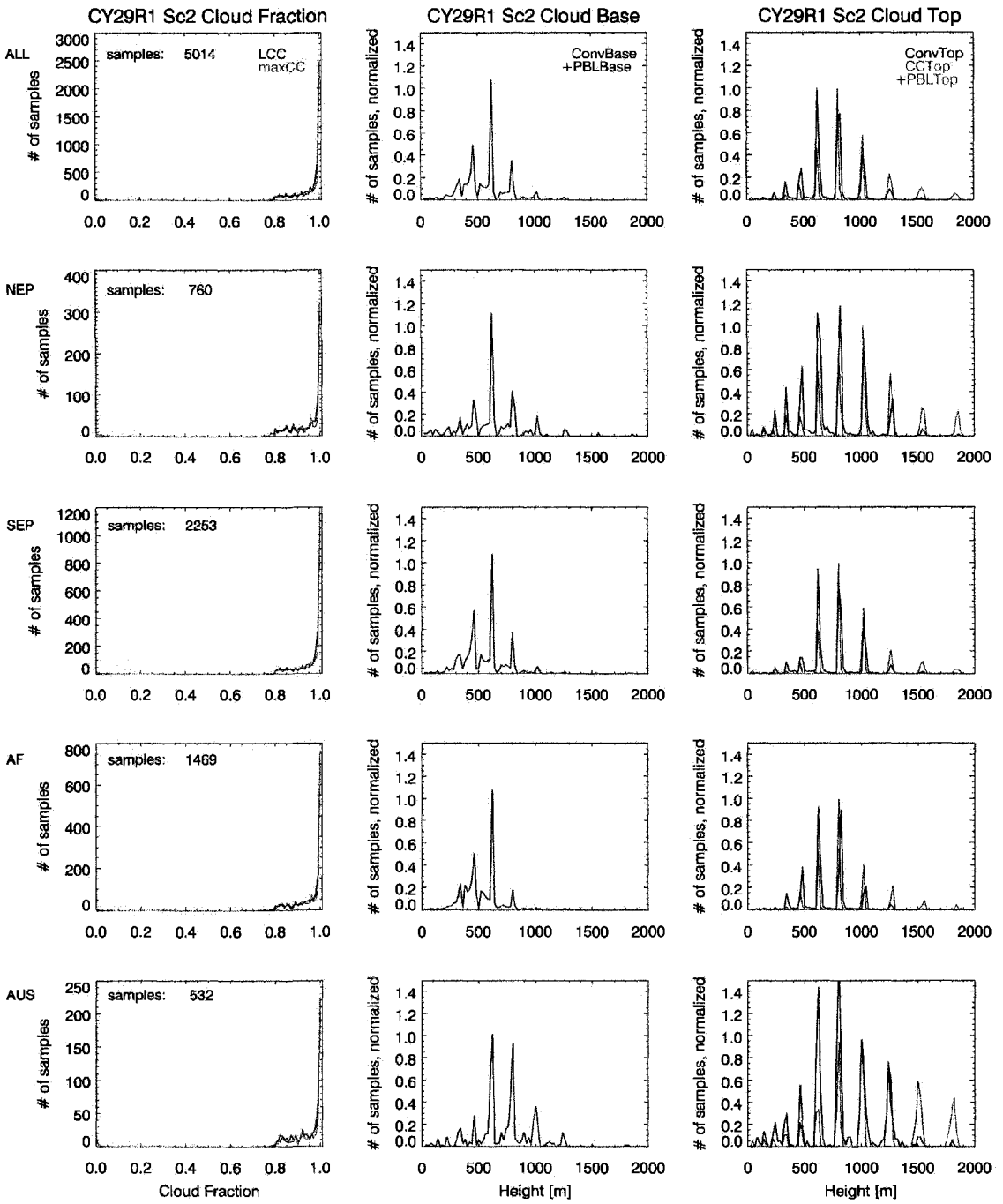

Fig. 5.40 Histograms of cloud fraction, cloud base height and cloud top height for all samples classified as Sc2 in CY29R1. Variables "LCC", "maxCC" and "ConvTop" as in the previous figures. Since the *Sc2* category includes samples generated by the EDMF, and samples generated by the convective schemes, the cloud base histograms in the middle column include the cloud base height ("PBLBase") in case the sample is generated by the EDMF, and the convection base height ("ConvBase") in case the sample is generated by the convective schemes. Similarly, the cloud top height in the right column includes the BL height ("PBLTop") and the height of the topmost cloudy layer ("CCTop").

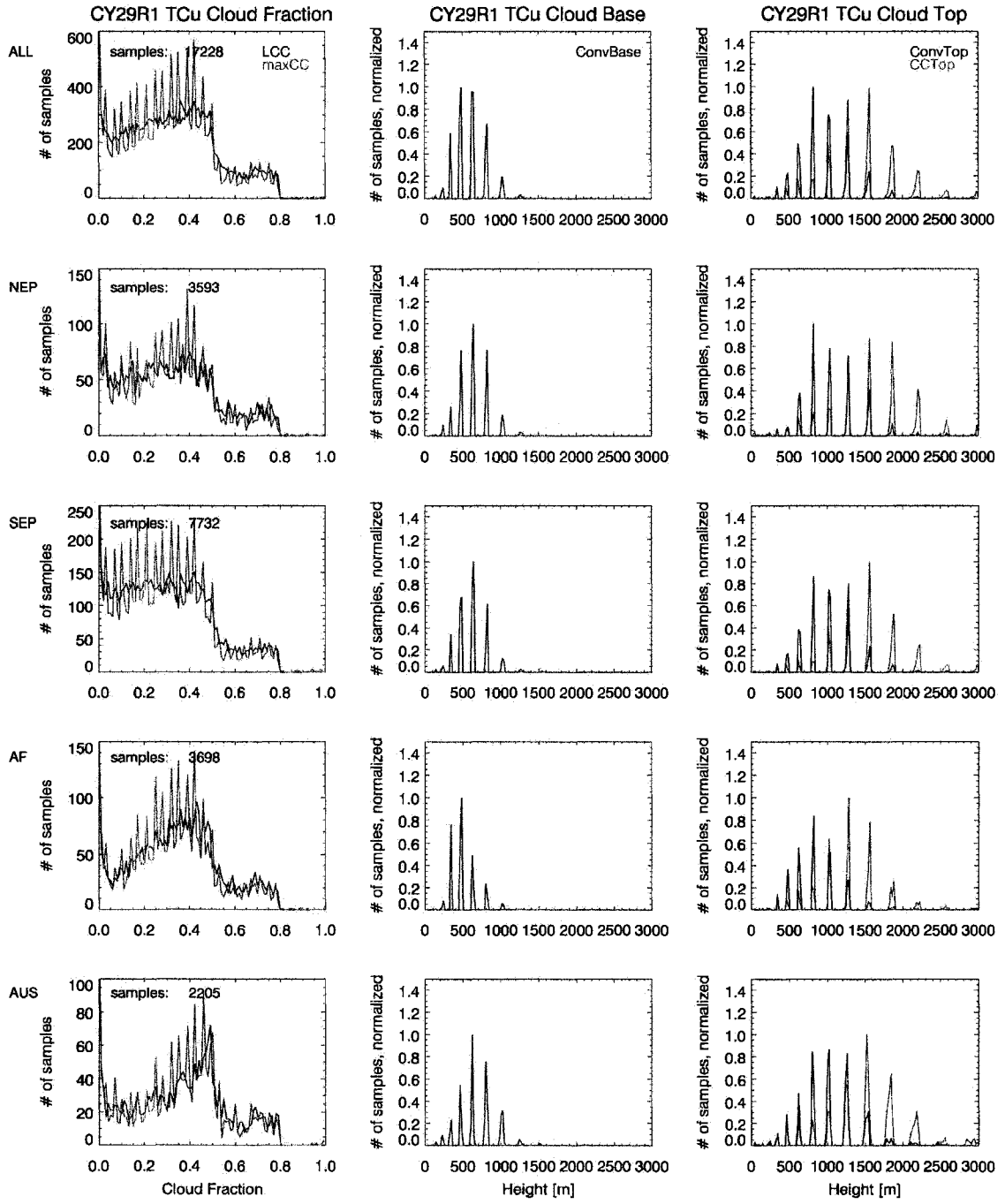

Fig. 5.41 Same as Fig. 5.37, but for CY29R1 samples classified as *TCu*.

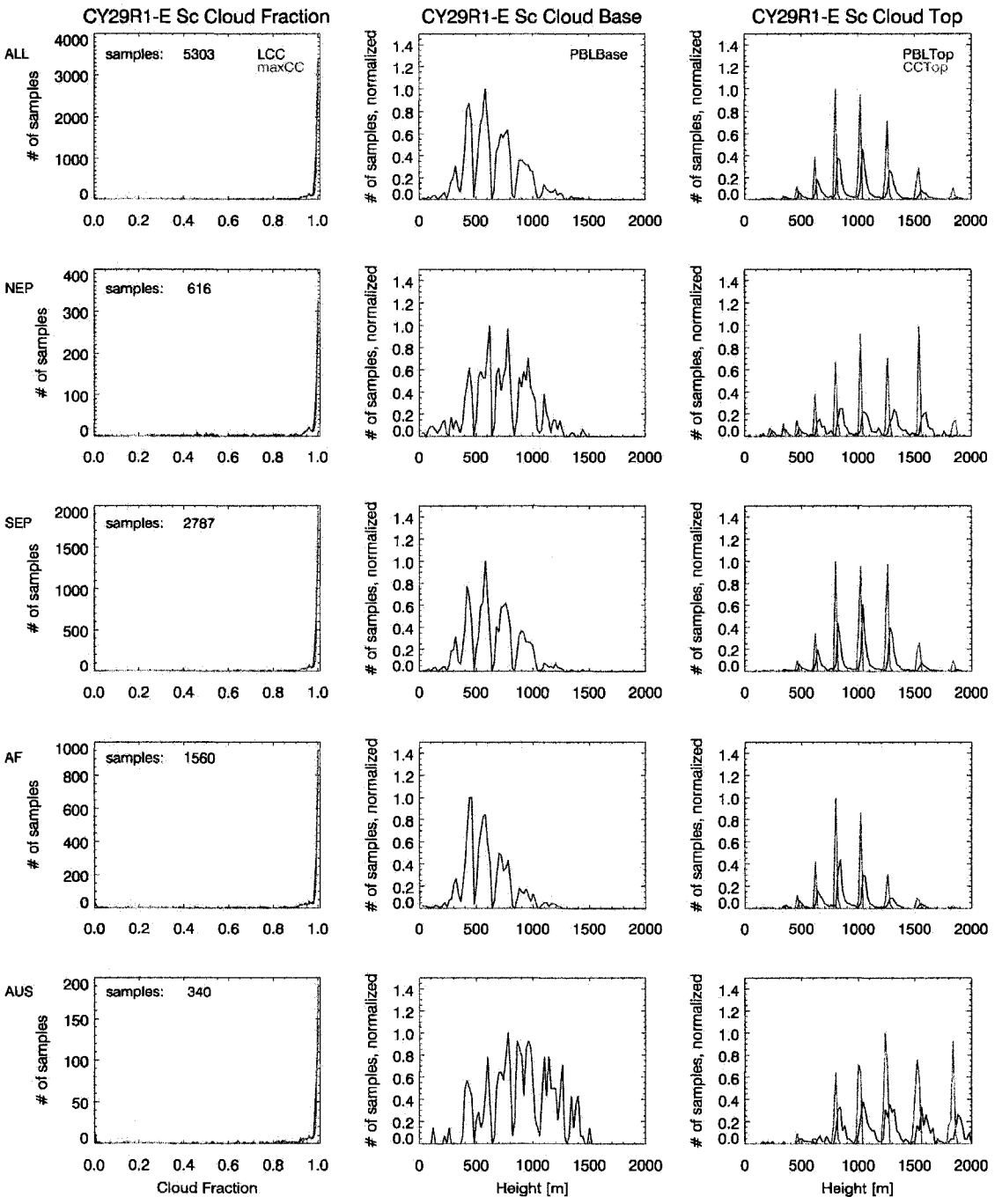

Fig. 5.42 Same as Fig. 5.39, but for CY29R1-E samples.

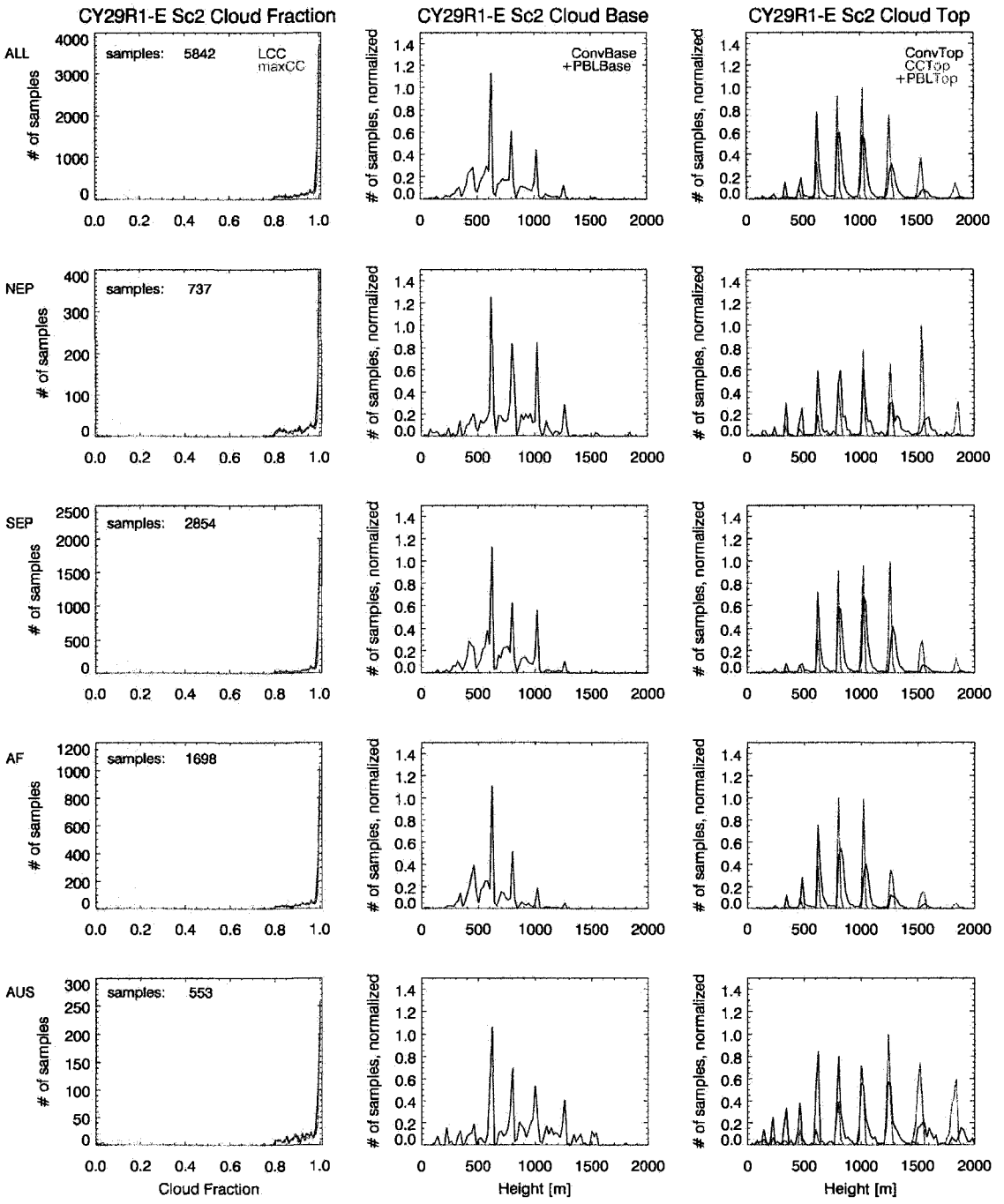

Fig. 5.43 Same as Fig. 5.40, but for CY29R1-E samples.

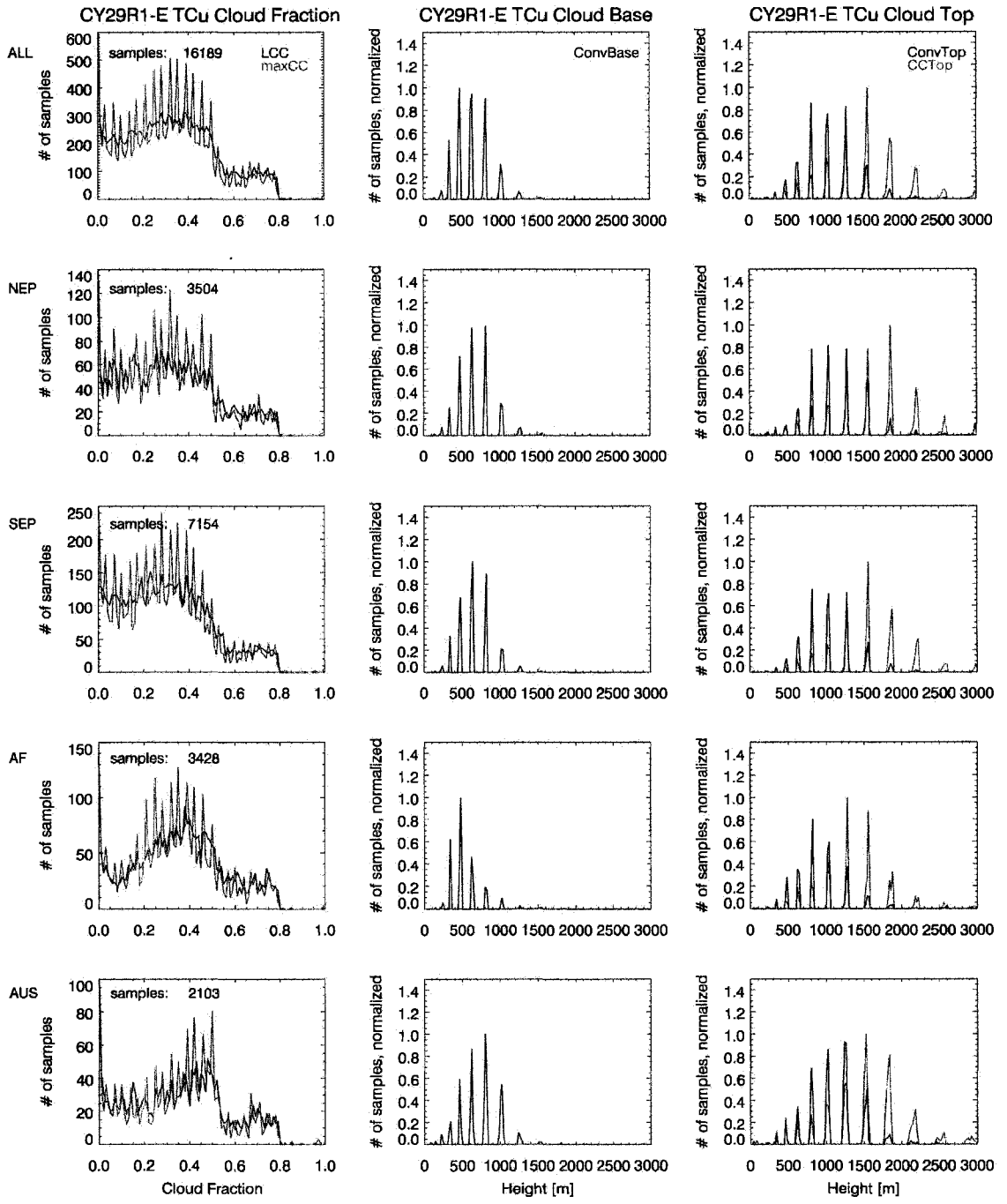

Fig. 5.44 Same as Fig. 5.37, but for CY29R1-E samples classified as *TCu*.

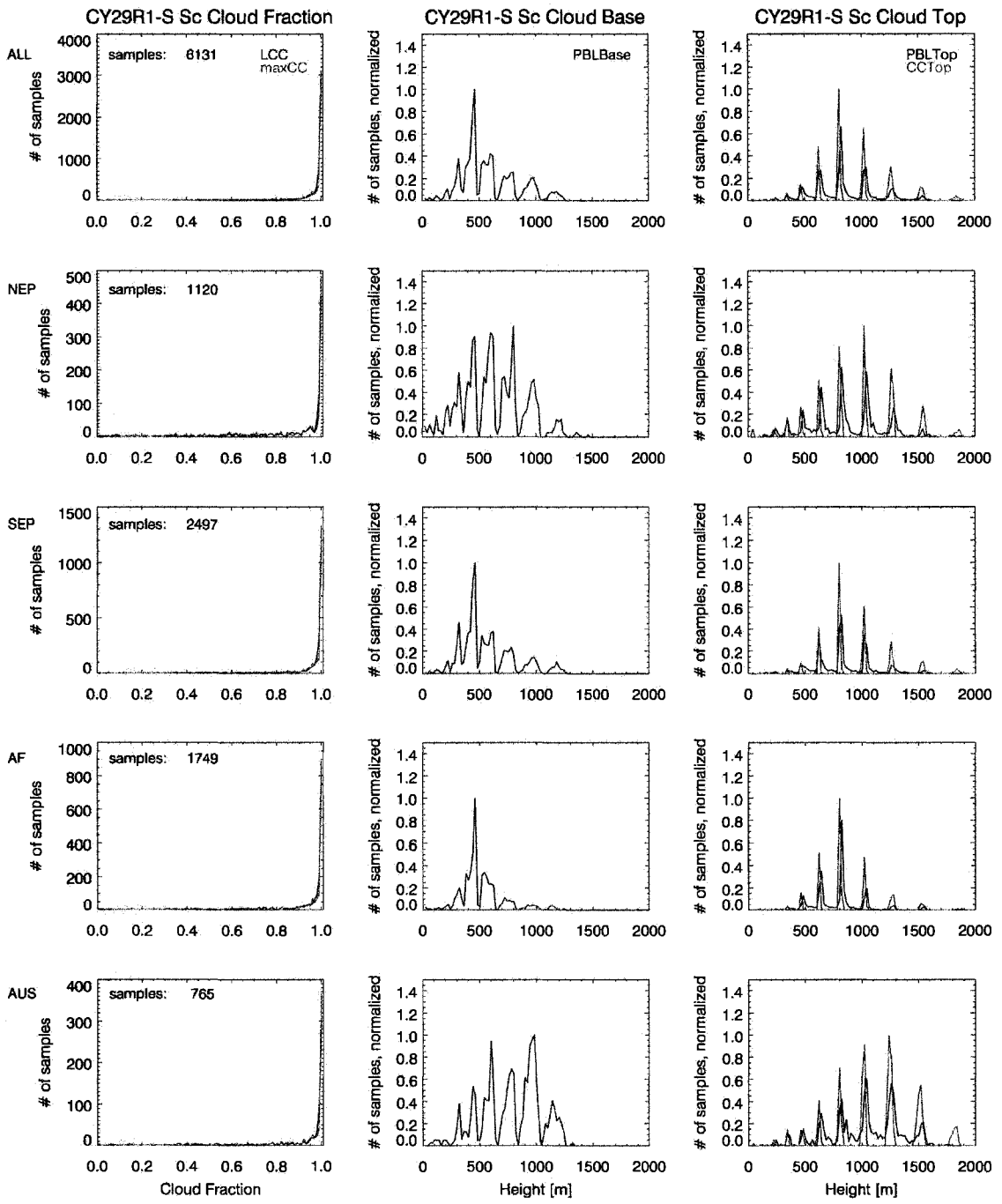

Fig. 5.45 Same as Fig. 5.39, but for CY29R1-S samples.

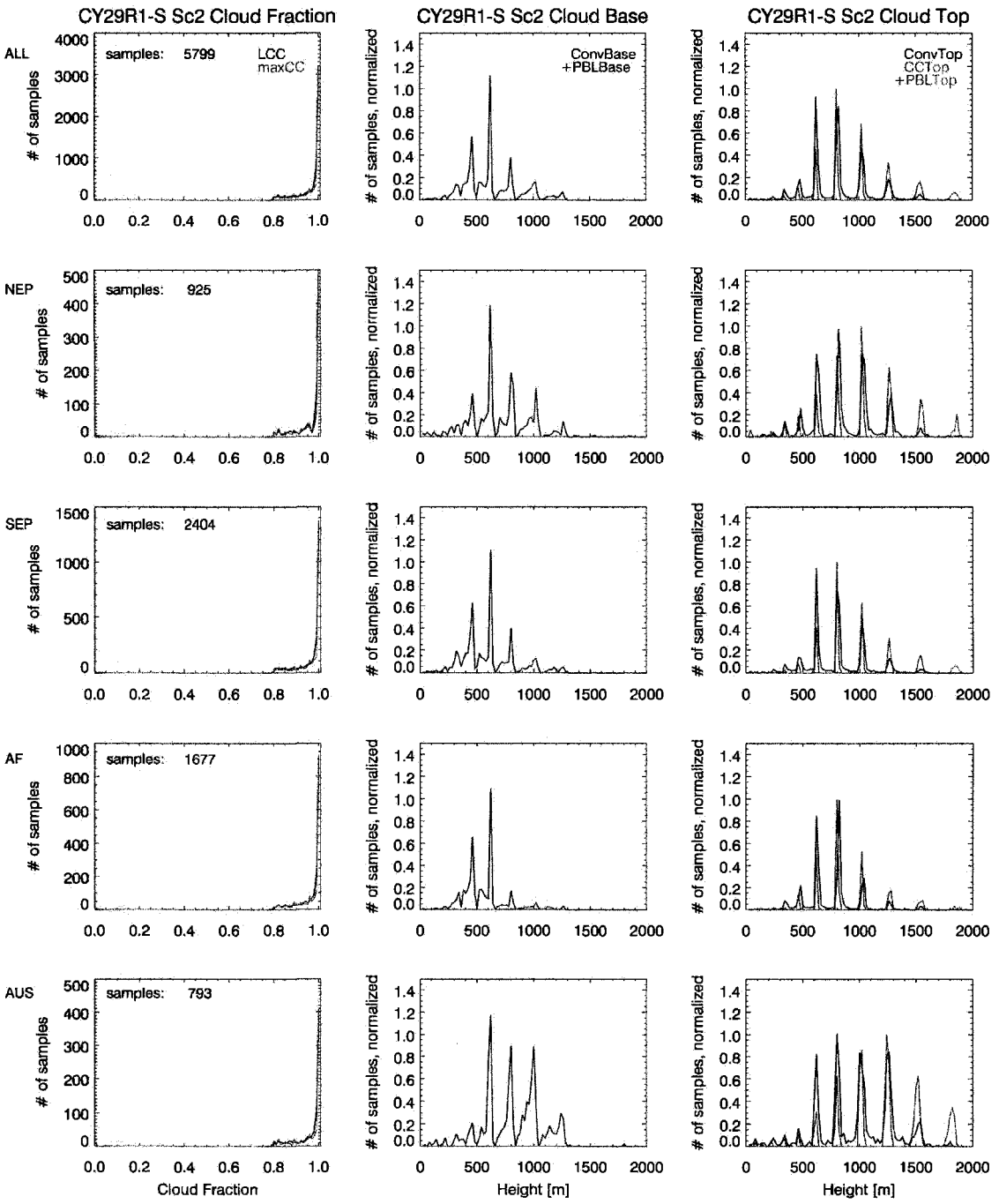

Fig. 5.46 Same as Fig. 5.40, but for CY29R1-S samples.

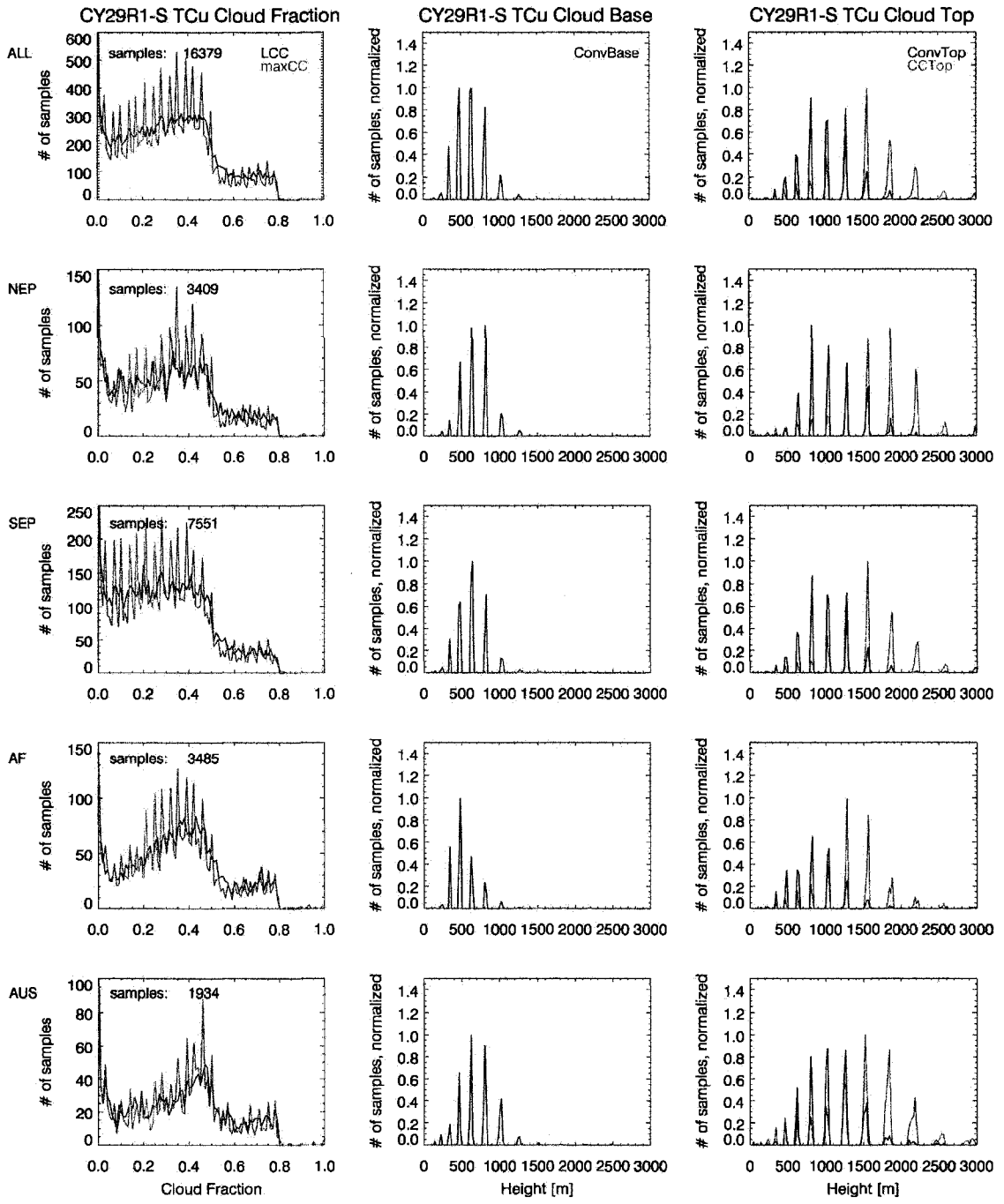

Fig. 5.47 Same as Fig. 5.37, but for CY29R1-S samples classified as *TCu*.

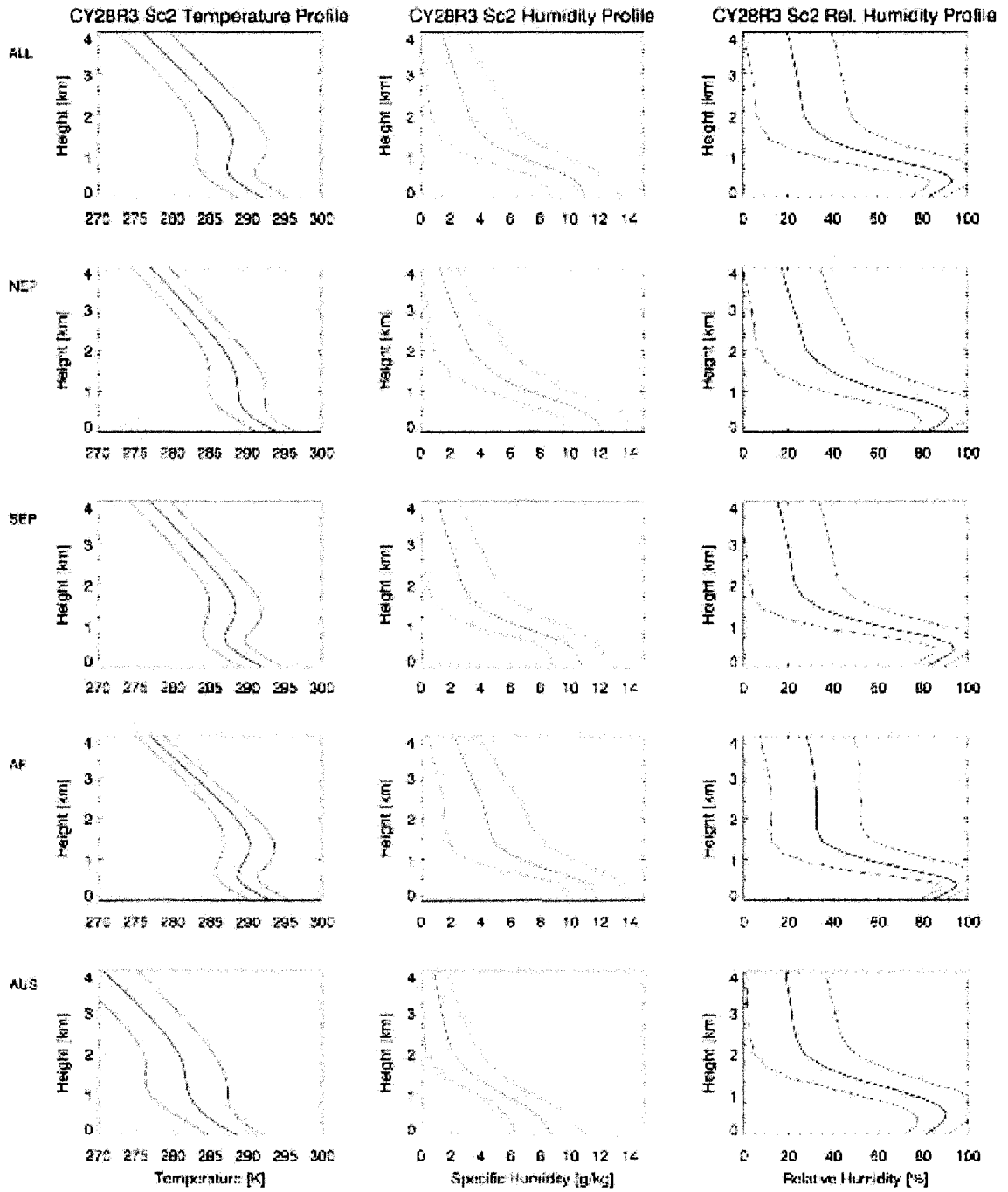

Fig. 5.48 Composite profiles of model temperature, specific and relative humidity for all CY28R3 model columns containing clouds classified as *Sc2* (thick lines). The thin lines indicate the plus/minus one standard deviation range. The rows show profiles for samples from all regions (first row) or individual regions (rows two through five).

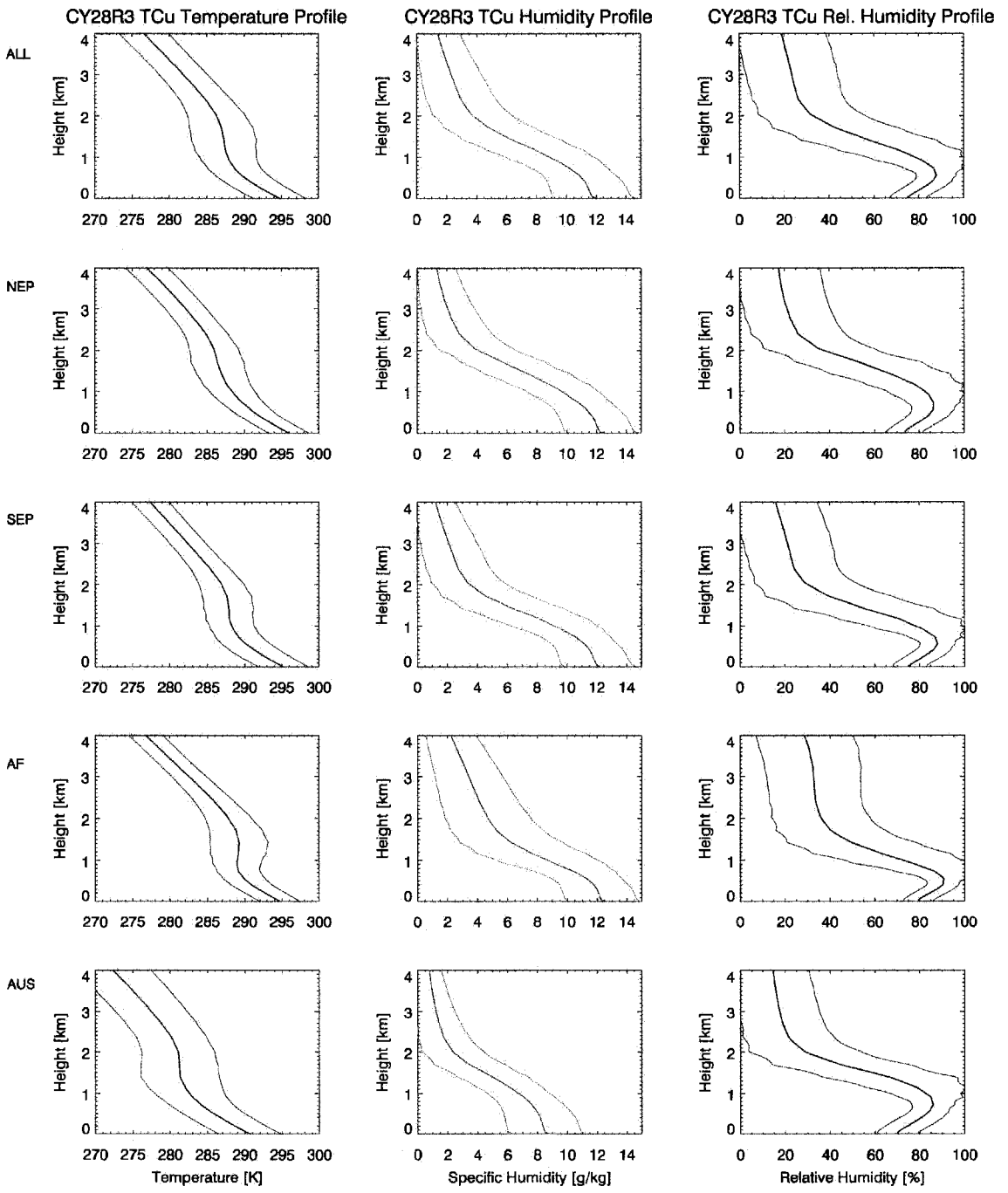

Fig. 5.49 Same as Fig. 5.48, but for CY28R3 samples classified as *TCu*.

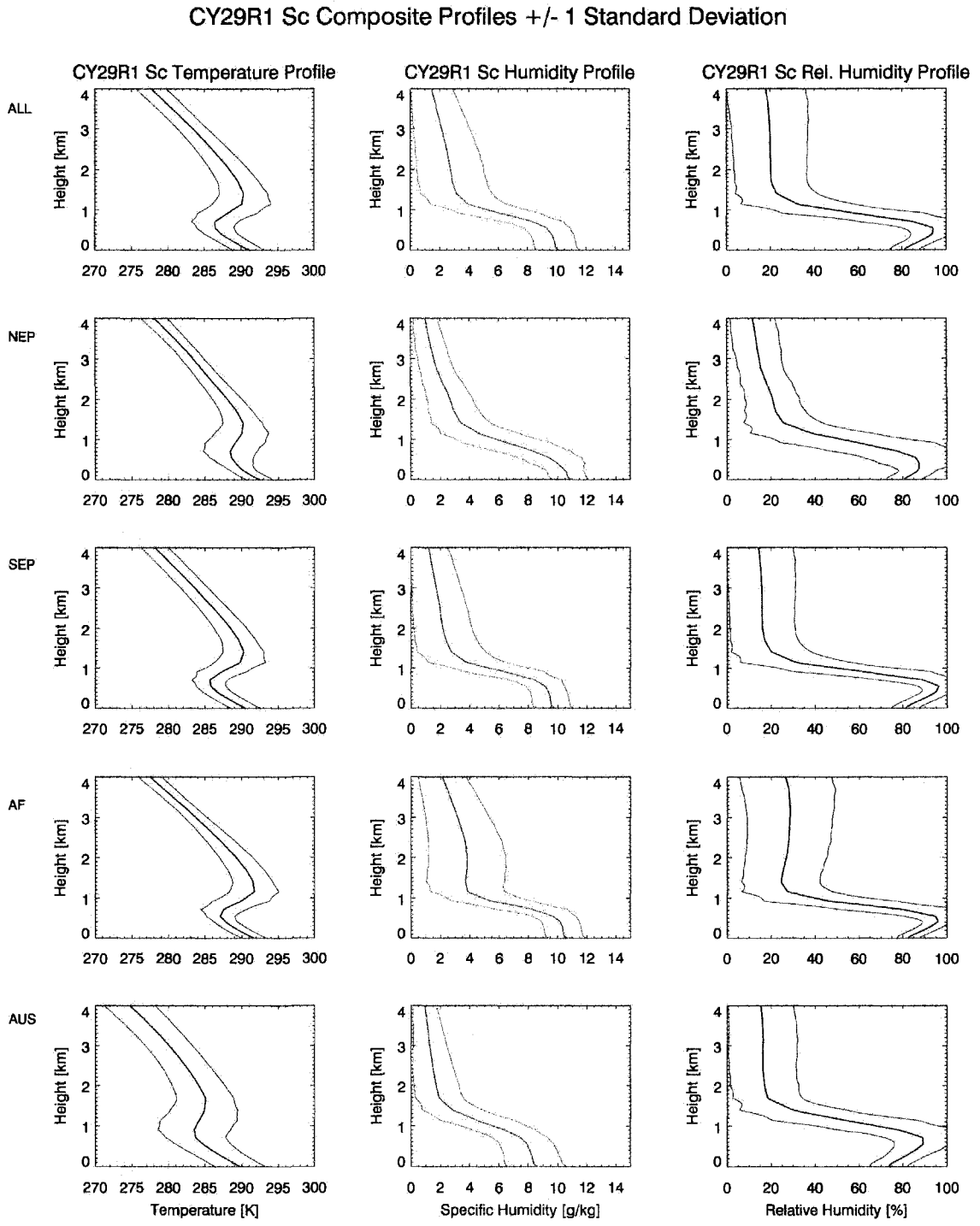

Fig. 5.50 Same as Fig. 5.48, but for CY29R1 samples classified as *Sc*.

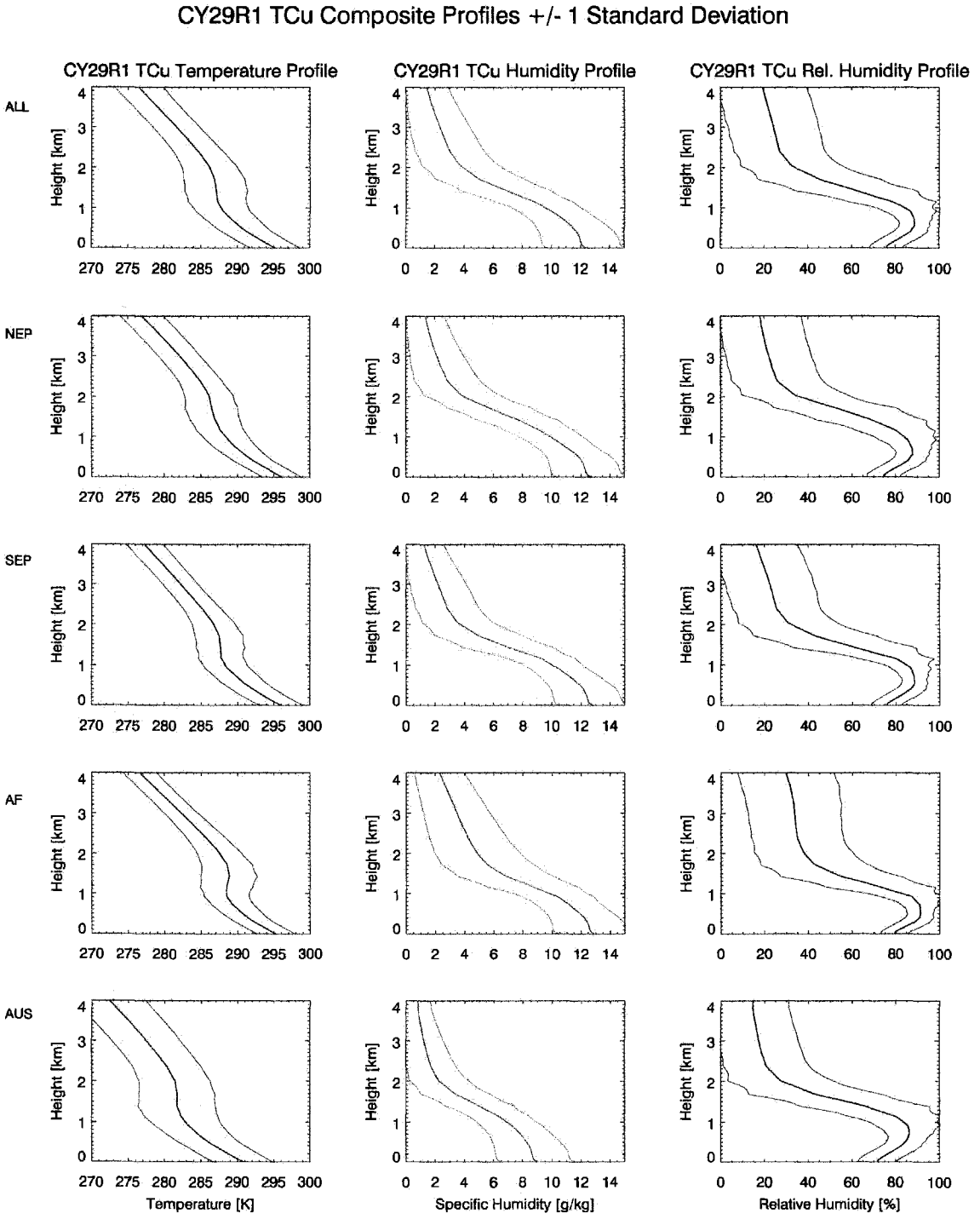

Fig. 5.51 Same as Fig. 5.48, but for CY29R1 samples classified as *TCu*.

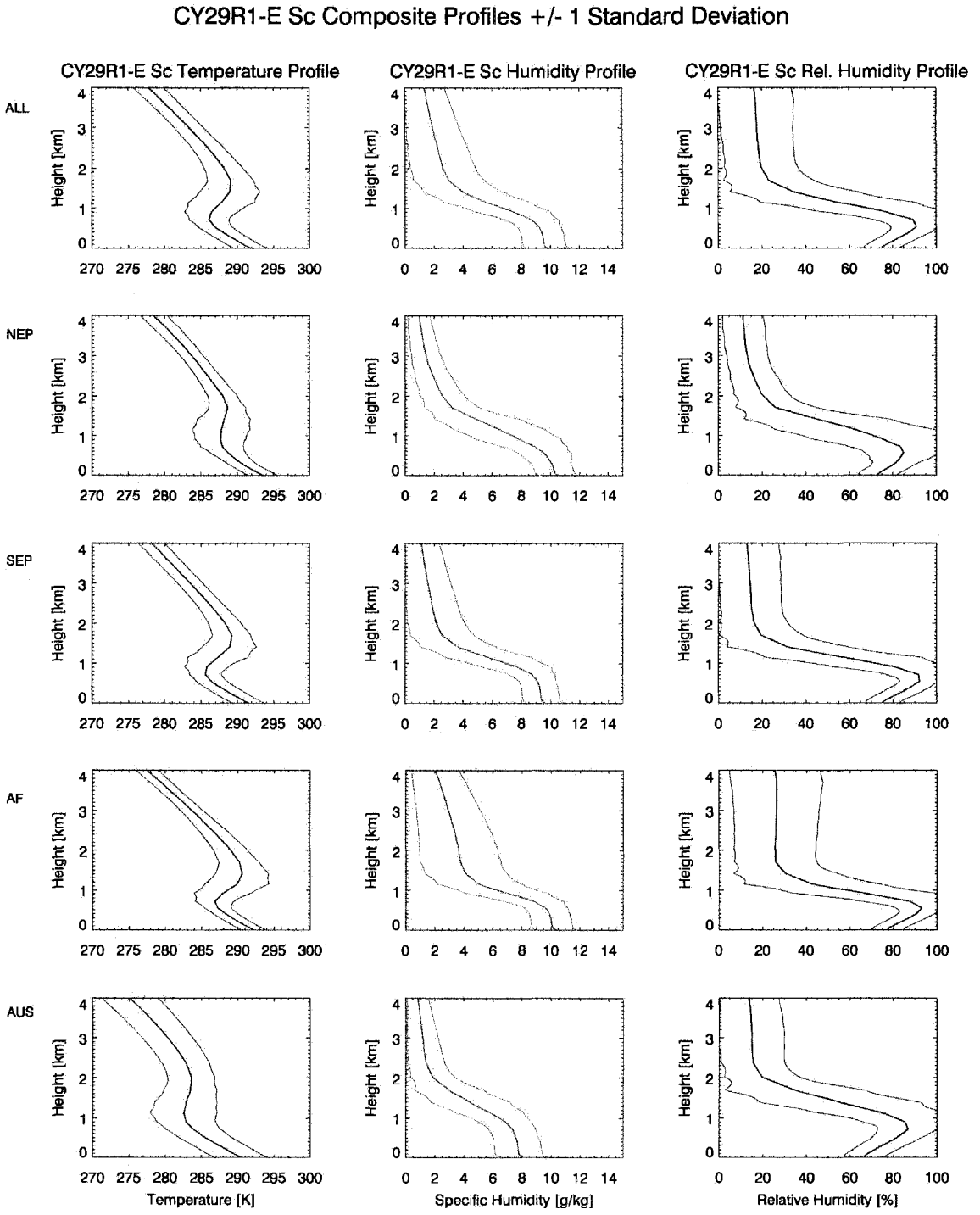

Fig. 5.52 Same as Fig. 5.48, but for CY29R1-E samples classified as *Sc*.

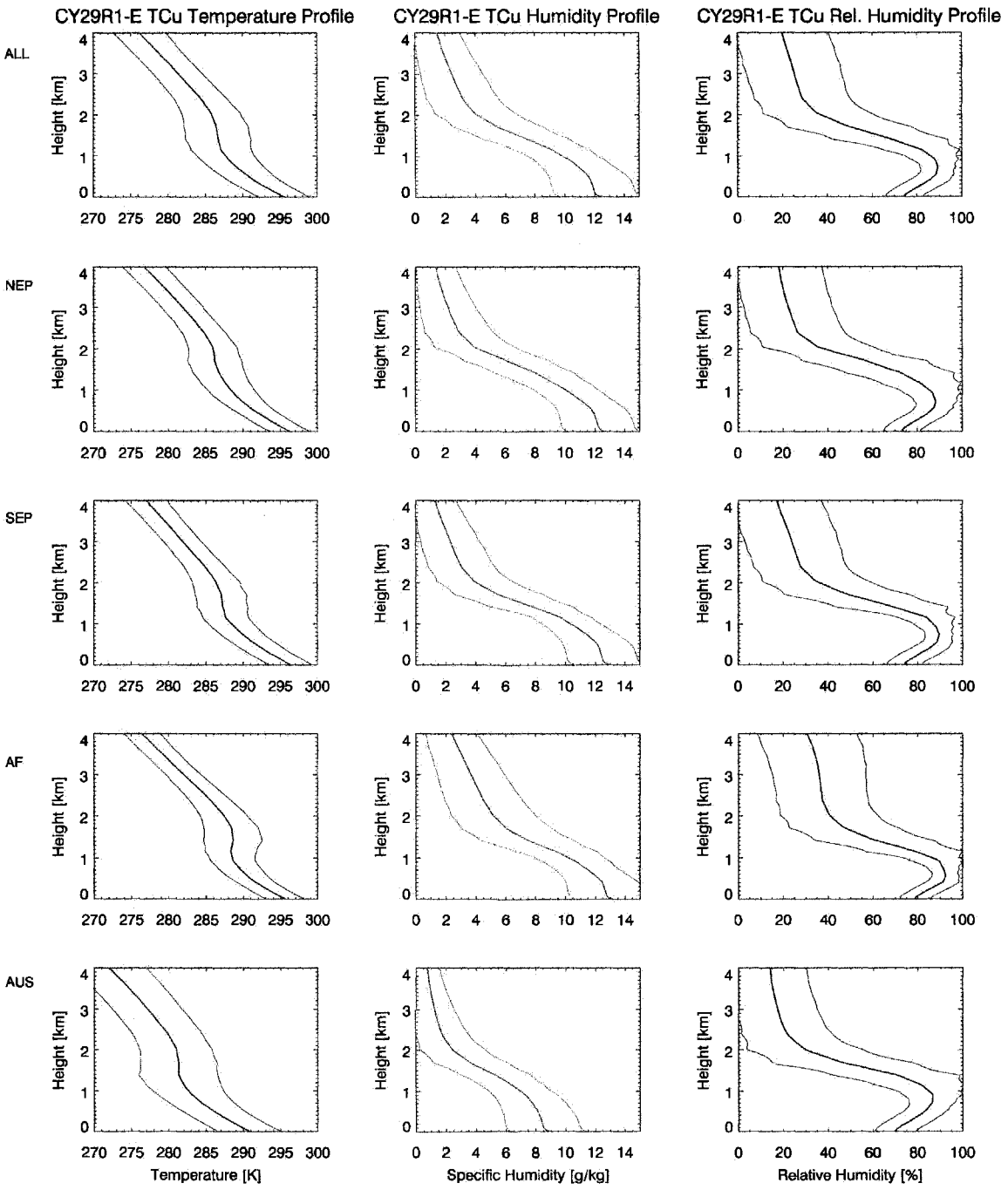

Fig. 5.53 Same as Fig. 5.48, but for CY29R1-E samples classified as *TCu*.

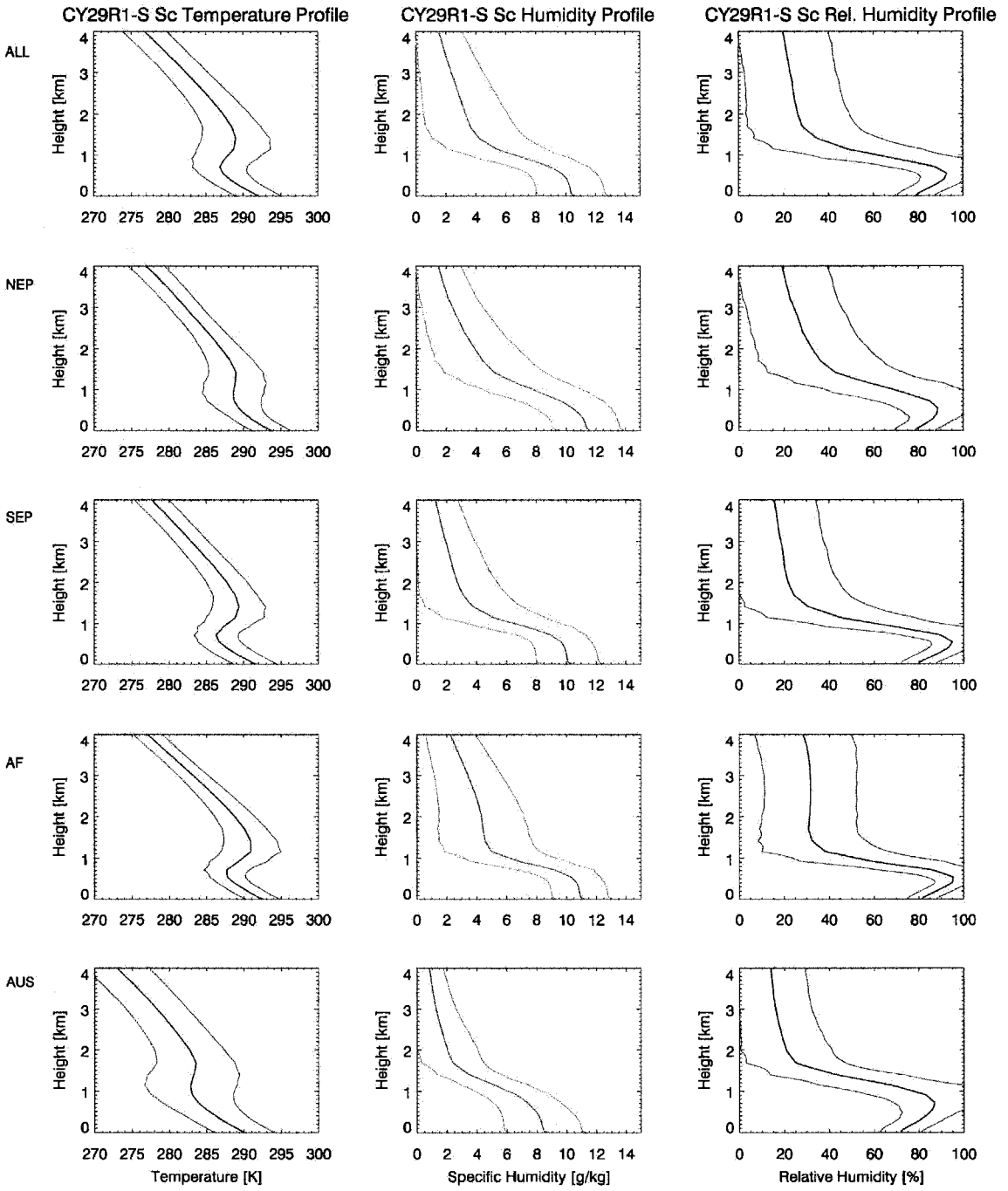

Fig. 5.54 Same as Fig. 5.48, but for CY29R1-S samples classified as *Sc*.

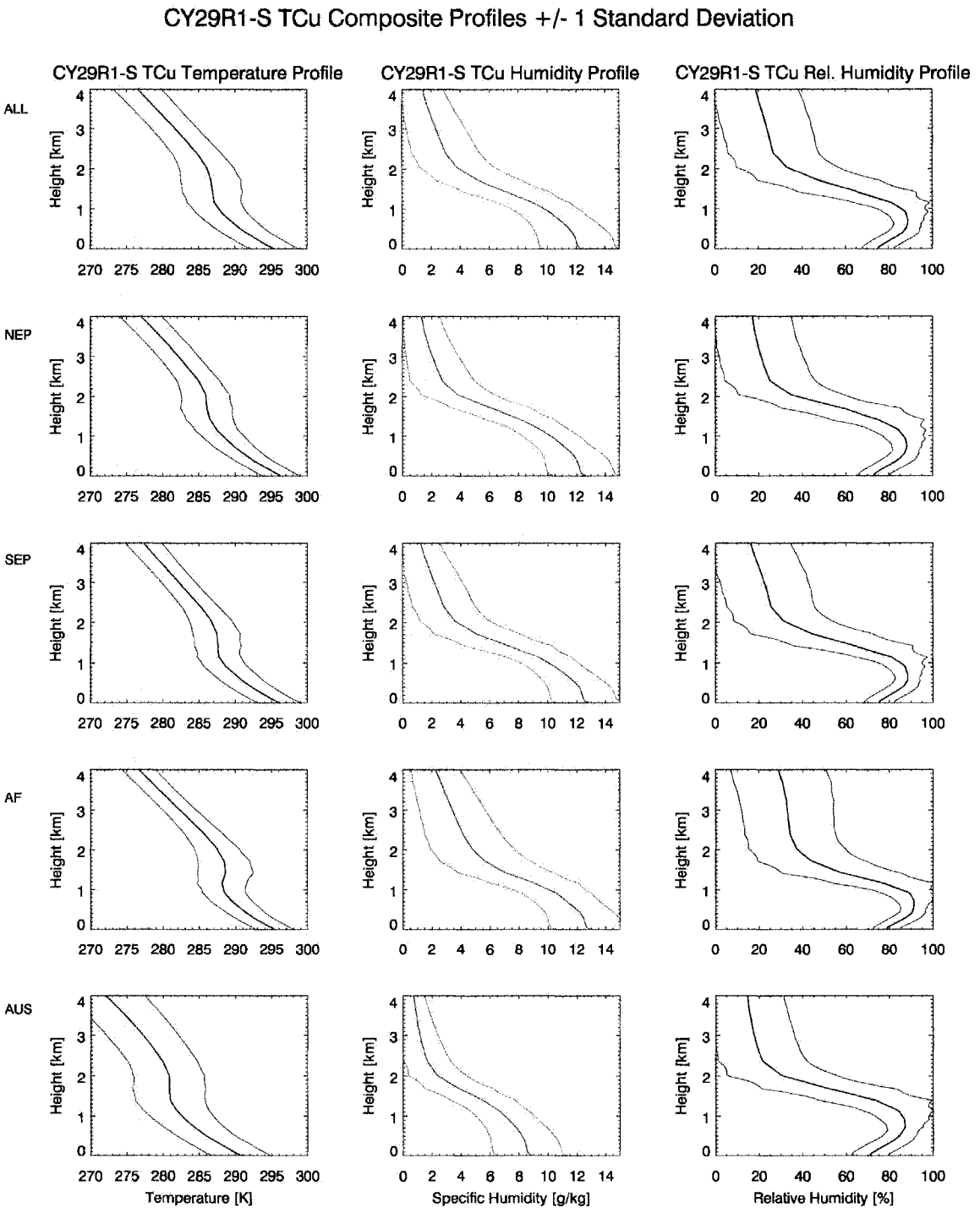

Fig. 5.55 Same as Fig. 5.48, but for CY29R1-S samples classified as *TCu*.

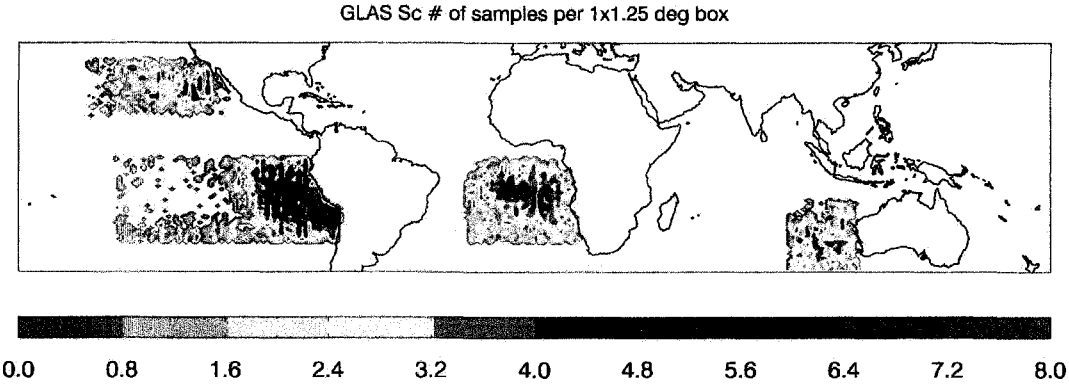

Fig. 5.56 Number of GLAS samples per 1°x1.25° grid box classified as *Sc*.

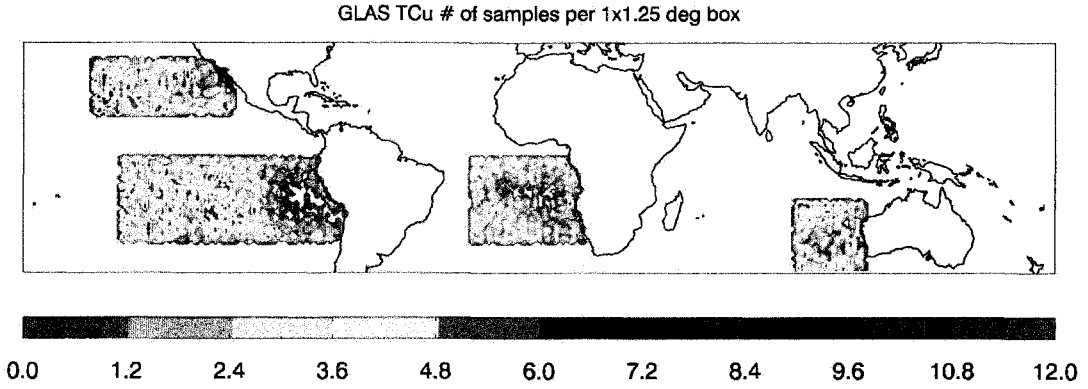

Fig. 5.57 Number of GLAS samples per 1°x1.25° grid box classified as *TCu*.

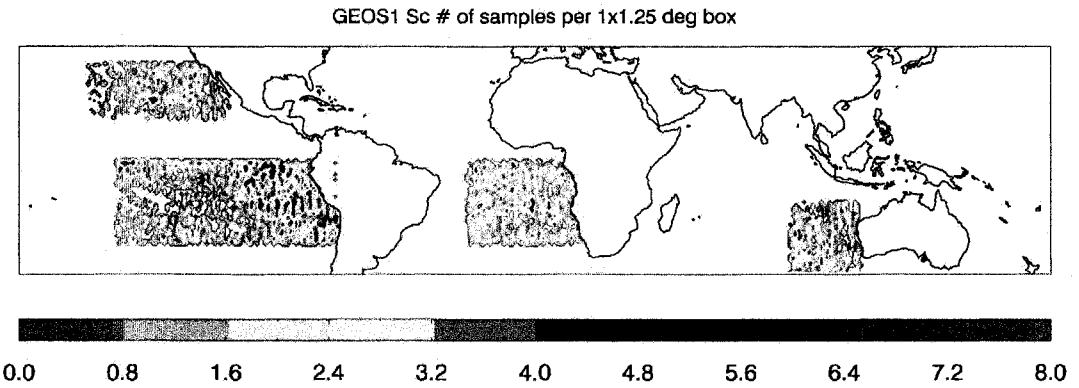

Fig. 5.58 Number of GEOS1 samples per 1°x1.25° grid box classified as *Sc*.

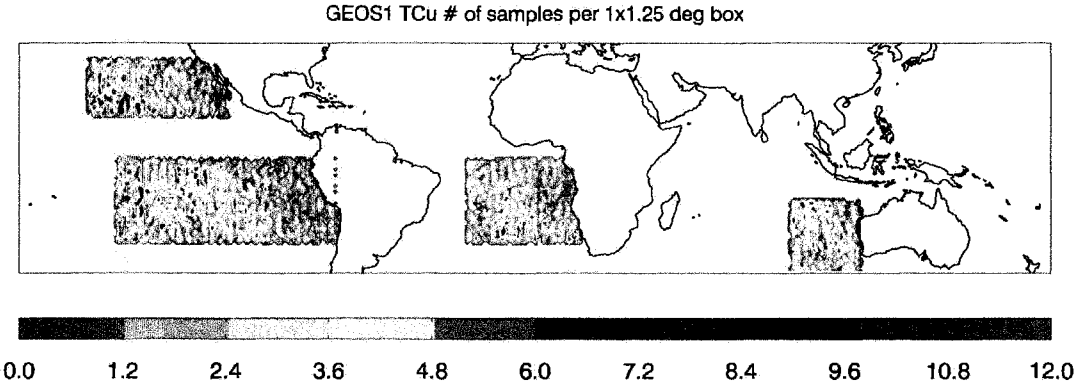

Fig. 5.59 Number of GEOS1 samples per 1°x1.25° grid box classified as *TCu*.

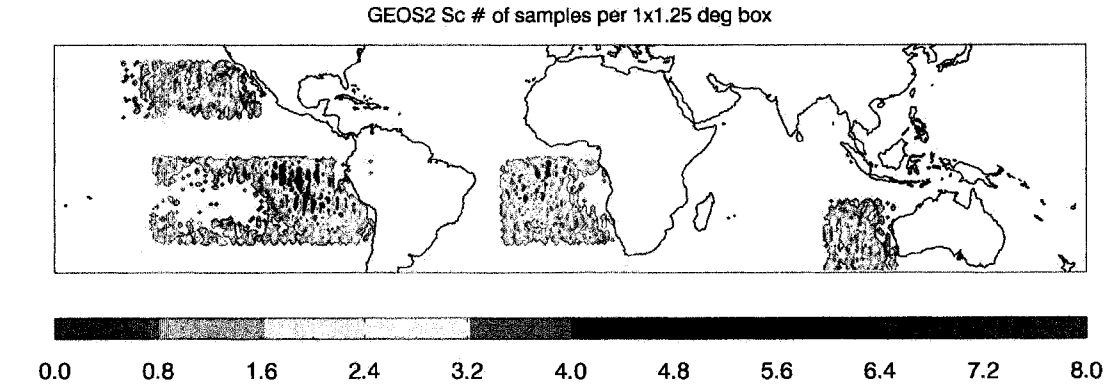

Fig. 5.60 Number of GEOS2 samples per 1°x1.25° grid box classified as *Sc*.

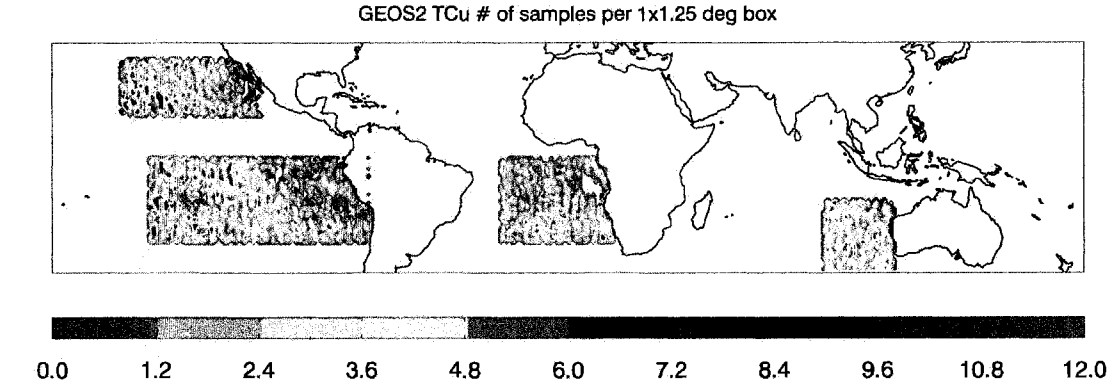

Fig. 5.61 Number of GEOS2 samples per 1°x1.25° grid box classified as *TCu*.

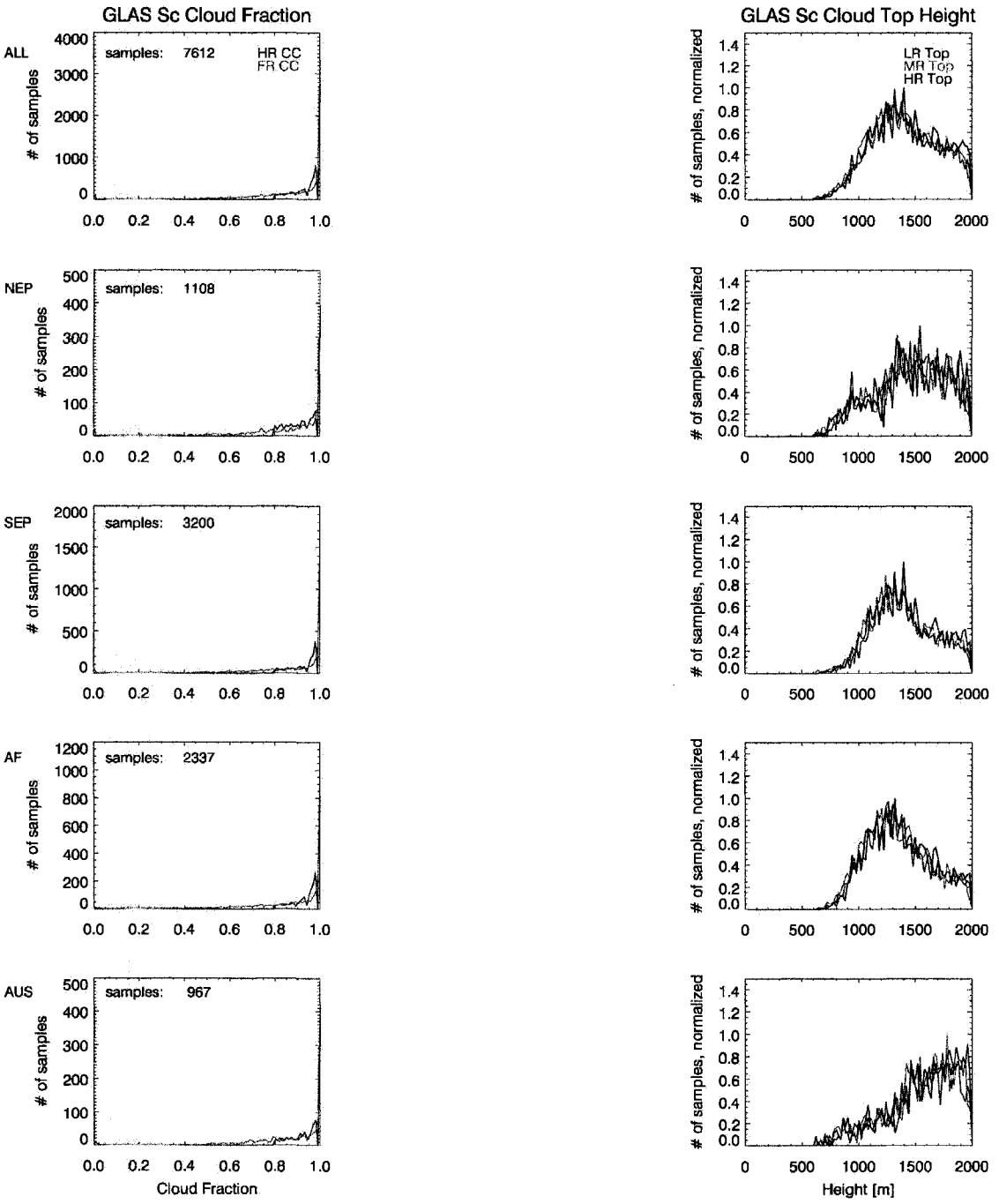

Fig. 5.62 Same as Fig. 5.35, but for GLAS samples on the GEOS-5 grid.

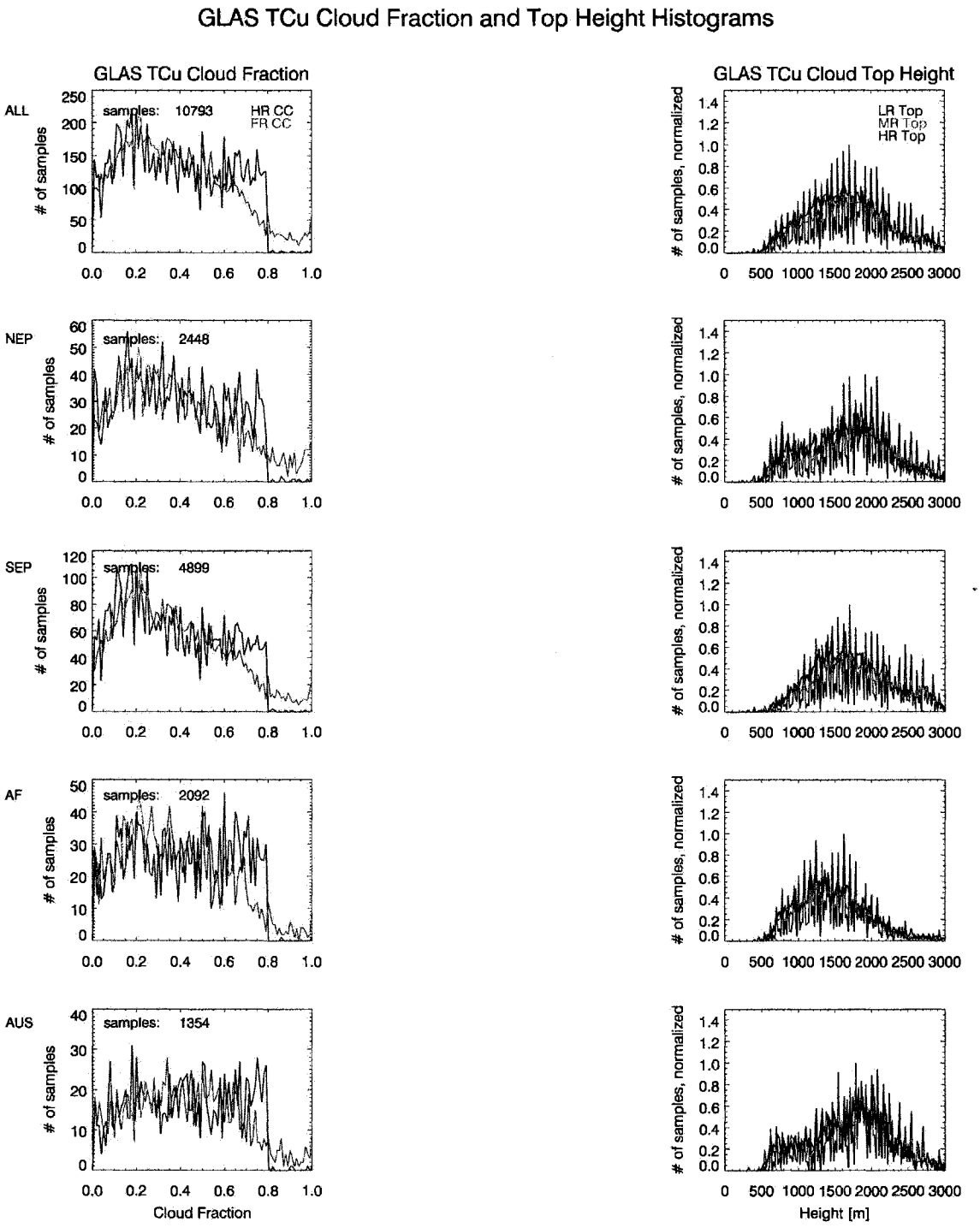

Fig. 5.63 Same as Fig. 5.35, but for GLAS samples on the GEOS-5 grid classified as *TCu*.

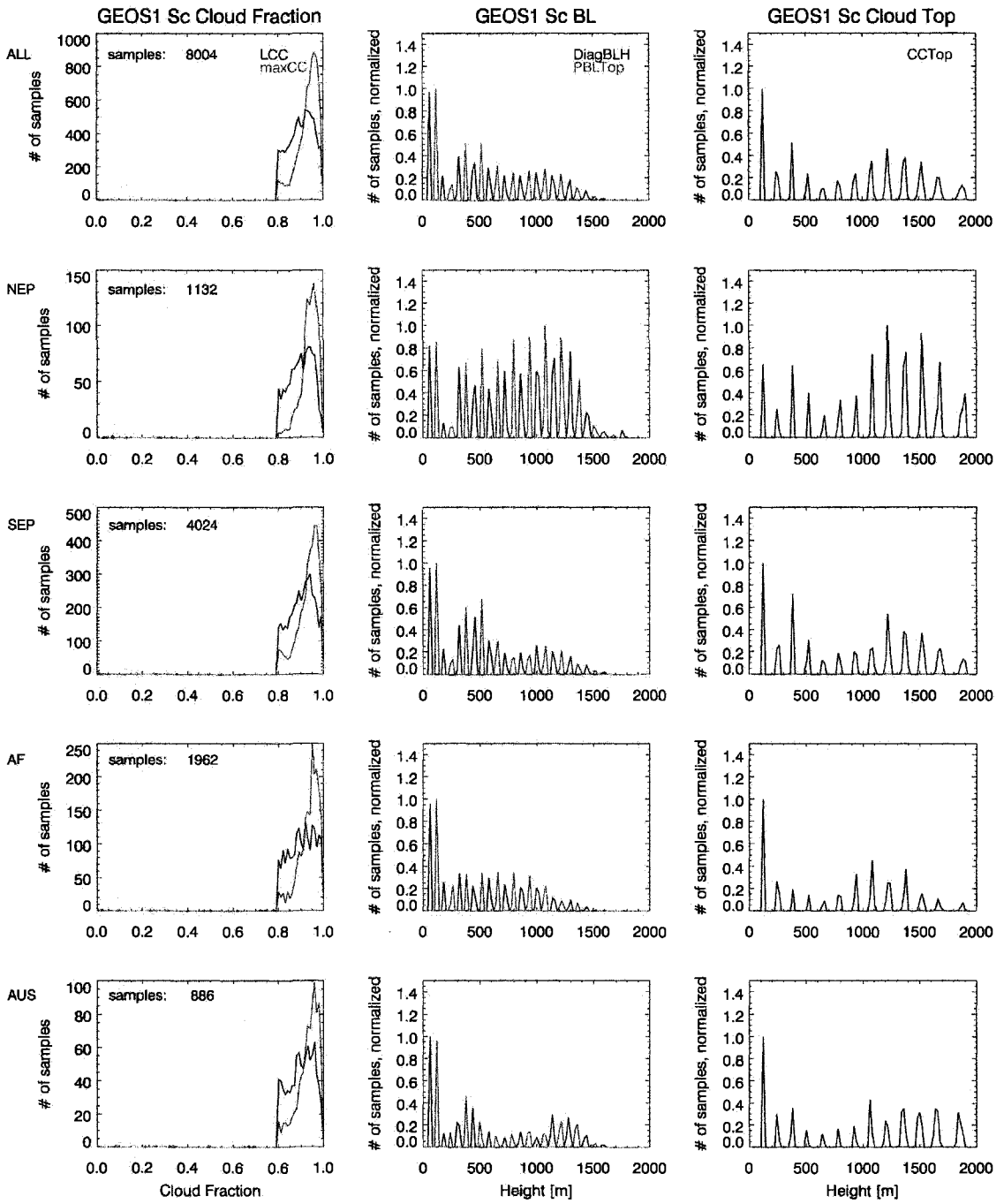

Fig. 5.64 Histogram of cloud fraction, cloud base height and cloud top height for all GEOS1 samples classified as *Sc*. The number of samples classified as *Sc* in all four regions is printed in the upper left corner of the left panels. The variable abbreviations used in the labels are explained in sections 5.2.1 and 5.3.1.

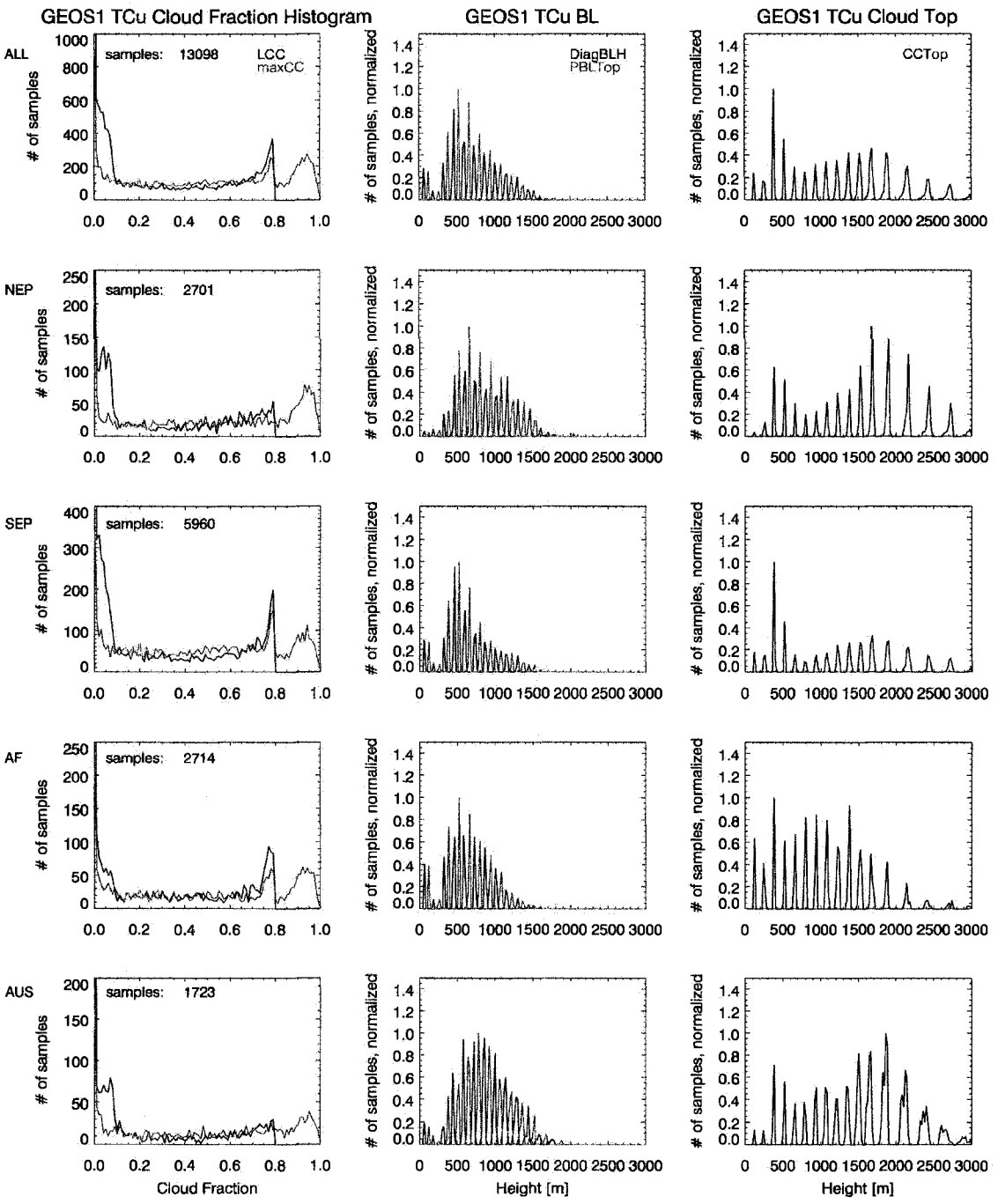

Fig. 5.65 Same as Fig. 5.64, but for GEOS1 samples classified as *TCu*.

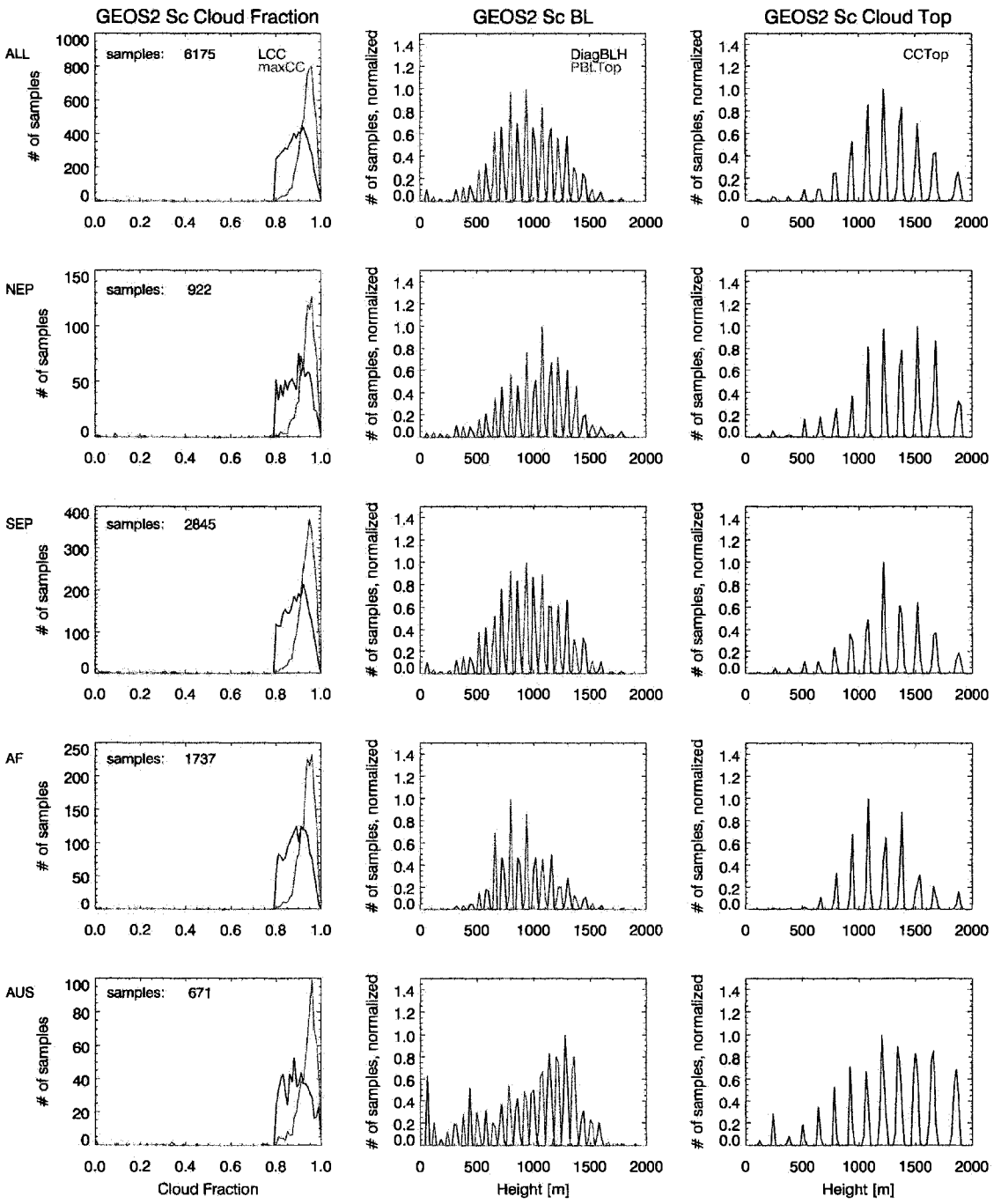

Fig. 5.66 Same as Fig. 5.64, but for GEOS2 samples classified as *Sc*.

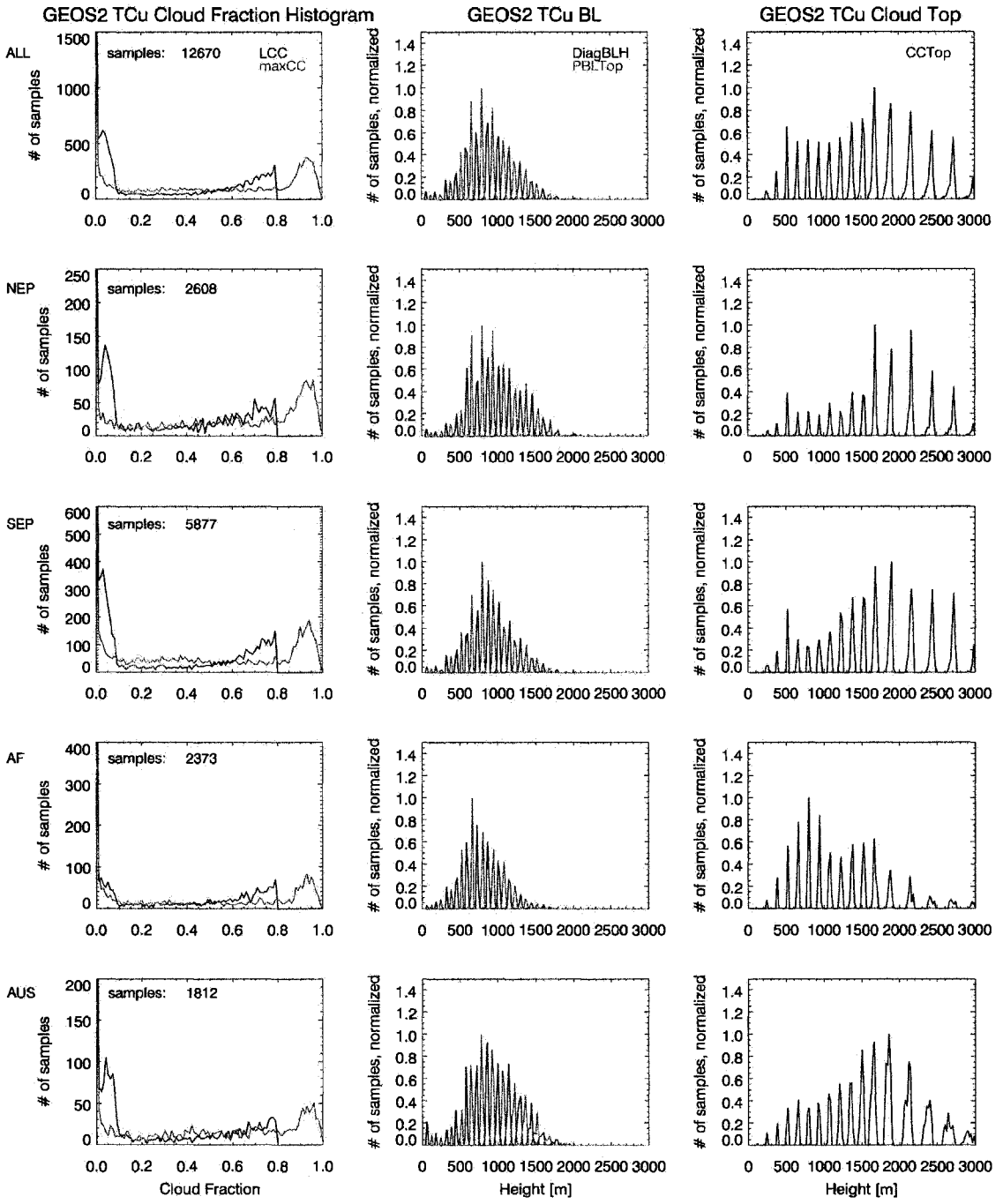

Fig. 5.67 Same as Fig. 5.64, but for GEOS2 samples classified as *TCu*.

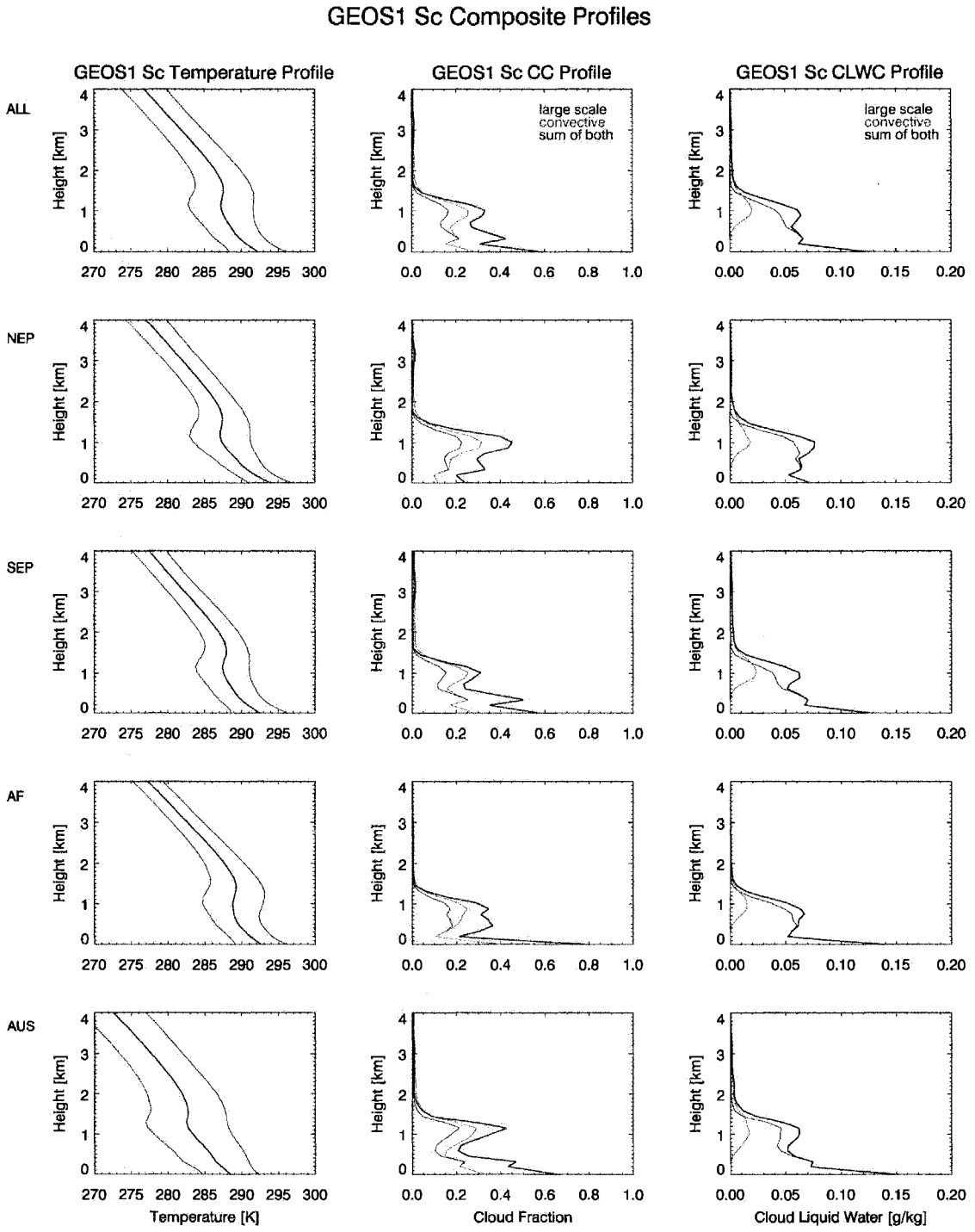

Fig. 5.68 Composite profiles of temperature, cloud fraction and cloud liquid water content for all GEOS1 samples classified as *Sc*. In the left panel, the thick line is the average, and the plus/minus one standard deviation range is marked by the thin lines. In the middle and right panel, the contributions to the total (green) from the convective cores (red) and the large scale moisture scheme (blue) are shown separately.

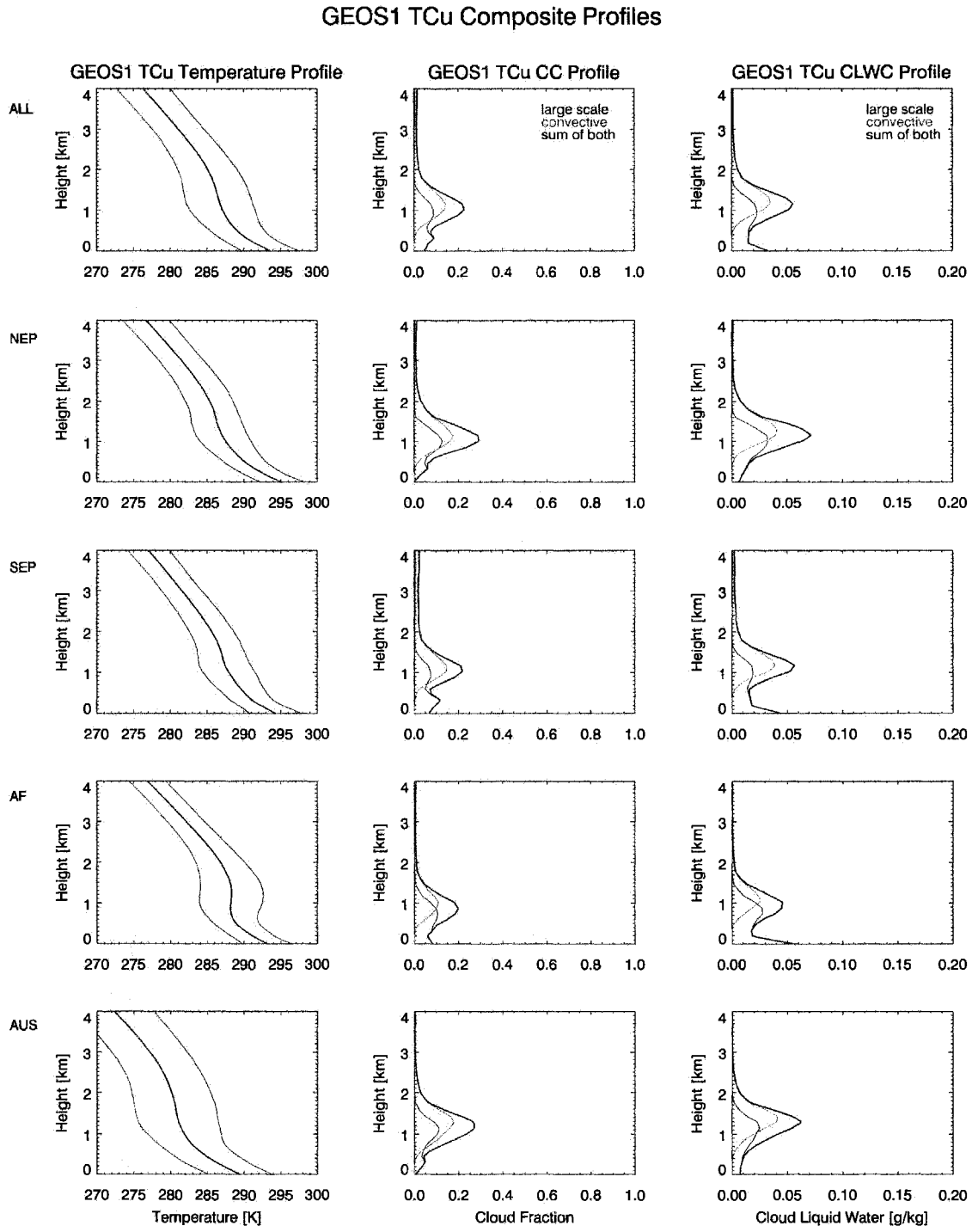

Fig. 5.69 Same as Fig. 5.68, but for GEOS1 samples classified as *TCu*.

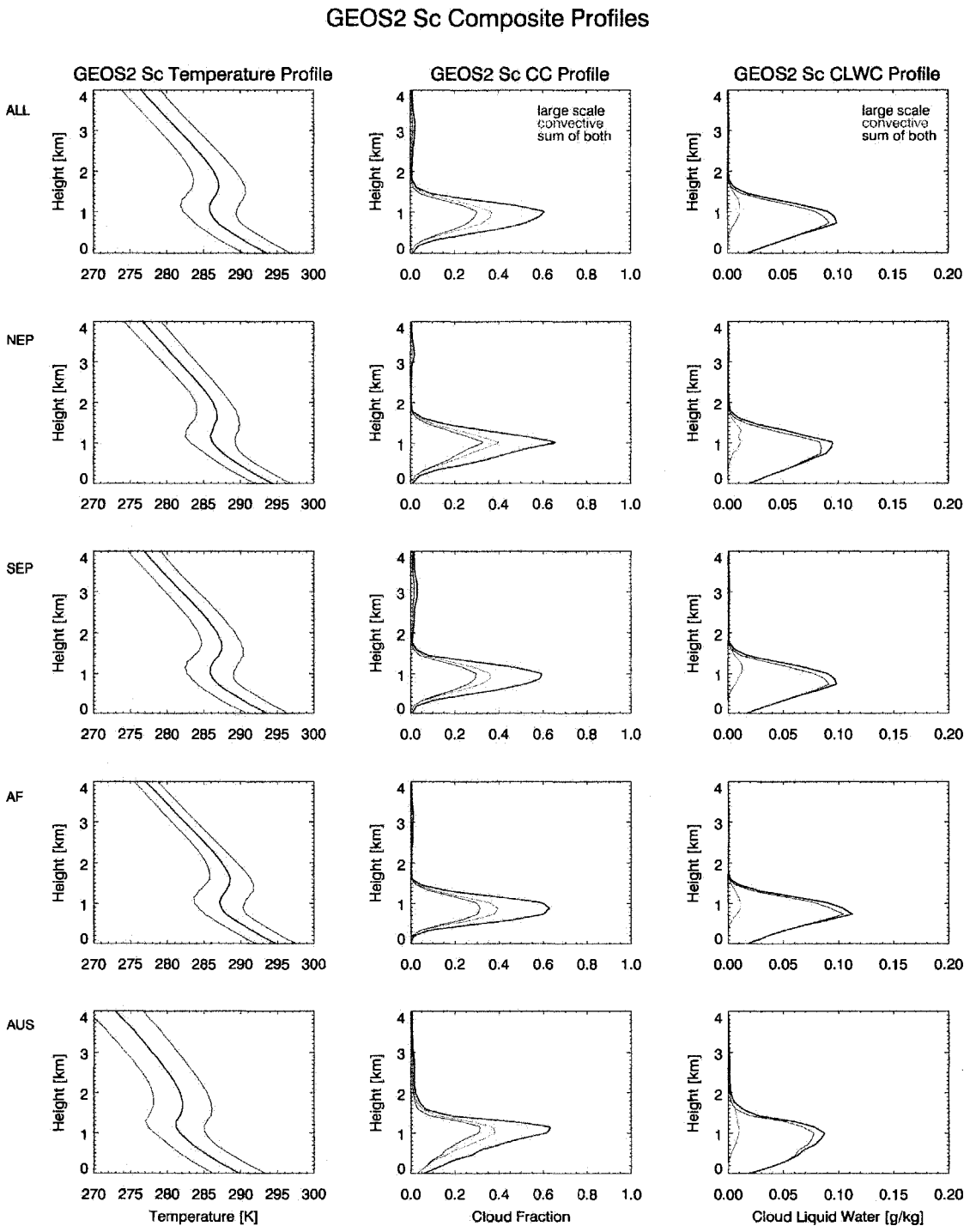

Fig. 5.70 Same as Fig. 5.68, but for GEOS2 samples classified as *Sc*.

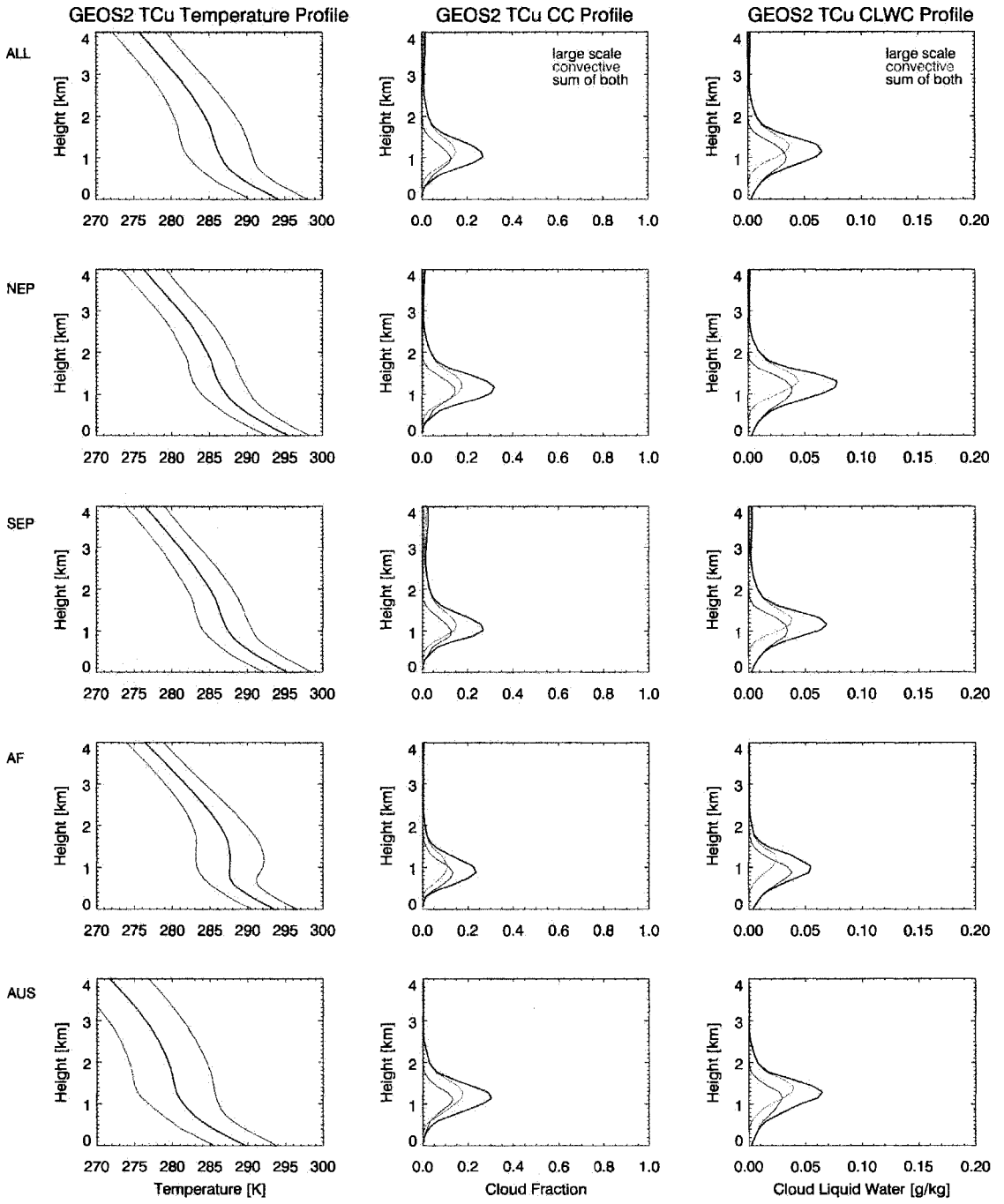

Fig. 5.71 Same as Fig. 5.68, but for GEOS2 samples classified as *TCu*.Fig. 5.71 Same as Fig. 5.68, but for GEOS2 samples classified as TCu.

Chapter 6: Additional observations

6.1. Low clouds observed by CALIPSO - the seasonal cycle

CALIPSO data are now available, spanning a period of over a year. To investigate seasonal changes in the low cloud-top height, observations from July 2006, October 2006, January 2007 and April 2007 have been averaged for each of the four months (Fig. 6.1). In these maps, the lowest detected cloud-top height, if not exceeding 3 km, of the 5 km resolution cloud layer product has been averaged into 2°x2° latitude-longitude bins. Both daytime and nighttime observations are included. The number of observed low cloud tops per bin is plotted in Fig. 6.2. Areas with ≤70 averaged cloud tops per bin are hatched in Fig. 6.1. The number 70 is a somewhat arbitrary threshold corresponding to roughly a quarter of the maximum number of samples found in any bin on the map. The number of samples may be low in a grid box for several reasons: the number of overpasses over the particular area was low, no low clouds existed, or the low clouds were obscured by higher clouds. Whatever the reason, the average cloud-top height in areas with low sample numbers is less reliable than in areas with high sampling numbers.

In addition to the maps, the low cloud tops were also averaged into four bands shown in Fig. 6.3. The bands labeled "Neiburger" and "SEP" (South East Pacific) follow the gradient of cloud-top heights from the North and South American coasts into the central Pacific ocean. The bands titled "near" and "far" run parallel to the American coast, the

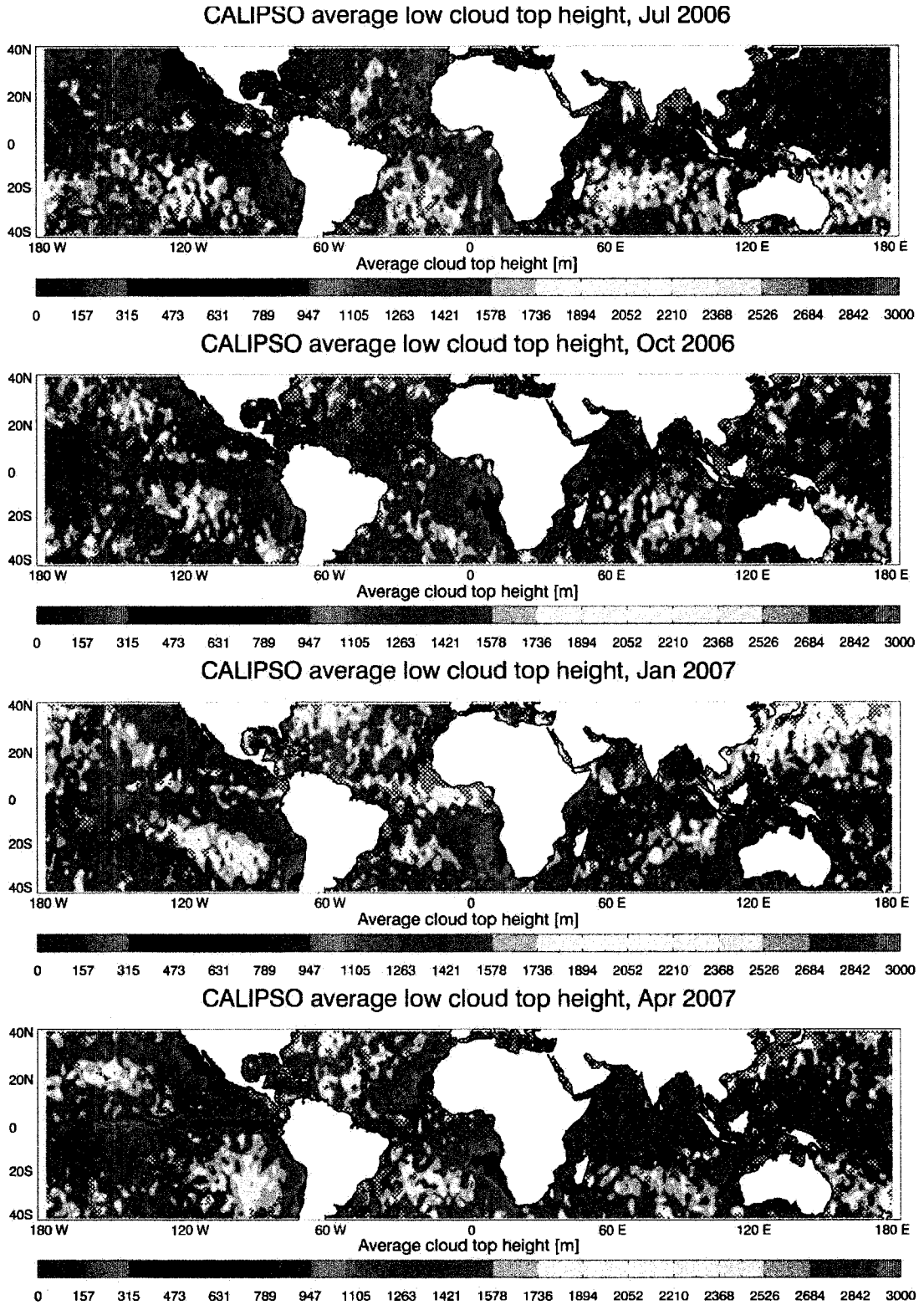

Fig. 6.1 Lowest detected CALIPSO cloud top, if not exceeding 3 km, averaged into 2°x2° bins for the months of July 2006, October 2006, January 2007 and April 2007. Cross hatching indicates areas with ≤70 averaged samples.

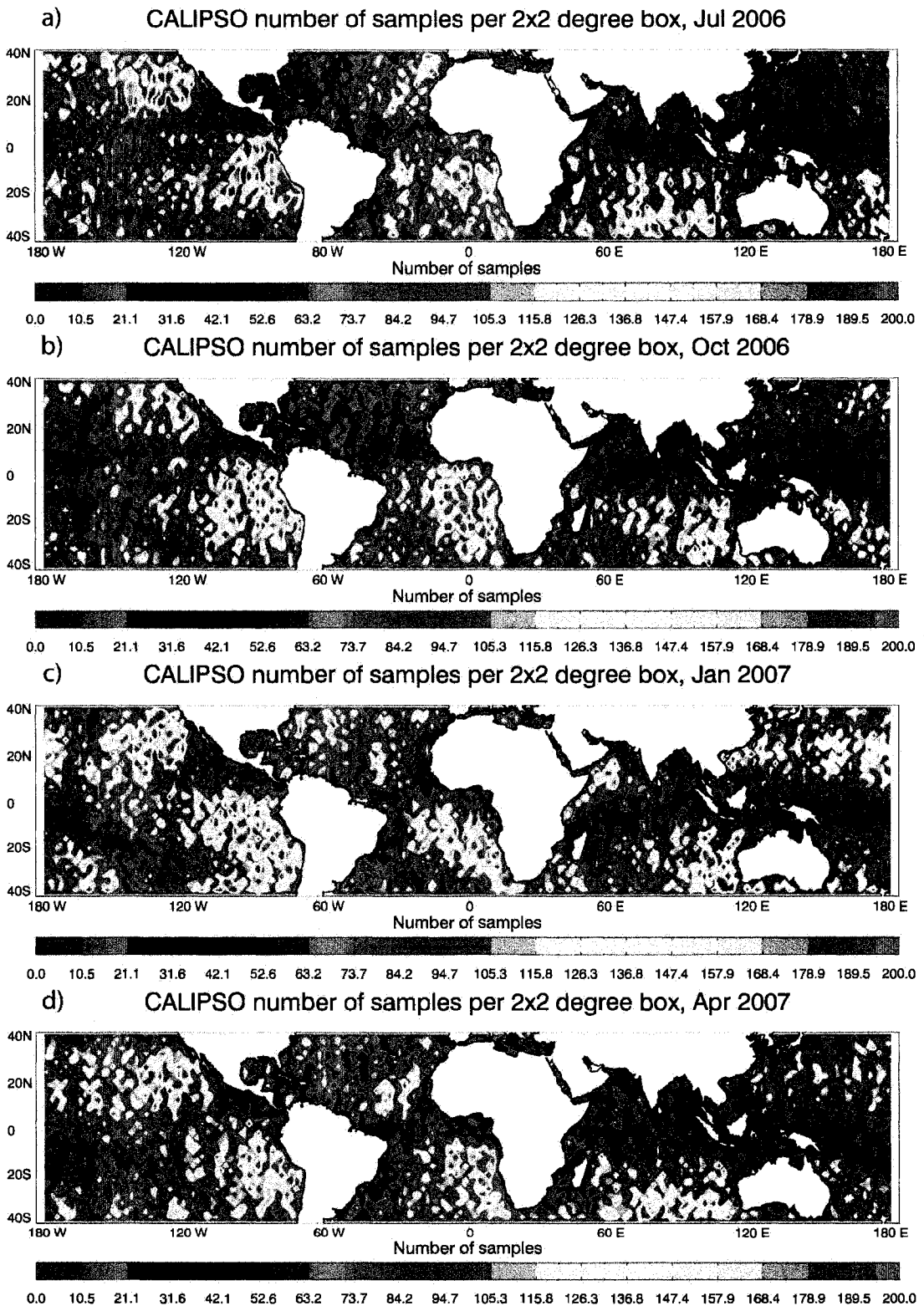

Fig. 6.2 Number of averaged CALIPSO low cloud tops per 2°x2° bin, corresponding to the previous figure, for the months of July 2006, October 2006, January 2007 and April 2007.

"near" band directly along the coast line, the "far" band approximately 25° west of the coast. These bands allow a comparison of cloud-top heights in the North and South Pacific for similar cloud regimes.

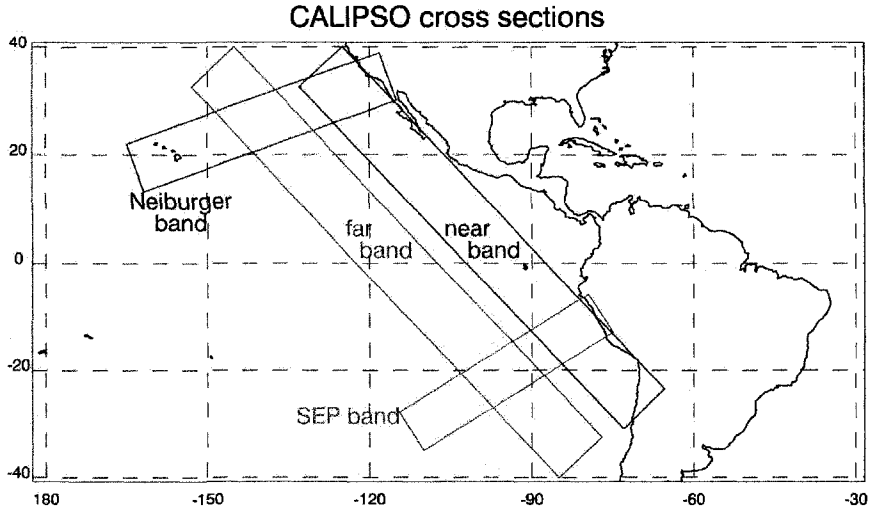

Fig. 6.3 Location of bands.

In Fig. 6.5 through Fig. 6.8, individual observed cloud tops are shown as green dots. The average cloud-top height for each of the four months is shown as a solid thick line, while the one-standard-deviation range is marked by thin black lines. To obtain the average cloud-top height along each band, cloud tops are averaged into sections perpendicular to the length of the band (see Fig. 6.4). The average cloud-top height is plotted against the center longitude (Neiburger, SEP bands) or center latitude (near and far bands) of each bin.

Overview

A look at the maps (Fig. 6.1) shows that during July, average cloud tops are higher in the southern hemisphere than in the northern hemisphere. The cross hatching, as well as Fig. 6.2a, show that fewer low cloud tops are found in the northern hemisphere. It is likely that more frequent deep convection exists in place of low clouds, or covers up

some of the low cloudiness. In October, the areas with low sample numbers (and likely deep convection) shift south, and the average low cloud-top height starts to increase in the northern hemisphere. In January, deeper cloud-top heights appear particularly in the west Pacific and the Atlantic. In April, the cloud-top heights are similar in both hemispheres, and the regions with low sampling start to spread north again. The seasonal variations are particularly pronounced in the north east Pacific.

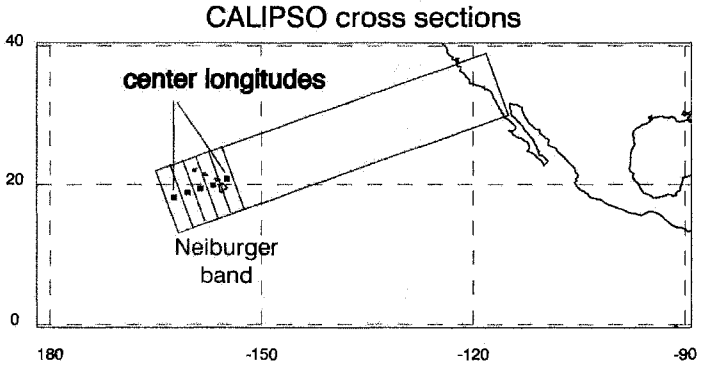

Fig. 6.4 Schematic of bins along the Neiburger band.

6.1.1. North East Pacific

Focussing on the north east Pacific (Neiburger band), seasonal variations are clearly evident in Fig. 6.5. The lowest average cloud tops along the North American coast can be found during July, with values around 600 m. The variability in the eastern half of the band is lowest as well, as indicated by a small standard deviation. The gradient in cloud-top height from the coast (~120°W) to Hawaii (Big Island at 155°W) is relatively constant, with increasing cloud-top height and variability towards the west. In October, the highest cloud tops are located between 140° and 150° W, decreasing weakly towards the west, and more strongly to wards the coast. The near-coastal average cloud-top height is located around 1 km, and the variability of individual cloud top measurements

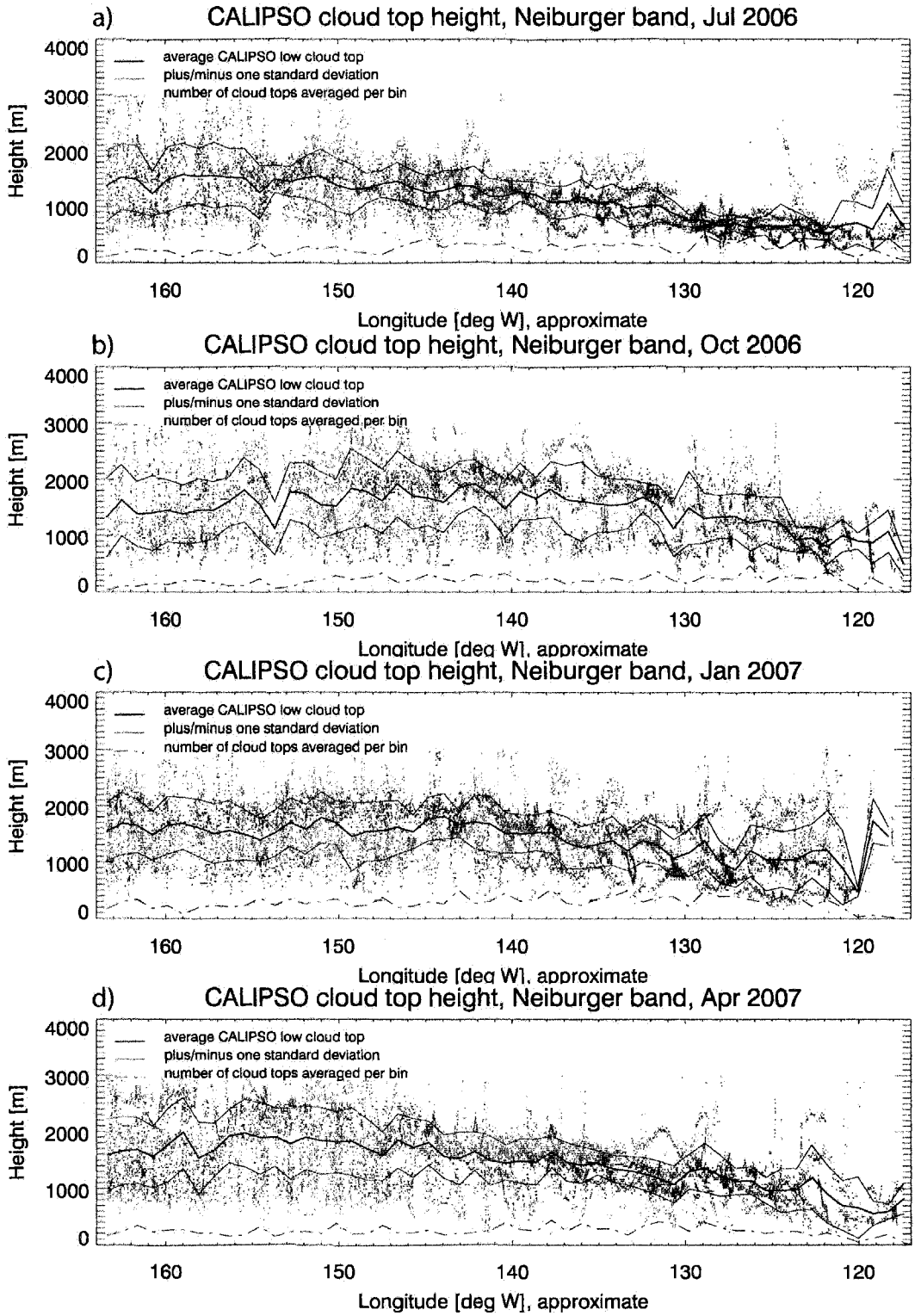

Fig. 6.5 Lowest detected CALIPSO cloud tops, if not exceeding 3 km, along the Neiburger band. Individual cloud tops marked by green dots. Average cloud-top height along the band plus/minus one standard deviation plotted as solid thick (thin) line. Number of averaged cloud tops per bin plotted as dot-dashed line.

is overall greater than in July. January has similar near-coastal values and overall variability as October. The cloud-top height gradient is concentrated in the eastern half of the band. In April, the cloud-top height is reduced to 700 m, and variability is decreasing. The cloud-top height gradient from coast to Hawaii is near constant across the band again. The gradient in low cloud-top height from the North American coast to Hawaii has been observed many times, starting with Neiburger (1961).

Overall, the seasonal variations are greatest between the coast and about 140°W. Both average cloud-top heights and variability of individual samples change little in the western half of the band.

6.1.2. South East Pacific

In the south east Pacific, the seasonal cycle seems less pronounced than in the north. This area is well sampled in all seasons, and the one-standard-deviation range is comparatively small in all months (Fig. 6.6). Both average cloud-top height and variability show little seasonal change west of 100°W. Near the coast (located at ~79°W), the average cloud-top height is lowest in July and October with values around 1 km. The cloud-top height increases gradually from the coast to approximately 100°W. In January, and especially in April, the cloud-top height rises in the eastern half of the band by roughly 400 m (900 m), while values at the coast remain low. This leads to a very steep gradient concentrated within about 3° of the coast line.

6.1.3. Stratocumulus regime

The near band captures the stratocumulus regime along the north and south American coasts, as well as the ITCZ around the Equator. In the northern hemispheric

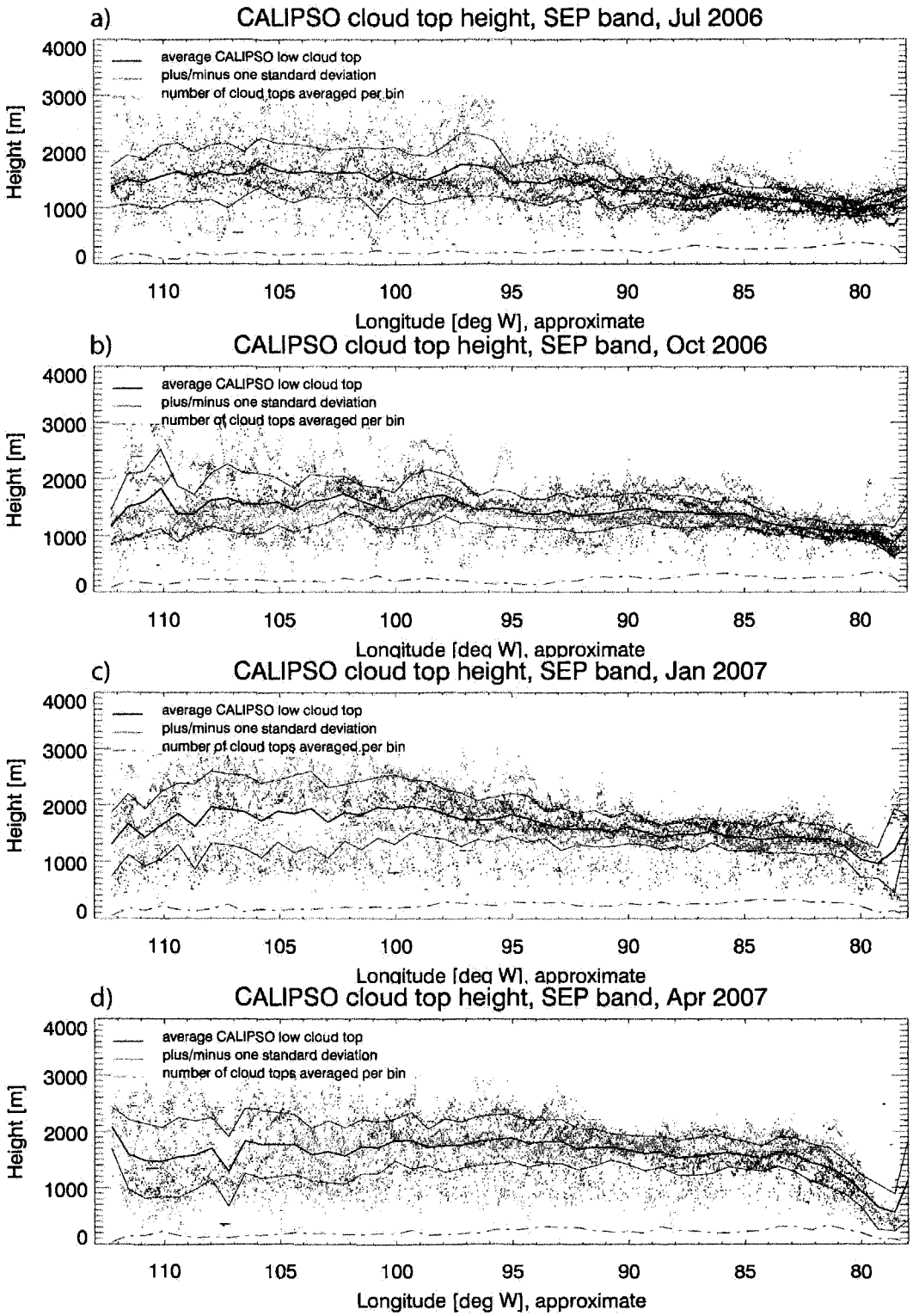

Fig. 6.6 Lowest detected CALIPSO cloud tops, if not exceeding 3 km, along the South East Pacific (SEP) band. Individual cloud tops marked by green dots. Average cloud-top height along the band plus/minus one standard deviation plotted as solid thick (thin) line. Number of averaged cloud tops per bin plotted as dot-dashed line.

summer, the region of deep convection extends from Panama all the way to California along the coast. This corresponds to the lower sample numbers from around 5°N to 22°N in July and October. This stretch of the near band is also characterized by a greater average cloud-top height, and large standard deviation. While the region with low sampling remains almost unchanged, the area of high variability and higher average cloud tops moves south in January, between approximately 5°S and 15°N. In April a curious phenomenon occurs: between 1°S and 5°N, the average cloud-top height is quite low, while on both sides, the cloud-top height remains high. This seems to indicate an area with suppressed convection, where low clouds frequently appear.

Poleward of the deep convective part of the band, the average cloud-top height is generally lower, and observations are less variable. As already described in section 6.1.1, the lowest and least variable cloud tops in the north east Pacific occur in July. October and January are more variable with higher average tops, and in April, a return to July conditions can be observed. In the south east Pacific, the average cloud-top height is less variable throughout the year (see section 6.1.2). Most notable is that the consistent low cloudiness extends furthest north in July and October, and retreats to approximately 10°S (15°S) in January (April). It should be mentioned that south of ~22°S, the band is no longer parallel to the South American coast line, but approaches the coast.

In April and July, the low clouds in the southern part of the band are deeper than in the northern part. In October and January, the two regions have clouds with comparable average cloud-top heights.

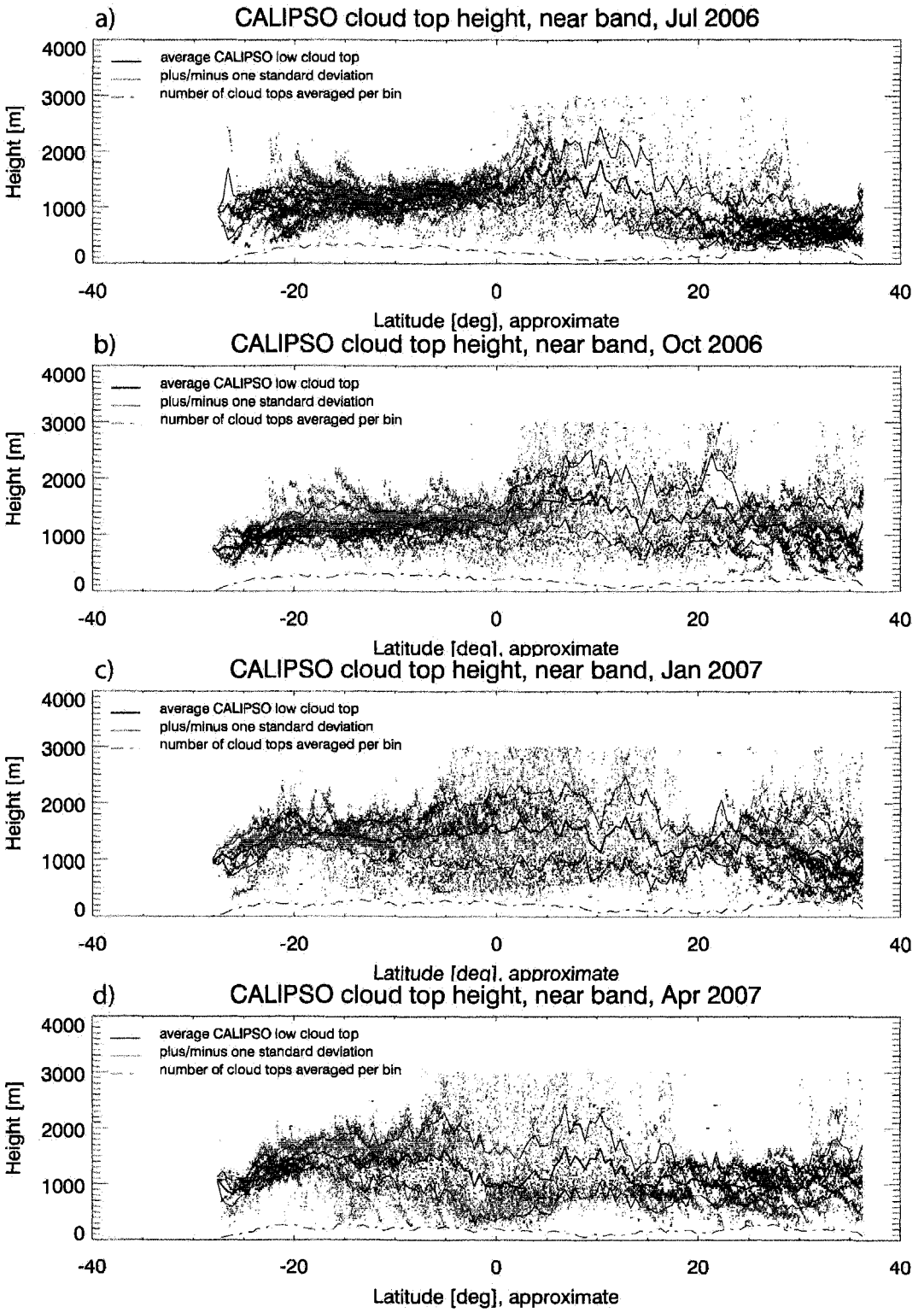

Fig. 6.7 Lowest detected CALIPSO cloud tops, if not exceeding 3 km, along the American coast (near band). Individual cloud tops marked by green dots. Average cloud-top height along the band plus/minus one standard deviation plotted as solid thick (thin) line. Number of averaged cloud tops per bin plotted as dot-dashed line.

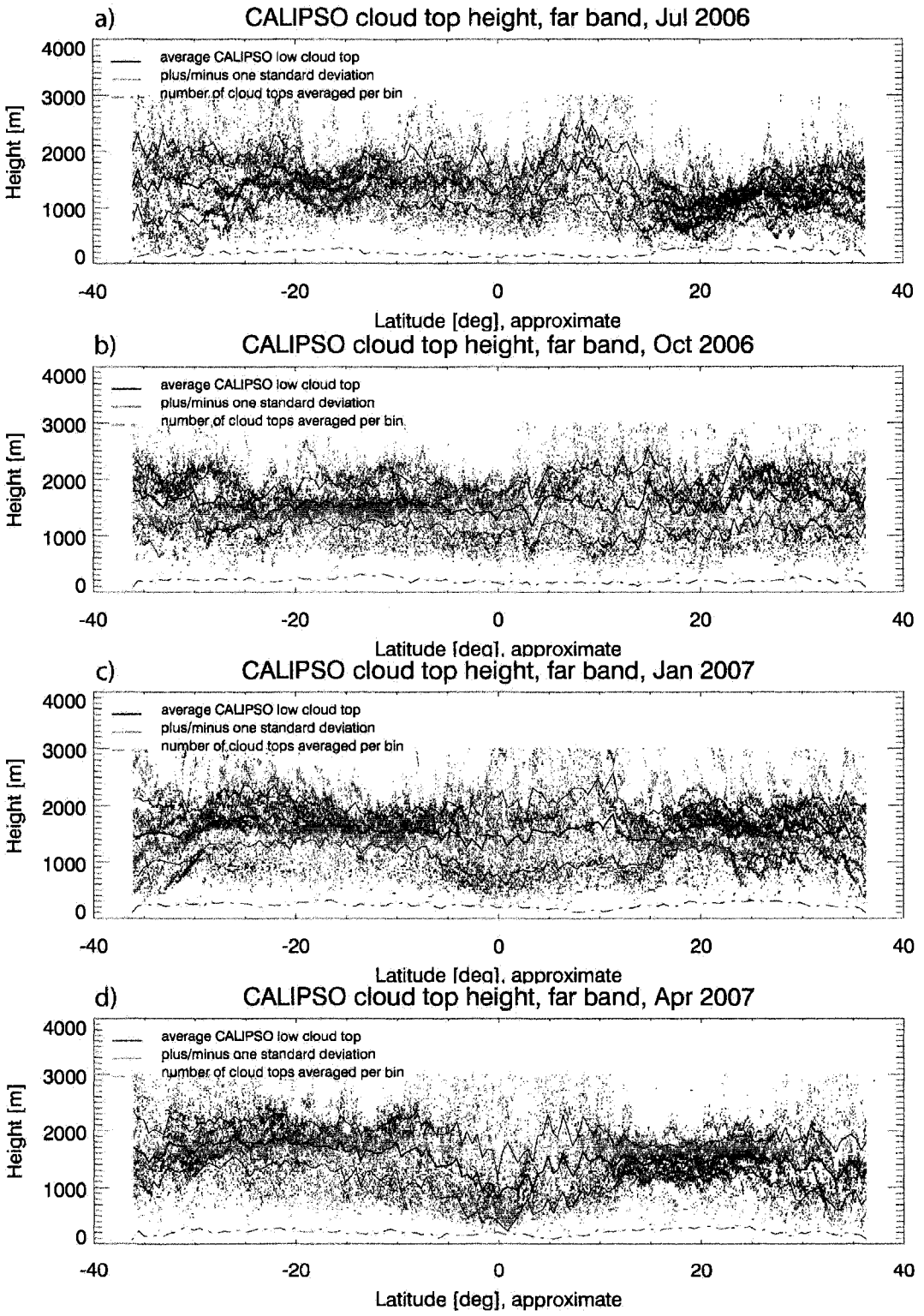

Fig. 6.8 Lowest detected CALIPSO cloud tops, if not exceeding 3 km, parallel to the American coastline (far band). Individual cloud tops marked by green dots. Average cloud-top height along the band plus/ minus one standard deviation plotted as solid thick (thin) line. Number of averaged cloud tops per bin plotted as dot-dashed line.

6.1.4. Trade and transitional cumulus regime

Apart from a shift in the location of the ITCZ, the observed cloud-top height is quite consistent between regions north and south of the ITCZ, and across seasons.

In July, the observed average cloud-top height north of the ITCZ is the lowest of the year, ranging from 1 km to 1.3 km. South of the ITCZ, the values range from 1.3 km to 1.7 km, with similar standard deviation. In October, the southern area changes little, but the northern part of the band becomes more variable, and the average cloud-top heights slightly exceed those in the south. January brings deeper clouds in the south by about 200 m, but not much change in the north. In April, variability lessens again north of the deep convection, and average cloud tops are lower, while the southern areas show little change. As in the near band, the far band shows an area of consistently low cloud tops with good sampling rate between ~3°S and 2°N, framed by areas with higher average cloud tops an variability.

6.2. Low clouds observed by CALIPSO - the diurnal cycle

The local overpass of the CALIPSO satellite occurs at approximately 1:30 am and 1:30 pm at the Equator, plus/minus roughly 12 minutes at 40°N and 40°S. The observations can be split into daytime and nighttime observations. Sampling twice a day is not truly sufficient to observe the full diurnal cycle, but consistent differences between early afternoon and early morning states can certainly be detected.

Fig. 6.9 and Fig. 6.10 show maps of the average low cloud-top height for daytime and nighttime observations only. Since splitting the data by time of day halves the number of observations, there are more bins with low sample numbers. Any grid box

with 35 or fewer averaged cloud tops is cross hatched in these maps. Fig. 6.11 and Fig. 6.12 are the corresponding maps of samples per bin.

The predominant colors alone in Fig. 6.9 and Fig. 6.10 show that higher cloud tops are observed during the night. The color scale indicates an overall shift of about 200 m. It appears that slightly more low clouds are detected during the night than during the day. Indeed, there is less background scatter during the night, making the detection of layers with weak signal easier during the night. However, the clouds targeted here are optically thick and should produce a strong signal, not to be confused with background noise, during daytime as well.

Fig. 6.14 through Fig. 6.16 show the average cloud-top height in the four bands again, this time split for night and day. The general behavior of the average low cloud-top height is the same as for the figures previously discussed, except for an overall tendency towards deeper clouds at night. The difference between daytime and nighttime observations seems to be more pronounced in areas where shallow cumulus or deep convection are likely present. However, those same regions also have greater variability in the observations, making it difficult to assess how significant those differences are. The SEP band is the one with the smallest standard deviation. In the eastern half of the band, the clouds observed during nighttime are on average between 100 m and 300 m deeper than during the day. For the most part, the daytime and nighttime averages are still located within one standard deviation of each other. In the western half of the band, differences can be as large as 500 m. There seems to be little variation of the diurnal differences with season in the SEP band.

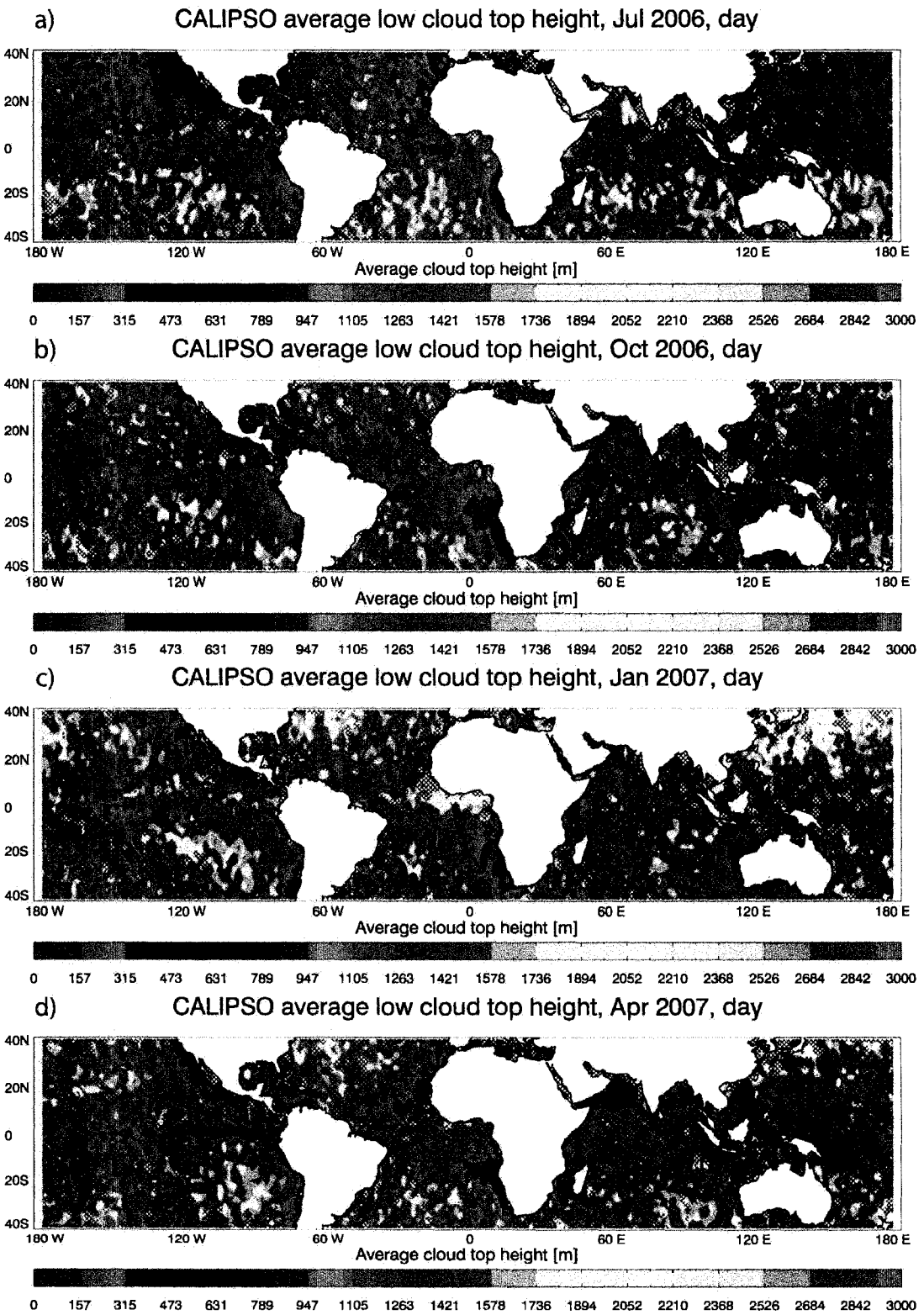

Fig. 6.9 Lowest detected daytime CALIPSO cloud top, if not exceeding 3 km, averaged into 2°x2° bins for the months of July 2006, October 2006, January 2007 and April 2007. Cross hatching indicates areas with ≤35 averaged samples.

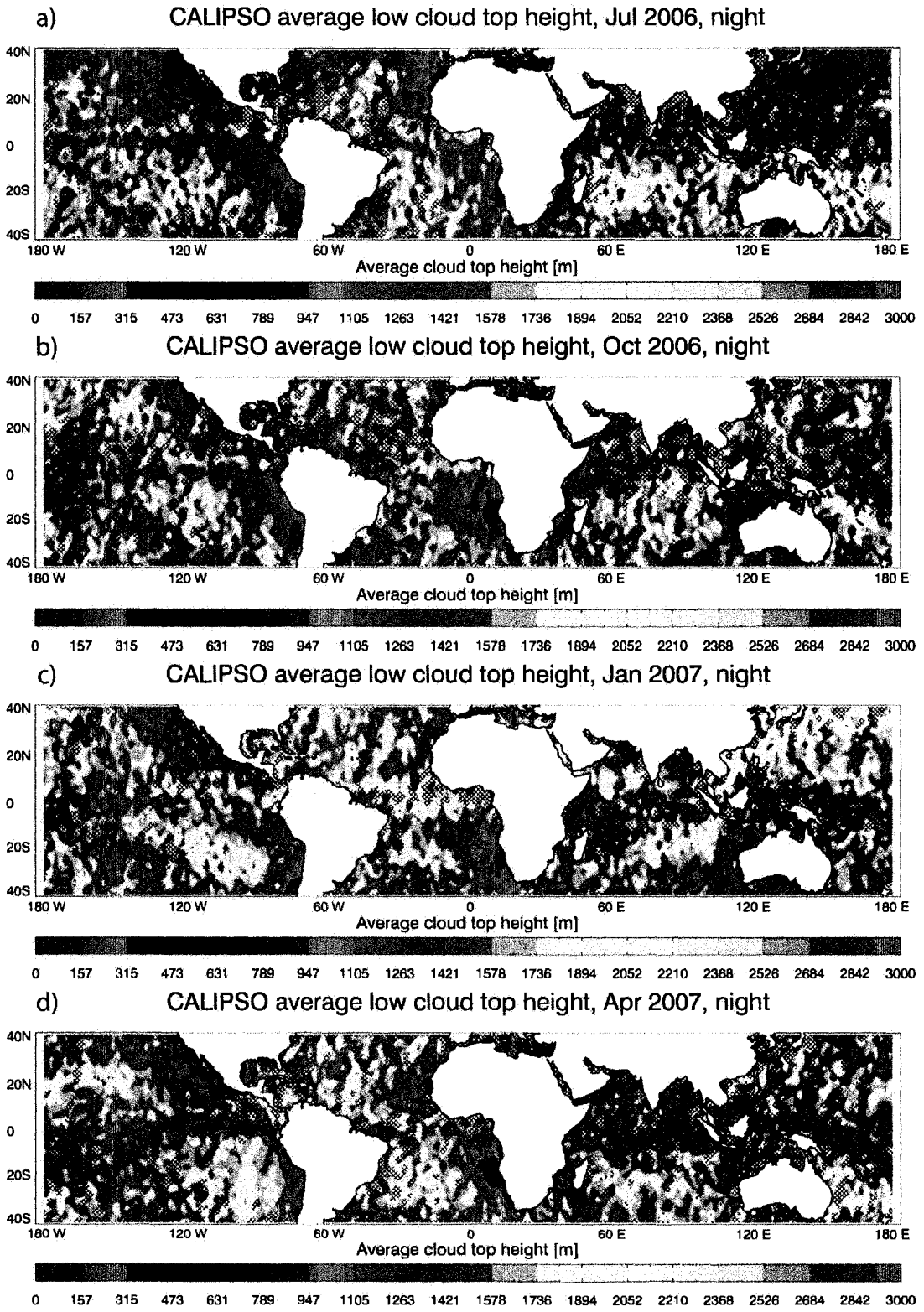

Fig. 6.10 Lowest detected nighttime CALIPSO cloud top, if not exceeding 3 km, averaged into 2°x2° bins for the months of July 2006, October 2006, January 2007 and April 2007. Cross hatching indicates areas with ≤35 averaged samples.

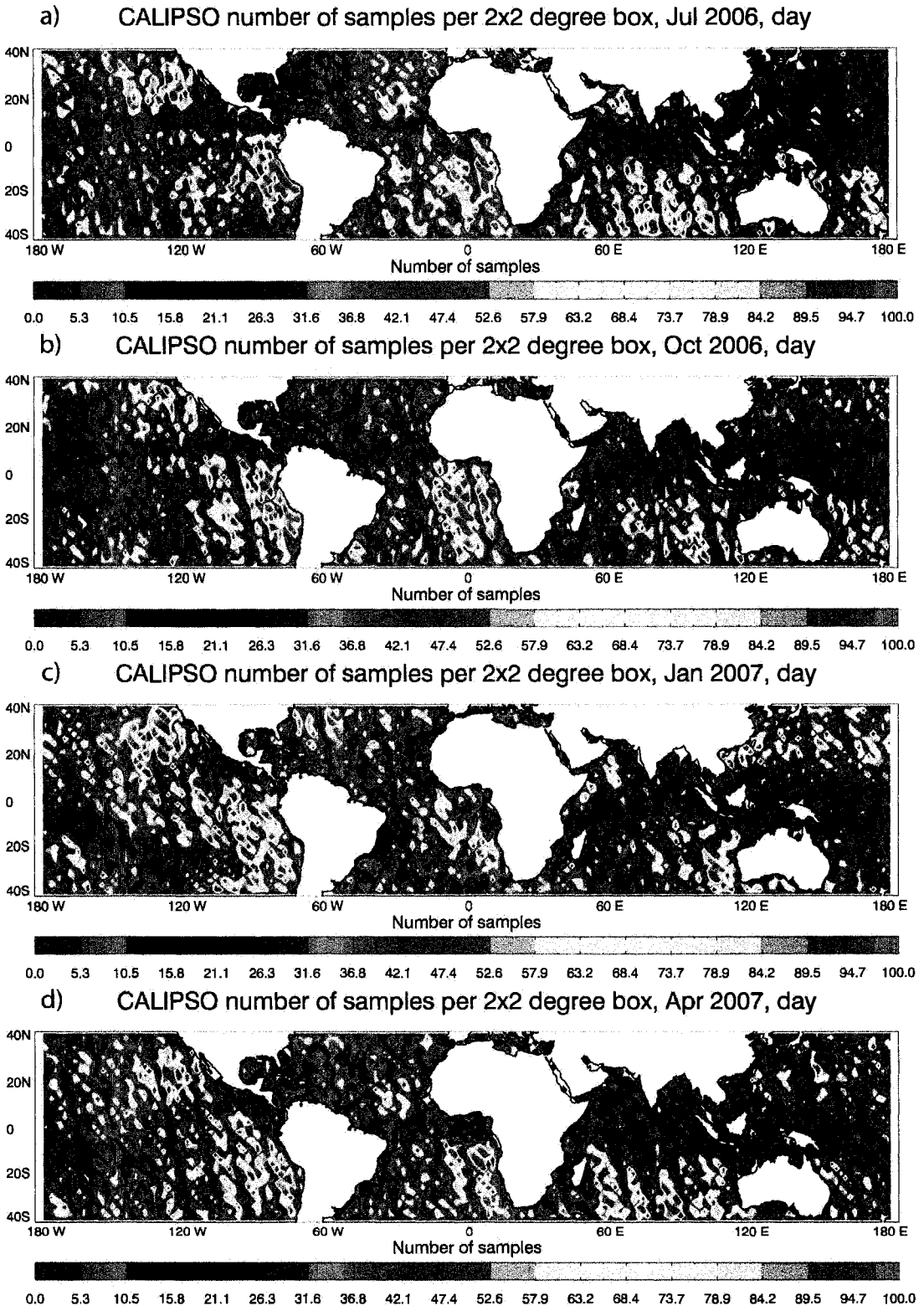

Fig. 6.11 Number of averaged daytime CALIPSO low cloud tops per 2°x2° bin, corresponding to the previous figure, for the months of July 2006, October 2006, January 2007 and April 2007.

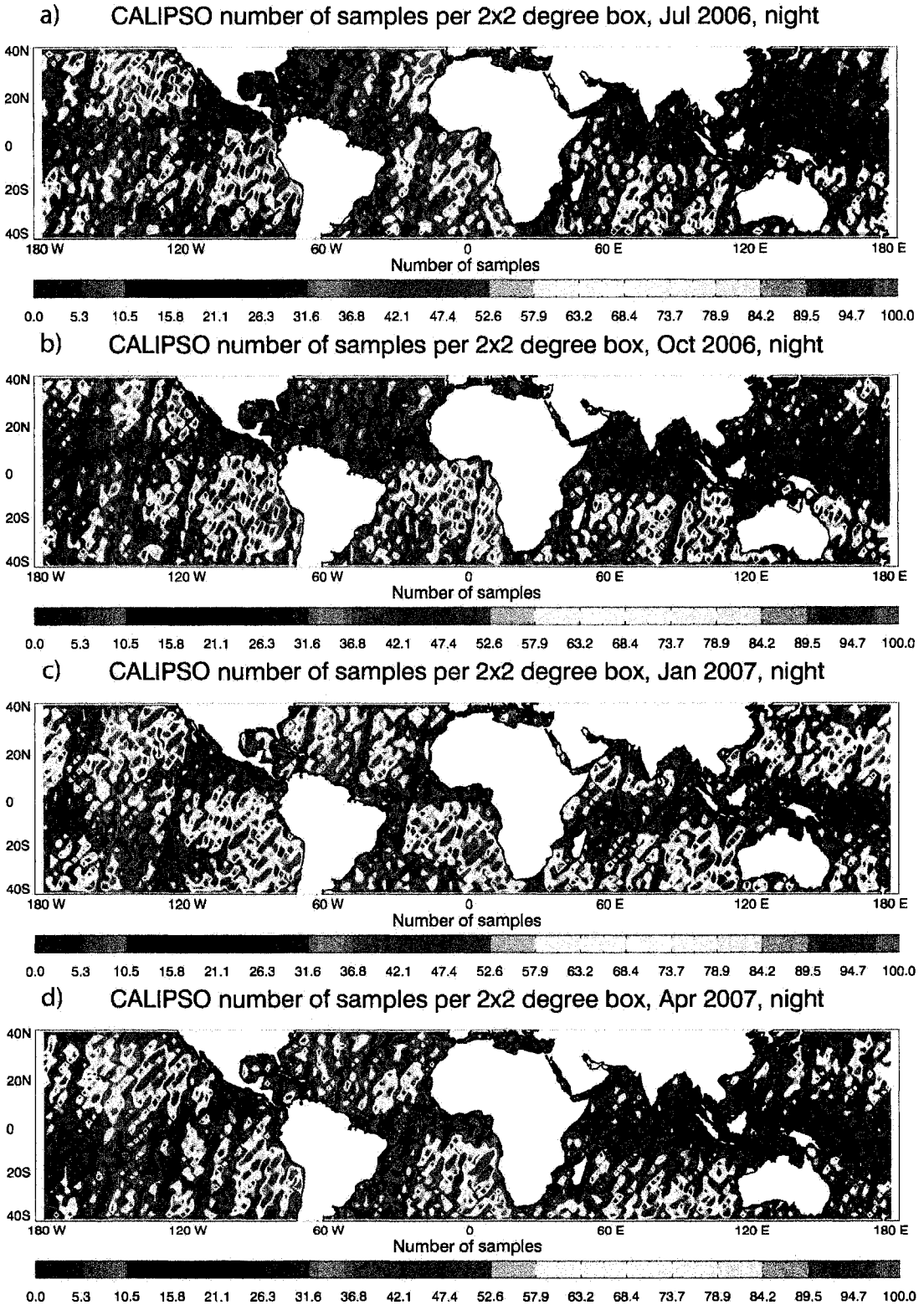

Fig. 6.12 Number of averaged nighttime CALIPSO low cloud tops per 2°x2° bin, corresponding to the previous figure, for the months of July 2006, October 2006, January 2007 and April 2007.

In the Neiburger band, the differences between daytime and nighttime are hard to assess. Due to the orientation of the band, daytime overpasses occur almost perpendicular to the length of the band. As a consequence, the observations from an individual overpass are often averaged into only one or two neighboring bins. Neighboring bins may therefore contain observations of individual overpasses taken several weeks apart, not a long-term average. During the night, the overpasses are aligned more along the length of the band, so that each bin contains samples taken at various times throughout the month. This leads to a smoother average.

The near and far band also show a tendency for deeper clouds during the night. As in the other bands, the observations are quite noisy, making it difficult to assess just how significant these differences are. In the northern part of the far band, for example, the daytime to nighttime differences appear to have some seasonality, being greatest during October, and almost non-existent during January. The near band does not show the same type of seasonality though.

During the East Pacific Investigation of Climate (EPIC) study, a consistent diurnal cycle of the stratocumulus cloud-top height was observed in the South East Pacific (Bretherton et al., 2004, B04 hereafter). The level of the trade wind inversion (observed eight times daily by radiosonde), also marking the stratocumulus cloud top, rose about 200 m each night from an early afternoon low. It appears CALIPSO's overpasses occur at just the right time to capture the full extent of the diurnal cycle. The daytime-to-nighttime differences in the eastern half of the SEP band are consistent with the 200 m mentioned in B04, as is the average cloud-top height: During EPIC, the inversion along the coast ranged between 1000 m and 1200 m within a 24 hour period (from Fig. 4, B04)

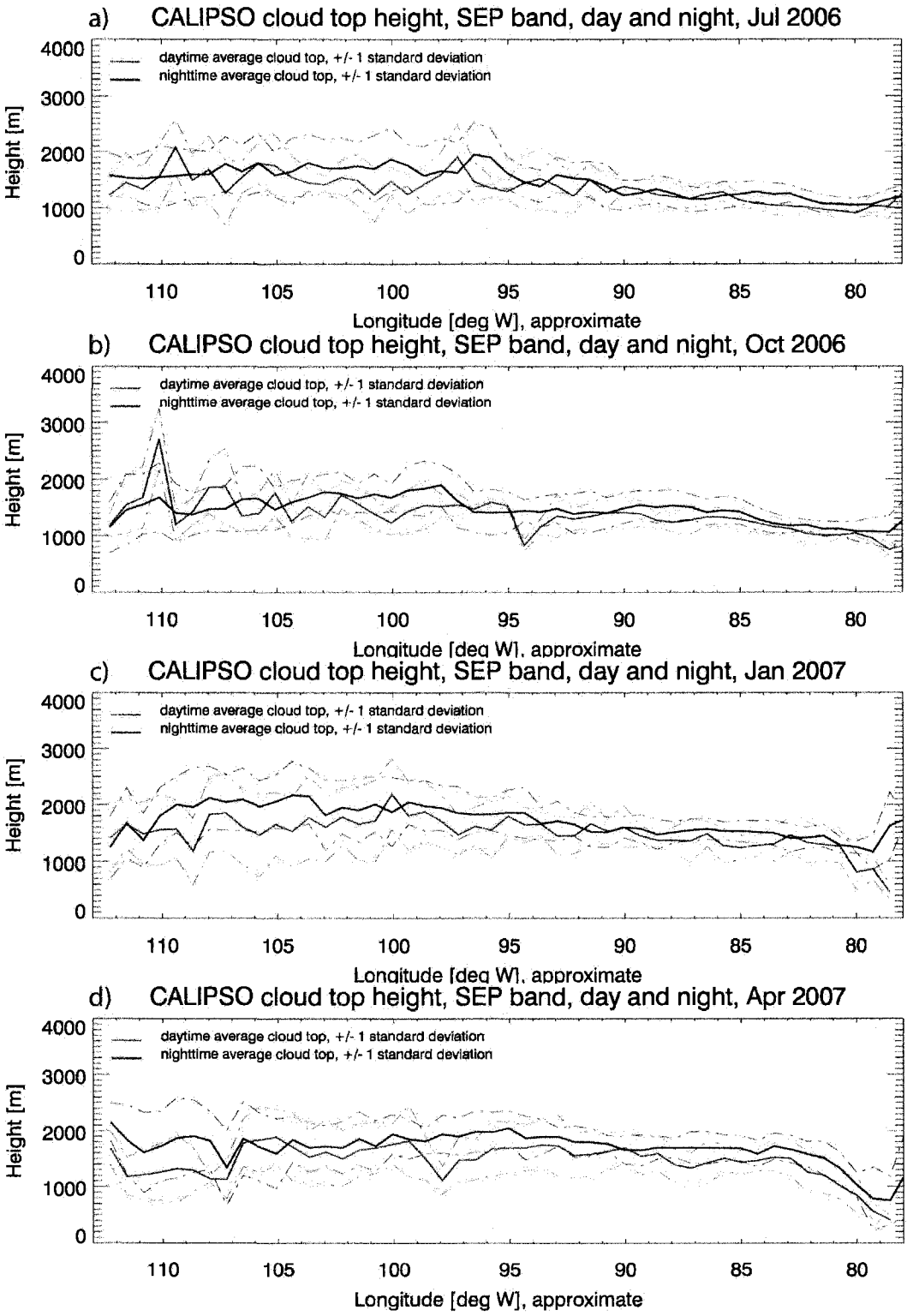

Fig. 6.13 Lowest detected CALIPSO cloud tops, if not exceeding 3 km, along the South East Pacific (SEP) band. Average cloud-top height along the band (plus/minus one standard deviation) plotted as solid thick (dash-dotted) line. Daytime values in red, nighttime values in blue.

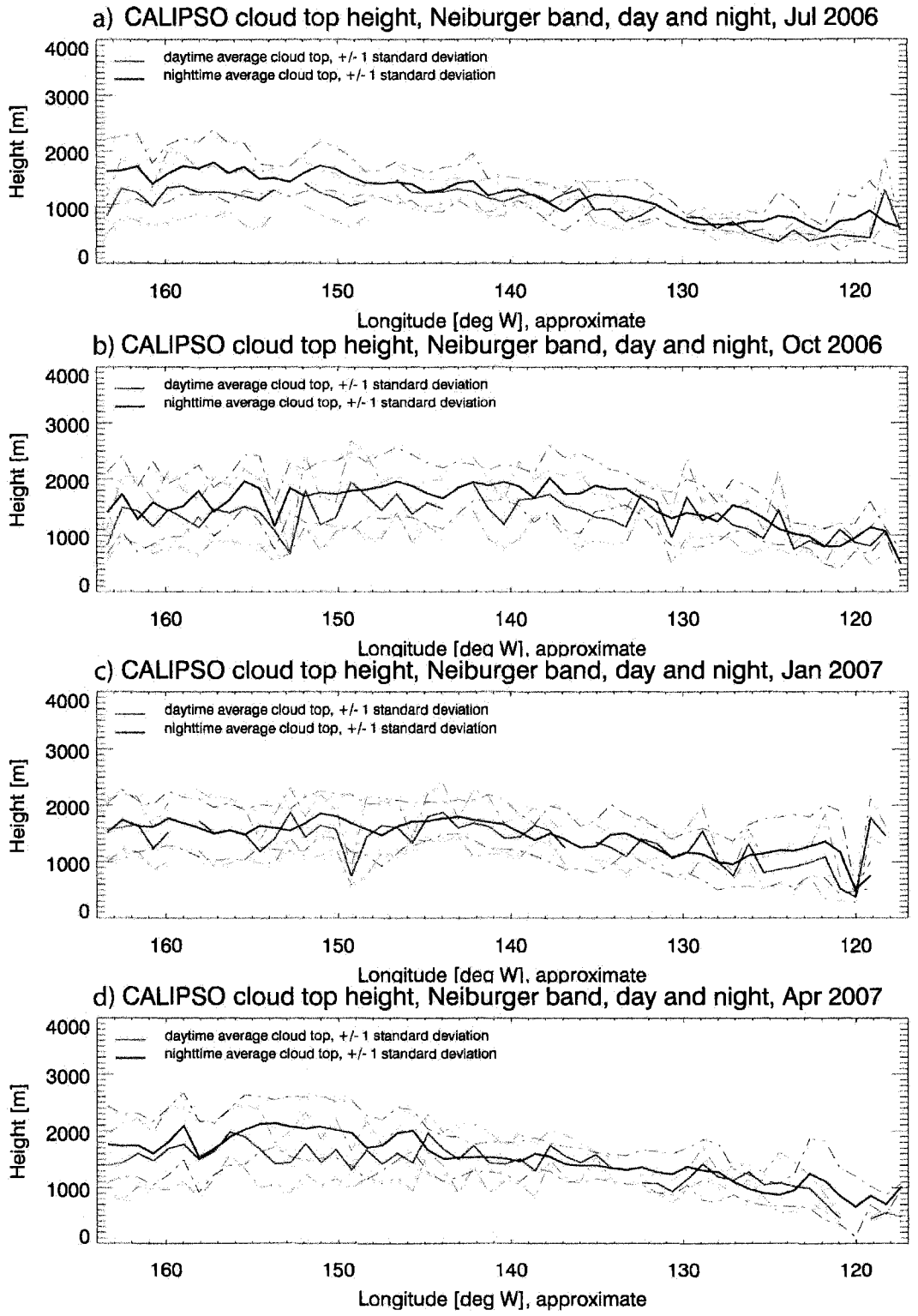

Fig. 6.14 Lowest detected CALIPSO cloud tops, if not exceeding 3 km, along the Neiburger band. Average cloud-top height along the band (plus/minus one standard deviation) plotted as solid thick (dash-dotted) line. Daytime values in red, nighttime values in blue.

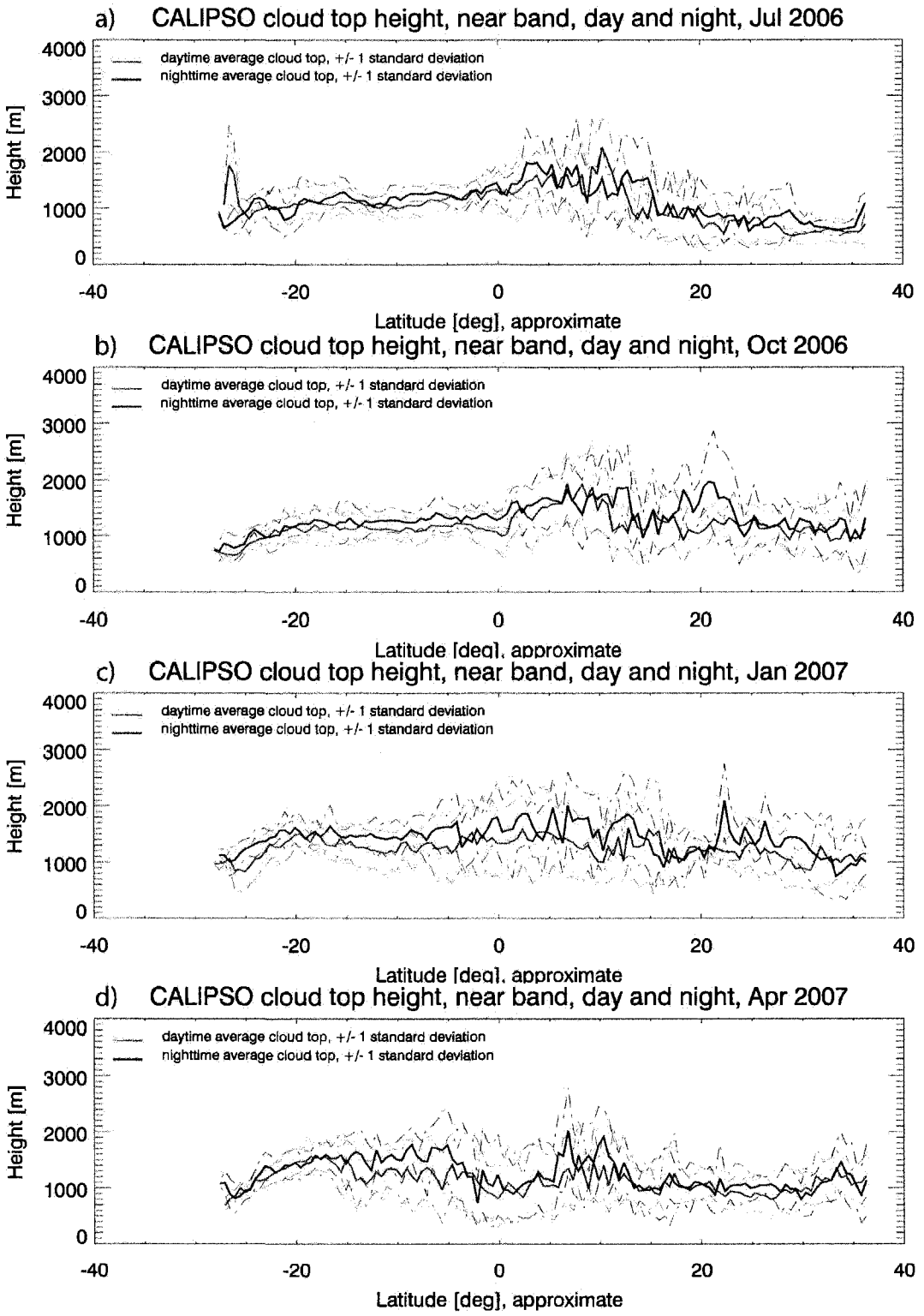

Fig. 6.15 Lowest detected CALIPSO cloud tops, if not exceeding 3 km, along the American coast (near band). Average cloud-top height along the band (plus/minus one standard deviation) plotted as solid thick (dash-dotted) line. Daytime values in red, nighttime values in blue.

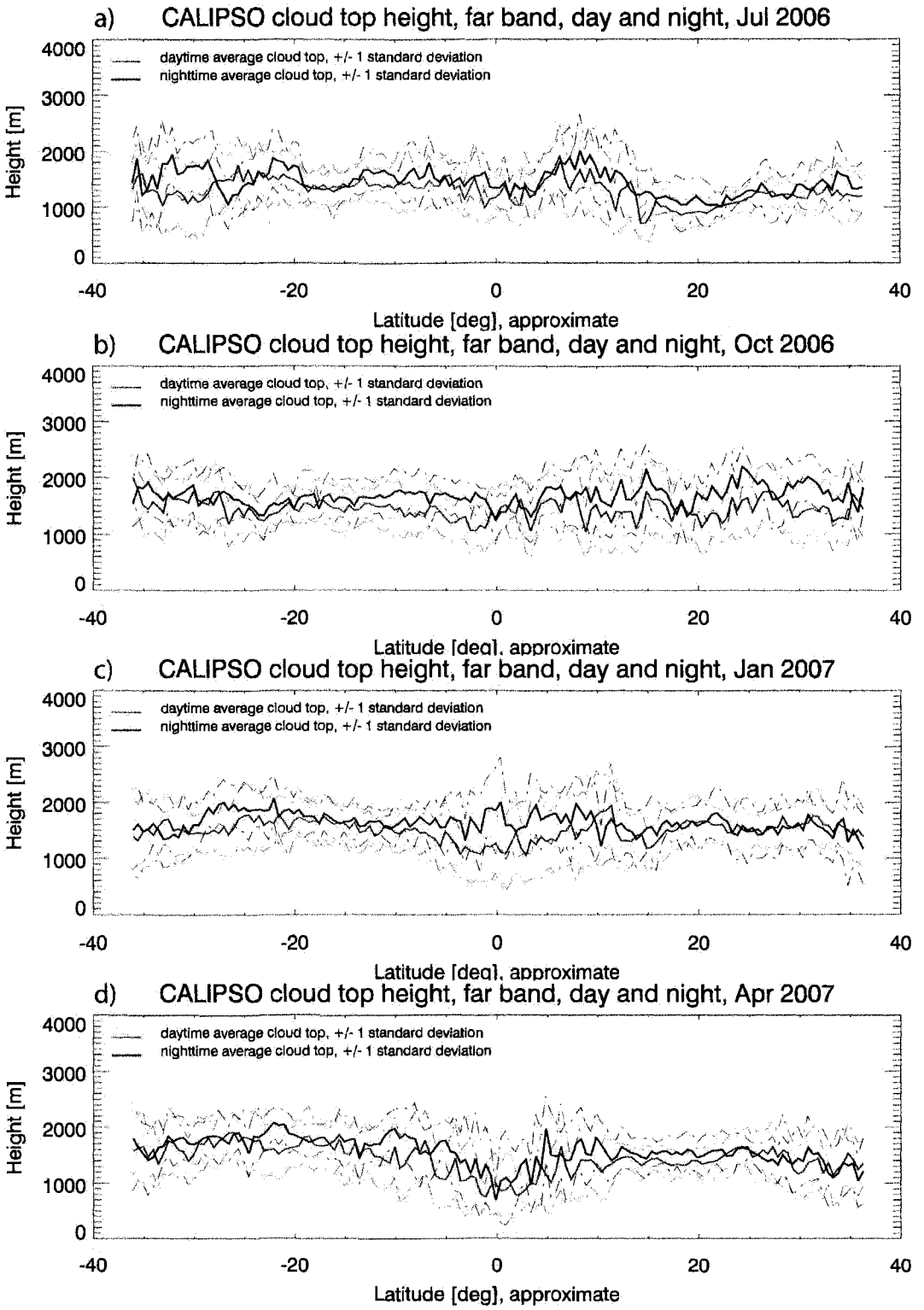

Fig. 6.16 Lowest detected CALIPSO cloud tops, if not exceeding 3 km, parallel to the American coast line (far band). Average cloud-top height along the band (plus/minus one standard deviation) plotted as solid thick (dash-dotted) line. Daytime values in red, nighttime values in blue.

consistent with the 1000 m observed by CALIPSO in October 2006. The observations from EPIC were obtained somewhat further south along the coast than the SEP band's location, but the map in Fig. 6.1b shows little variation in the CALIPSO observations along the coast line. The ship from which the radiosondes were launched during EPIC remained stationary for three days at 20°S and 85°W. The daytime inversion height ranged from approximately 1000 m to 1250 m during this period, the nighttime inversion height between 1300 m and 1500 m. The buoy location lies just outside the SEP band, but is located closest to the bin with center longitude of approximately 87°W. The average CALIPSO cloud-top height lies around 1.4 km at that longitude, with a daytime average of 1.25 km and a nighttime average of 1.5 km. Again, these values seem consistent, considering slight variations in location and the fact that the observations were obtained several years apart, though in the same season. B04 also observe a minimum in cloud fraction and cloud liquid water path coincident with the lowest inversion heights in the early afternoon. Shortwave heating offsets the cloud top radiative cooling. The moisture flux is less efficient in moistening the entrained air, leading to a reduction of cloud fraction and liquid water path.

A similar diurnal cycle in cloud fraction was also observed during ASTEX (Ciesielski et al., 1999; Ciesielski et al., 2001). While the overall cloud fraction in the ASTEX region (North East Atlantic) was lower than in the EPIC study, a minimum in cloud fraction (39%) was observed during the afternoon, and a maximum (54%) in the early morning hours. The authors conclude that the combination of longwave cooling and shortwave heating during the day destabilizes the cloud layer. It becomes well-

mixed and stably stratified with respect to the subcloud layer, and the two layers decouple. The decoupling leads to a thinning or breakup of the clouds in the afternoon.

Klein and Hartmann (1993, hereafter KH93) used surface based cloud climatologies to assess the seasonal changes of stratocumulus extent in various regions of the globe. The CALIPSO observations shown here are not observing stratocumulus amount per se. However, it is not unreasonable to deduce the existence of stratocumulus-type clouds from a combination or low average cloud-top heights and high number of low cloud observations, paired with the knowledge of the typical location of marine stratocumulus. Thus it would appear that the Californian stratocumulus is most consistent and prevalent in July. This agrees with the season of maximum stratus identified as JJA by KH93. July is also the month in which low clouds are most frequently observed around the Canary Islands, again in agreement with KH93. The authors identify the season SON as the one with the most stratocumulus in the South East Pacific, and off the Namibian coast. The South East Pacific doesn't seem to show much seasonal variation in the CALIPSO data, but the area identified as "Namibian" by KH93 (10°S-20°S, 0°-10°E) does indeed have the lowest cloud tops and largest sample numbers in October.

6.3. Adding a new perspective

The following short sections demonstrate how lidar observations can add a new perspective to existing topics and problems.

6.3.1. Low clouds on the Equator in boreal spring

The persistent low cloudiness along the Equator in April 2007 is well visible in the maps (Fig. 6.1d) as well as in the near and far bands (Fig. 6.7d and Fig. 6.8d). Fig. 6.2d

shows that, apart from a small area at the coast, the number of averaged cloud top observations is quite good along the Equator. The location of the low cloud tops is consistent with the location of the coldest observed sea surface temperatures during that month (NOAA SSTs, not shown here) and the SSM/I ocean rainfall product (not shown) confirms the existence of a double ITCZ. Since the model runs for this study are limited to the GLAS period in the fall of 2003, the model is no help here in assessing what circulatory structures may contribute to the area of suppressed convection and low cloudiness.

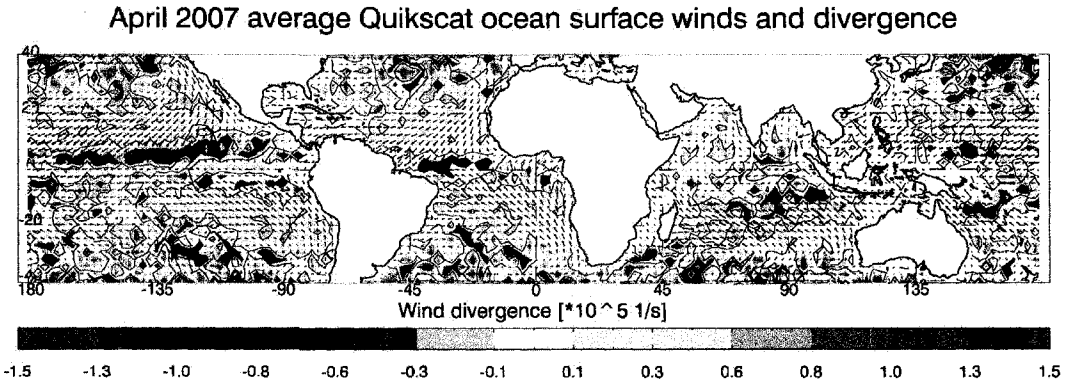

Fig. 6.17 Quikscat ocean surface winds averaged for April of 2007.

Fig. 6.17 shows the divergence and surface winds calculated from the Quikscat Level 3 daily gridded ocean wind vectors. Two bands of surface convergence mark the double ITCZ, with moderate divergence (~0.7×10^{5} s^{-1}) along the Equator. It is reasonable to assume that the air between the two bands of convection is probably subsiding.

6.3.2. Mid-level clouds over the Equator - ITCZ outflow?

The GLAS lidar frequently observes mid-level clouds near the Equator in the East Pacific. These clouds are usually detected on the descending (approximately 7 am local time) overpass. CALIPSO does not observe similar clouds in the same season (October)

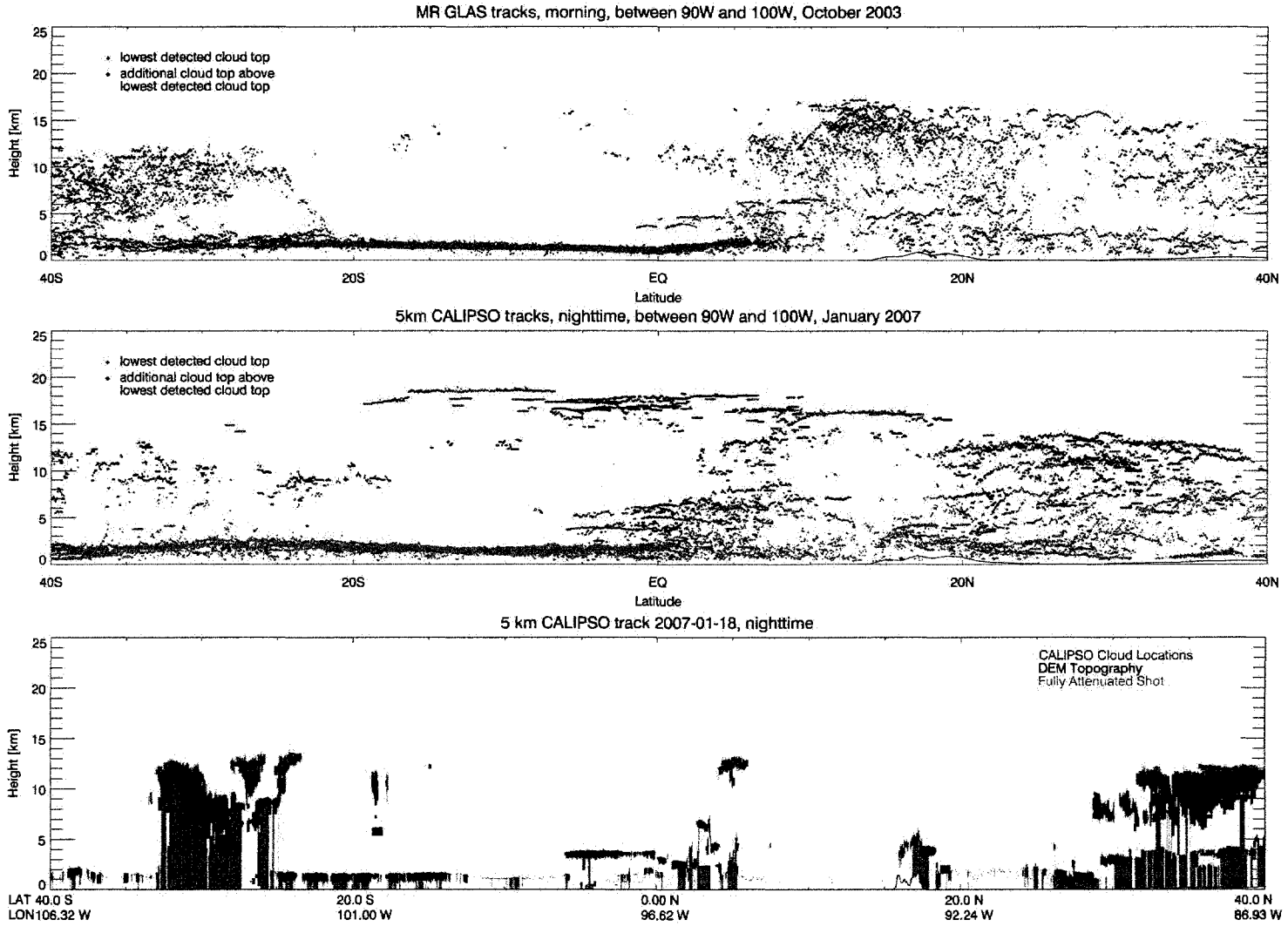

Fig. 6.18 GLAS and CALIPSO tracks showing mid-level clouds over the Equator. Top and middle panel show all cloud tops between 90°W and 100°W for October 2003 (GLAS,) and January 2007 (CALIPSO). Black line is average topography. Bottom panel shows single CALIPSO track.

but it does see them in the nighttime January overpasses. About half of the time, the mid-level clouds do not fully attenuate the lidar signal, suggesting that these clouds are not optically thick. This could be an indication that these clouds are detrained, rather than a shallow convective clouds. A shallow meridional return flow has been observed in this region of the Pacific. Low level southerly winds flow into the ITCZ. The air rises and returns south as a shallow northerly flow around 2 to 4 km, and a high branch near the tropopause (Zhang et al., 2004, McGauley et al., 2004). The clouds observed by CALIPSO and GLAS tend to be located somewhat higher, between 3 km and 7 km. Whether these clouds are indeed outflow from the ITCZ cannot be determined by the lidar observations alone. They confirm however that under certain atmospheric conditions, optically thin mid-level clouds are common in the Eastern Equatorial Pacific.

6.3.3. Systematic differences between cloud regimes in the North East Pacific and the South East Pacific

While the North East and South East Pacific regions have many similarities, such as cloud regimes, cold ocean upwelling along the coast, and persistent subsidence throughout most of the troposphere, there are some indications of systematic differences between these regions as well. As discussed above, the seasonality of the low cloud height is much less pronounced in the SEP compared to the NEP. The variability of day-to-day lidar observations of the cloud-top height is also much lower in the SEP.

In the previous chapter, the two regions proved to have different sensitivity to changes in the formulation of the model's boundary layer scheme. In the NEP region,

relaxing the Klein and Hartmann stability criterion led to significantly more *Sc*-type clouds, whereas in the SEP region, changing the environmental mixing of the lifted test parcel led to a greater change. This sensitivity is consistent with the weaker trade inversion in the NEP (see *Sc* composite temperature profile).

There is some evidence that the balance between radiative forcing, surface fluxes, advection and entrainment maintaining the persistent trade inversion differ in the two regions. Wood and Bretherton (2004) estimate cross-inversion entrainment rates from a combination of boundary layer depth, surface temperature and model-derived subsidence rates and find that while entrainment rates are strongest along the coast in the NEP, they actually increase with distance from the coast in the SEP. Estimated entrainment rates are also about 50% stronger in the NEP stratocumulus regions compared to the SEP stratocumulus regions. Wood and Bretherton (2004) suggest this may be due to varying balances between the inversion strength (a weaker inversion favoring stronger entrainment) and the turbulence in the boundary layer (weaker turbulence hindering entrainment). Ahlgrimm and Randall (2006) explore the balances maintaining the trade inversion using a bulk boundary layer model and find that entrainment in the NEP is mainly balanced by advection of cool, dry air, while in the SEP, a local balance between radiative forcing and entrainment dominates.

The lidar data can contribute to further studies of this type by providing more reliable observations of the boundary layer height for all seasons.

6.3.4. Location of boundary layer top and cloud top in transitional cumulus regions

GLAS can detect the gradient in aerosol concentration that frequently marks the boundary layer top. Since the algorithm searches for the boundary layer top by looking for the first significant decrease in backscatter strength from the ground up, the cloud top of optically thick boundary layer clouds is often marked as the boundary layer top.

Usually, the boundary layer in the stratocumulus regime is considered to be well mixed to the cloud top. And indeed, for the non-precipitating case, moist conserved variables are near-constant throughout the depth of the boundary layer. In the trade cumulus regime, the well-mixed area is confined to the subcloud layer, but the trade inversion still caps the cloud top. How and where the stratocumulus regime transitions into the trade cumulus regime is still under investigation. The lidar observations suggest several scenarios. The figures discussed in this section (Fig. 6.19) show the observed cloud top and base (connected by a blue line) for select HR GLAS tracks in the central Pacific. Also shown are the location of the detected BL top (light and dark green dots) and of the level of full signal attenuation (red dots). The quality of the BL retrieval is assessed by comparing the backscatter signal strength at the detected BL top to the signal 500 m above in, presumably, clear air. The quality flag is not only a confidence rating, but by its nature also distinguishes between BL tops coincident with cloud tops (very strong backscatter signal) and clear air BL tops (weaker signal). Boundary layer retrievals with weaker signal (quality flag 1 through 9) are shown as light green dots, retrievals with strong signal (flag 10 through 13) as dark green dots.

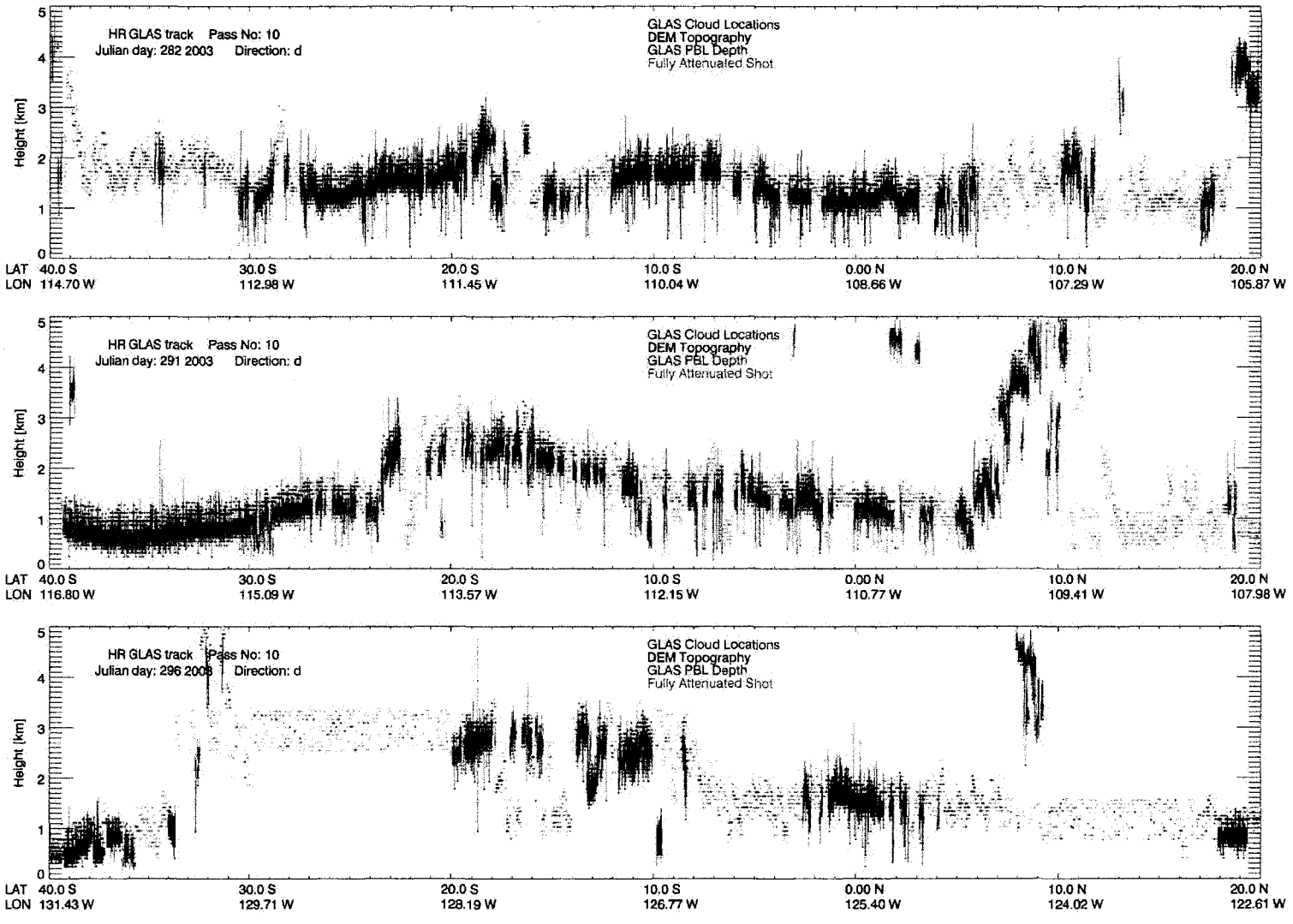

Fig. 6.19 Individual GLAS tracks showing location of low clouds (blue lines), boundary layer top (green dots) and attenuated cloud bases (red dots).

In clear air (no boundary layer clouds), the BL tops can be spread out over an 800 m thick layer (Fig. 6.19c, around 25°S and 10°N). This indicates that the aerosol gradient marking the BL top is quite diffuse, and individual lidar shots place the BL top at varying heights. These BL tops have usually low signal strength (light green dots).

Typical stratocumulus clouds are marked by strong BL tops (dark green dots) with little spread, right above the cloud layer (blue lines), which attenuates the signal fully within a few hundred meters (red dots) (Fig. 6.19b, south of 25°S).

Where the cloud cover is broken, the BL tops detected in the clear areas in between can be located at various heights (e.g. Fig. 6.19b at the Equator, Fig. 6.19a between Equator and 10°S). If the clear BL top is located at approximately the same height as the cloud tops left and right, the strongest aerosol gradient lies right around the cloud-top height. This would suggest a well-mixed boundary layer all the way to the cloud top level, and the clouds are likely broken stratocumulus.

In other locations, the BL top in a clear gap lies significantly lower than the cloud tops around (e.g. Fig. 6.19c between 15°S and 20°S, Fig. 6.19b around 7°S). In this case, the well-mixed boundary layer is confined below the clouds. The cloud layer is possibly decoupled. In any case, the top of the subcloud layer has a stronger aerosol gradient than the trade inversion. This resembles the trade cumulus scenario.

Quite often, the cloudy layer lies within the spread of the BL retrievals, and individual tracks can contain all of the scenarios described above. Still, the lidar has the potential to distinguish between partially cloudy regions that resemble broken stratocumulus (BL at level of cloud top) and regions that resemble trade cumulus conditions (BL significantly lower than cloud top level). While it is fascinating to look

at individual tracks, a longer lidar record, such as from CALIPSO, could shed some light on the question where and under what circumstances one or the other regime exists, and when and where a transition between regimes occurs.

6.3.5. Seasonal changes in the ITCZ high clouds

Several studies on high clouds have been conducted with the GLAS observations (Dessler et al., 2006a; Dessler et al., 2006b). CALIPSO now provides an opportunity to look at seasonal changes in these clouds. Here, we have chosen to examine the cloud-top height distributions of high (>10 km) clouds in the region of the Intertropical Convergence Zone (ITCZ). In order to capture these clouds, all lidar observations between the Equator and 20°N, and 160°W to 100°W are examined. Histograms for the highest detected optically thin (non-attenuating) and thick (attenuating) cloud tops are shown in the following figures. The seasonal migration of the ITCZ within the specified boundaries should not influence results much since clouds outside the ITCZ will most likely have cloud tops below 10 km and will not be counted. The exception is the southern branch of the double ITCZ in April, which is discussed below.

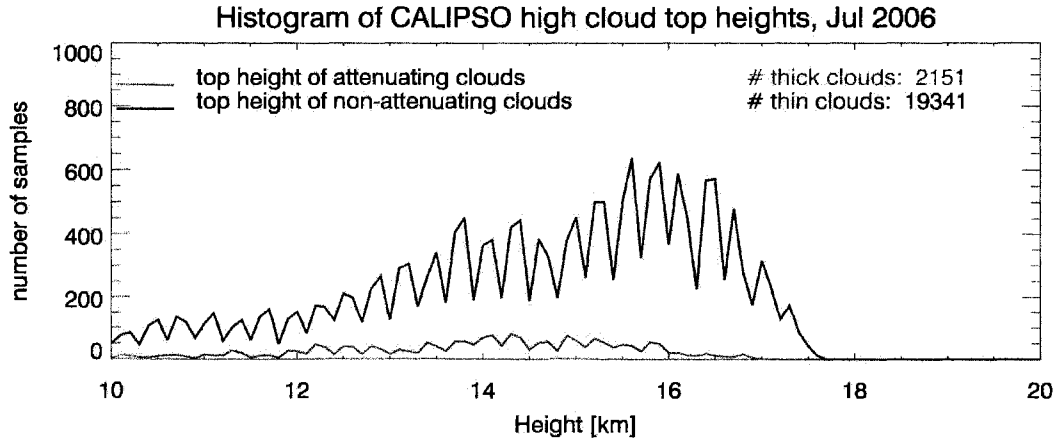

Fig. 6.20 Histogram of highest detected cloud top from CALIPSO in July of 2006 in the ITCZ region (0° to 20°N, 160°W to 100°W)

July and October of 2006 (Fig. 6.20 and Fig. 6.21) have similar cloud-top height distributions, with significantly more optically thin clouds (factor 7 to 8) and a maximum for thin clouds between 15 km and 16 km. The distribution for optically thick clouds mirrors the shape of the thin clouds, but with a maximum at slightly lower height (14 km to 15 km).

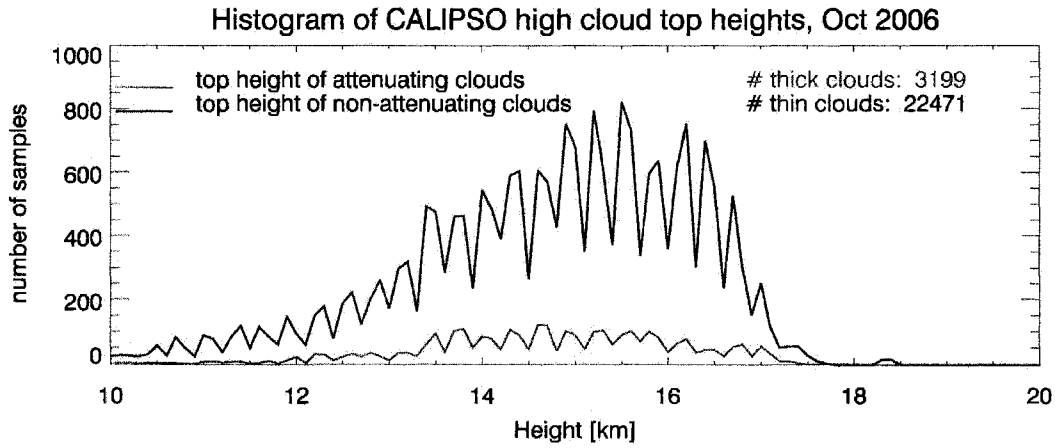

Fig. 6.21 Histogram of highest detected cloud top from CALIPSO in October of 2006 in the ITCZ region (0° to 20°N, 160°W to 100°W)

The picture is quite different for January 2007 (Fig. 6.22). The distribution of optically thin clouds has two maxima, between 13 km and 15 km, and around 17 km. The distribution of optically thick clouds has its maximum near 12 km, about a kilometer lower than the first maximum in the thin-cloud distribution. A corresponding second peak at higher altitude is missing. The ratio of total thick to thin clouds is similar as in July. The higher maximum in the thin cloud histogram may be related to a higher tropopause level, or maybe more vigorous convection injecting cloud water deeper into the tropopause layer.

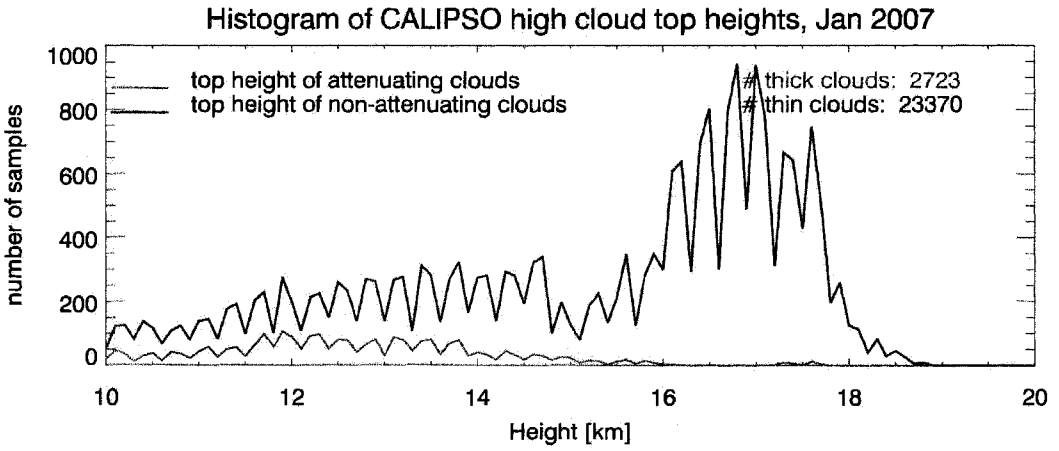

Fig. 6.22 Histogram of highest detected cloud top from CALIPSO in January of 2007 in the ITCZ region (0° to 20°N, 160°W to 100°W)

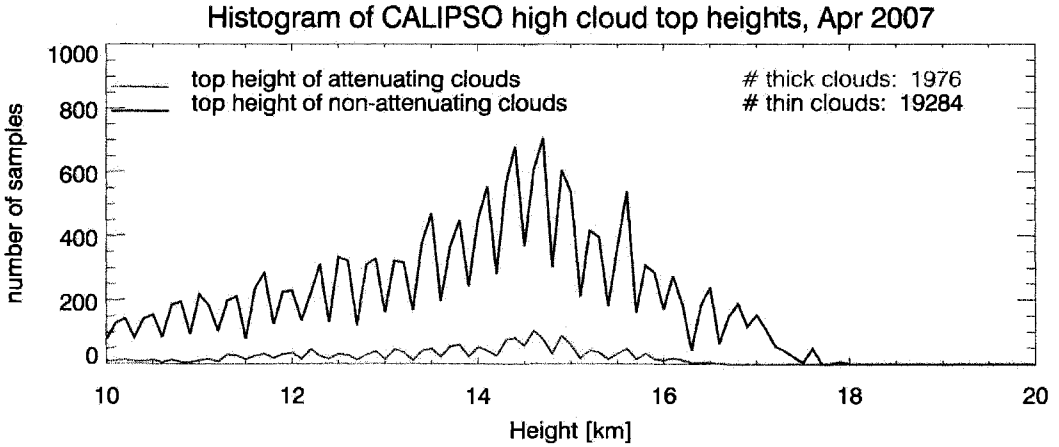

Fig. 6.23 Histogram of highest detected cloud top from CALIPSO in April of 2007 in the ITCZ region (0° to 20°N, 160°W to 100°W)

In April (Fig. 6.22), the shape of both curves resembles the July and October figures again. The maxima are located at slightly lower altitude (14 km to 15 km) for both optically thin and thick clouds. In April, the ratio of thin to thick clouds is greatest (almost 10).

Since the ITCZ is not confined to the northern hemisphere in April, a similar figure as Fig. 6.23 is created for the southern hemispheric branch of the double ITCZ between the Equator and 15°S, and 145°W and 85°W. Optically thick clouds are even rarer in the southern branch of the ITCZ (factor 20). Since fewer clouds are found in the southern

branch compared to the northern branch for an equivalent sized region, the ordinate in Fig. 6.24 has a different scale. The shape of the distributions is similar to January, with a double peak in the thin clouds, and a single peak in the thick cloud distribution.

Dessler et al. (2006a) examine thin, near-tropopause level cirrus (TNTC) from the GLAS L2A period. The optically thin clouds between 16 km and 18 km in Fig. 6.22 and Fig. 6.24 could be classified as TNTC. Dessler et al. (2006b) conclude that while low temperatures at the tropopause play a role in the formation of TNTC, temperature alone is

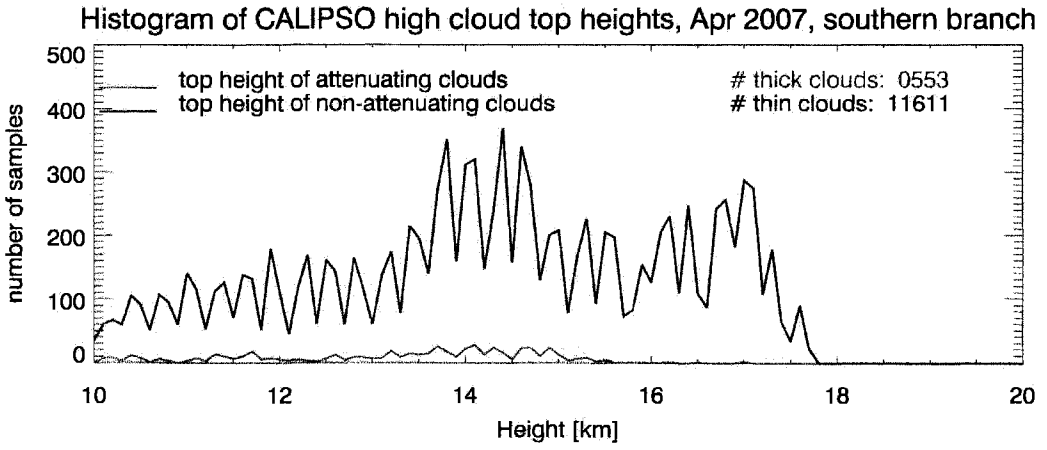

Fig. 6.24 Histogram of highest detected cloud top from CALIPSO in April of 2007 in the southern branch of the ITCZ region (0° to 20°S, 145°W to 85°W)

not a good predictor for the existence of TNTC. The authors find that high occurrence of TNTC clouds tends to occur in areas with vigorous convection (low OLR) and suggest that convection may play a role in TNTC formation. An investigation into the differences between the April and January ITCZ vs. the ITCZ in other months might lead to some answers.

6.4. Summary

With the availability of CALIPSO data, very accurate global observations of low cloud top height are now available for all seasons. Average maps for four months show a seasonal cycle in low-cloud top height over the oceans, which is particularly pronounced in the North East Pacific. Low clouds over the southern hemispheric ocean appear to be less affected by seasonal changes.

CALIPSO's overpasses occur at just the right local time to capture the maximum extent of the diurnal cycle in the low-cloud top height. During the night, the low-cloud top is located approximately 200 m higher than during the early afternoon, with some regional variations. The variability of low-cloud top height over ocean, both throughout the month and from day to night, is weaker for stratocumulus clouds than for trade cumulus clouds.

In addition to the unprecedented global cloud-top height observations, the lidar also adds a new dimension to existing well-studied topics, such as the seasonal double ITCZ in the East Pacific, the location of the boundary-layer top in relation to the cloud base in the transitional and trade regimes, and the systematic differences between stratocumulus regimes in the North and South East Pacific.

Chapter 7: Conclusions

In this study, the use of space-borne lidar observations for the comparison with, and evaluation of modeled clouds is explored. Four versions of the ECMWF Integrated Forecast System and two versions of the Goddard Earth Observing System model (GEOS-5) are assessed for their ability to produce marine boundary layer clouds. In order to do so, two cloud types are defined: a stratocumulus type (*Sc*), and a trade cumulus or transitional cumulus type (*TCu*). Samples in four oceanic regions are classified into those categories, and the frequency of occurrence, location, and properties of the samples compared between models and observations.

The first version (CY28R3) of the ECMWF model produces only about one third of the observed number of *Sc* samples. The generated clouds tend to have lower cloud tops than observed. With the introduction of the eddy diffusivity mass flux (EDMF) boundary layer scheme in CY29R1, the number of *Sc* samples increases somewhat, but the cloud top height is underestimated even more severely than in CY29R3. The cloud fraction distribution for the *Sc* samples becomes more realistic, though. A sensitivity run with less environmental mixing of the boundary layer test parcel in the EDMF scheme (CY29R1-E) improves cloud top height of the *Sc* clouds in the model. A second sensitivity run in which weaker lower-atmospheric stability is required by the EDMF scheme to produce clouds (CY29R1-S) leads to a greater number of *Sc* samples and better distribution of *Sc* samples in the four regions.

All four of the model runs tend to underestimate the number of clouds with near-100% cloud fraction, but overestimate the number of samples with low cloud fraction. Overall, all model versions produce about 10 to 12% more cloudy samples than observed. While the lack of high-fraction clouds is improved in the CY29R1 model runs, the overabundance of (primarily) low-fraction clouds remains. This is no surprise, because the shallow convection parameterization that is primarily responsible for the generation of the low-fraction (*TCu*) clouds is unchanged. As a result, the total low (< 4 km) cloudiness in the subtropical belt is overestimated by 2% to 5% in the model versions. On the plus side, the cloud-top height distribution for the clouds classified as *TCu* is comparable to the GLAS observations.

Low clouds in the four ocean regions discussed in this study react differently to the sensitivity runs of the ECMWF model. In the North East Pacific, the stability criterion in the EDMF formulation is more of a limiting factor to the production of *Sc* clouds than the parcel-drying of environmental air. This is even more pronounced in the regions west of Australia. In contrast, the South East Pacific and South Atlantic regions respond more strongly to the change in the parcel-entrainment formulation. Ideally, of course, any changes made to the parameterization should lead to improvements everywhere. The fact that this is not the case shows that the parameterization is not able to properly represent all of the boundary-layer processes. However, the varying sensitivity to parameter changes in the scheme is consistent with other studies showing that the balances maintaining the persistent marine stratocumulus decks vary between regions (Wood and Bretherton, 2004).

The uncertainty in the above analysis associated with comparing cloud fractions from a transect (GLAS) to the area cloud fraction of a model grid column is estimated to be around 5% of the classified samples. Using the Astin and van de Poll (2001) method to calculate confidence intervals from the FR GLAS observations, about 5% of *Sc* samples could possibly be misclassified and should in fact be in the *TCu* category. This error margin does not qualitatively alter the conclusions drawn from the model evaluation in this study.

The same method of model evaluation was applied to the GEOS-5 model in two versions. The analysis shows an excess of fog in the first version (GEOS1). This excess is substantially reduced in the second version (GEOS2), leading to better agreement with observations. The cloud-top height of the *Sc* clouds is comparable to the observations in GEOS2, but is unrealistically small in the first version (GEOS1), due to the high number of fog clouds with low tops. Similar to the ECMWF model, both versions of GEOS-5 have an overabundance of low-clouds in the subtropical belt (about 8%), leading to overestimations of the total low-cloud (>700 hPa) fraction by 5.1% and 2.4%, respectively. The shape of the low-cloud fraction distribution contributes to this problem with an excess of clouds with fractions 10% and lower, a lack of 100% fraction clouds, and too many samples in the range of 65% to 95%.

What distinguishes this model evaluation from previous work is the attempt to not only verify whether the model produces the observed clouds, but, in case of the ECMWF model, also to understand why the model falls short and to make specific suggestions for further improvement.

Observations from CALIPSO illustrate the seasonal and diurnal cycles of low-cloud top height and frequency of occurrence in the subtropical belt. The cloud-top heights observed are generally consistent with previous ground-based observations of the inversion height. In the trade-cumulus regions, the cloud-top heights are more variable than in the stratocumulus regions. Variability is also greater in the North East Pacific compared to the South East Pacific. The diurnal cycle of the inversion height observed during the East Pacific Investigation of Climate (Bretherton et al. 2004) compares well to the diurnal cycle observed by CALIPSO in the same region. In the stratocumulus regions, the cloud top tends to be about 200 m higher during the early morning overpass of the satellite, compared to the early afternoon overpass. In the trade cumulus regions, this difference tends to be slightly greater, but also more inconsistent.

While the southern oceans show little seasonal change in the observed number and top heights of low clouds, the northern oceans, particularly off the Californian coast, vary seasonally both in cloud-top height and sample number. The stratocumulus clouds have their lowest tops in July in the North East Pacific. The migration of the ITCZ is evident as a shifting area with few observed low clouds.

These low-cloud observations from GLAS and CALIPSO are the first of their kind. In the second part of Chapter 6, we demonstrate that the lidar observations can also contribute to previously studied topics by adding a new perspective.

In the boreal spring (April 2007), CALIPSO observes a large number of clouds with very low tops along the Equator in the East Pacific. Other observations confirm the existence of a double ITCZ in this month. It is likely that a low inversion along the Equator caps the low clouds between the two rising branches of the ITCZ.

GLAS observations from October 2003 show optically thin mid-level clouds between the Equator and 5°N in the East Pacific. Similar clouds are observed by CALIPSO in January 2007, but not in the other three months shown. Since these clouds are usually optically thin, it is unlikely that they are active convective clouds. They may be evidence of a shallow return circulation out of the ITCZ as discussed by Zhang et al. (2004) and McGauley et al. (2004).

The ability of GLAS (and potentially CALIPSO) to distinguish between cloudy and clear boundary-layer tops is demonstrated. A longer record from CALIPSO may help to determine where and under what circumstances the marine boundary layer transitions from a well-mixed layer to a decoupled layer with shallow convection.

Semitransparent cirrus clouds have been the subject of much study lately (Dessler et al. 2006a, Dessler et al., 2006b), since these clouds have a potentially large impact on radiation, while being hard to detect by passive satellite sensors. CALIPSO observations show that the level at which optically thin cirrus clouds are located in the ITCZ region varies with season. While the height of these clouds is usually consistent with detrainment from the tops of optically thick clouds (probably convective cores and thick anvils), in some months, thin clouds can be found kilometers above the tops of the optically thick clouds.

The lidar observations may seem to raise more questions than they answer in these cases. But they may just provide the missing piece of information to solve the puzzle.

Outlook

The era of the space-borne lidar has just begun. CALIPSO will hopefully provide more observations for several years to come. This study has focussed on lidar

observations alone, and one type of clouds, namely marine boundary layer clouds. However, combining lidar data with other observations from the A-train will alleviate some of the lidar's weaknesses, such as signal attenuation and a narrow foot print. The methods for model evaluation developed and demonstrated in this study can be easily adapted for CALIPSO data, other models or other cloud types.

A combined CALIPSO, CloudSat and ISCCP simulator is currently under development by the Cloud Feedback Model Intercomparison Project (Phase 2) group and will enable a wider range of model users to assess their models using lidar data.

Appendix

Appendix A GLAS products and retrieval algorithm

The Geoscience Laser Altimeter System (GLAS) is a lidar onboard the Ice, Cloud and Land Elevation Satellite (ICESat). It orbits the Earth in a near-polar orbit with a ground speed of approximately 7 km/s. The instrument consists of three redundant diode pumped Nd:YAG lasers transmitting at both the fundamental (1064 nm) and doubled (532 nm) frequency with a pulse rate of 40 Hz. At full resolution (FR), the centers of the laser footprints are about 175 m apart and have a diameter of about 70 m. To improve the signal-to-noise ratio, the individual backscatter profiles can be averaged before applying the algorithm that searches for cloud and aerosol layers. At high resolution (HR/ 5Hz), eight profiles are averaged. At medium resolution (MR/ 1Hz), 40 profiles are averaged, and at low resolution (LR/ 0.25 Hz), 160 backscatter profiles are averaged. While the signal detection is improved by this averaging process, horizontal (along-track) resolution is reduced to 1.4 km/ 7 km/ 28 km for HR/ MR/ LR respectively. In addition, features of small horizontal extent that do not show up in every profile averaged can be lost in this process.

The backscatter signal detected by GLAS is digitized at a rate of 1.953 MHz, corresponding to a vertical resolution of 76.8 m. The following is a short summary of the detection algorithm for cloud and elevated aerosol layers:

The backscatter profiles are averaged to LR. The algorithm first determines a background noise threshold from the profiles. It then proceeds to search from 22 km

above ground to the surface for layers with backscatter exceeding the threshold. Consecutive samples with backscatter signal above the threshold are considered a cloud or aerosol layer. The top- and bottom-most samples above the signal threshold are the height of the layer top and base. The discrimination between cloud and aerosol layers is based on several attributes: Signal magnitude at the layer top, signal gradient throughout the layer, layer top altitude, horizontal extent and uniformity, vertical extent and uniformity, relative humidity at the height of the layer and signal attenuation. The assumption is that aerosol layers are more likely to be found close to the surface. They tend to have a weaker backscatter signal than clouds, particularly in the lower atmosphere. Aerosol layers are assumed to have less distinct layer edges, have large horizontal extent and be relatively uniform in the horizontal. The relative humidity has to be close to 100% to allow the formation of clouds. The algorithm uses a combination of these criteria to distinguish cloud layers from elevated aerosol layers. The algorithm searches for up to ten consecutive layers.

If layers are found, the same procedure is repeated for the next higher resolution. At full resolution, only the lowest 10 km of the atmosphere are searched, and only one cloud layer can be detected.

In many circumstances, the boundary layer (BL) top is marked by a sharp gradient in aerosol concentration. To find the BL top, the algorithm searches the LR profile from the ground up to 6 km for the first significant decrease in backscatter intensity. This layer is marked as the BL top. If no such decrease is found below 6 km, the search is abandoned. In places where optically thick boundary layer clouds exist, the clouds can fully attenuate the lidar signal. In this case, the first decrease of the backscatter signal

occurs at the top of the boundary layer clouds. In some cases, this cloud top can be consistent with the expected BL top, such as for marine stratocumulus clouds, but there is no guarantee that this is always the case. The ratio of the signal strength in the BL to the signal 500 m above the BL top is a measure of the retrieval quality. A large ratio indicates a very strong signal, and usually a sharp gradient. This is often the case for cloudy BLs. Clear BLs usually have a weaker ratio. If a BL top is detected at LR, the search is repeated at HR.

The optical depth of detected aerosol and cloud layers can be estimated from the attenuated backscatter profiles. The lidar signal usually becomes fully attenuated at optical depths around three.

For further detail on the GLAS algorithms, the Algorithm Theoretical Basis Document Version 4.2 can be consulted (Palm et al., 2002).

Appendix B IFS model boundary layer and convection schemes

The following is a brief summary of the boundary layer (BL) and convective schemes of the individual model runs of the ECMWF IFS:

CY28R3

The BL parameterization consists of simple K-diffusion of the dry conserved variables. Cloud processes are not included in the BL scheme. Stratocumulus clouds are produced by the shallow convection parameterization.

Convection is triggered following Jakob and Siebesma (2003) using an entraining plume model. The updraft area for the plumes is chosen as the upper 3% of the vertical motion field. Cloud water in excess of 0.5 g kg^{-1} is removed to regulate water loading. The entrainment rate for the parcel scales as inverse height. The parcel originates in the

lowest model level. An excess of heat and moisture is added to the parcel that scales with the surface fluxes. The parcel is lifted until it reaches a level of zero vertical velocity. The model level closest to the lifting condensation level encountered by the parcel is the cloud base level, the level of zero vertical motion the first guess at the cloud top level.

The convection parameterization of CY28R3 is described in Bechthold et al. (2004) and referred to as ECM throughout the paper. To summarize, three types of convection are distinguished: shallow, deep and mid-level convection. These correspond to convection types 2 (shallow), 1 (deep) and 3 (mid-level). Convection type 0 indicates that no convective parameterization is active at the model grid point.

Shallow convection is represented using a BL equilibrium closure, i.e. the mass flux depends on the moist static energy equilibrium in the BL.

For deep convection, the cloud base and top are determined iteratively. The test parcel is lifted from a 30 hPa (60 hPa) average layer just above the lowest model layer. A fixed temperature and moisture perturbation are added. If the parcel ascent results in cloud formation, the origination level of the test parcel is chosen higher, and the parcel ascent is repeated. The cloud top level is adjusted with each iteration, and corresponds to the level with zero vertical motion of the parcel. CAPE is adjusted to zero over a specified time period to close the scheme.

Mid-level convection is convection originating above 500 hPa in areas with relative humidity above 80% and upward motion. Again, the level of zero vertical motion is the cloud top level.

CY29R1

The BL parameterization in this cycle considers moist conserved variables, instead of dry conserved variables. The scheme is a mixed K-diffusion and mass flux transport scheme. The mass flux transport allows for counter-gradient transport, representing eddies with a scale comparable to the BL depth. K-diffusion is used to parameterize smaller size eddies. The BL scheme can generate layer clouds if a stability criterion is satisfied. This criterion consists of a minimum temperature jump across the BL top ($\theta_{700\ hPa}$-θ_{sfc}> 20 K). The top level the test parcel reaches must also exceed the lifting condensation level (cloud base). If the stability criterion is satisfied, the shallow or deep convection parameterizations are disallowed.

The BL scheme distinguished between these conditions: Type 0 indicates a stable boundary layer, with negative buoyancy flux at the surface; type 1 refers to a dry convective boundary layer, where the test parcel never reaches the lifting condensation level before its vertical velocity goes to zero; type 2 is the cloudy boundary layer, which produces stratocumulus-type clouds; and type 3 refers to a dry convective boundary layer underneath convection. Here, the test parcel encounters the LCL before its upward motion ceases, but the stability criterion for type 2 is not satisfied. A thorough description of this BL scheme is provided in a Scientific Advisory Committee Paper of the ECMWF (SAC).

The shallow and deep convection schemes are unchanged from CY28R3. The runs CY29R1-E and CY29R1-S are variations on CY29R1. In CY29R1-E, the test parcel

entrainment is modified (weakened) to allow the parcel to rise higher. This should lead to a deeper BL. The entrainment term is changed as follows from

CY29R1:

$$w_e = \frac{1}{\tau w_u} + \frac{1}{z} \tag{B.1}$$

where τ is a time scale of 500 s, w_u is the updraft velocity, and z is height above ground. In CY29R1-E, this formulation is modified to

$$w_e = \frac{1}{\tau w_u} \tag{B.2}$$

It can be argued that the 1/z dependency desired for w_u is already incorporated in the first term, since the upward velocity w_u approaches zero at the surface. Hence, the additional term of 1/z might be unnecessary.

In CY29R1-S, the entrainment is unchanged, but the stability criterion is relaxed to

$$\theta_{700hPa} - \theta_{sfc} < 16K \tag{B.3}$$

The value of 16 K is closer to the estimate of Klein and Hartmann (1993). This modification should allow the BL parameterization to produce clouds in areas with a weaker inversion.

References

Ahlgrimm, M., and D. A. Randall, 2006: Diagnosing Monthly Mean Boundary Layer Properties from Reanalysis Data Using a Bulk Boundary Layer Model. *J. Atmos. Sci.*, **63,** 998-1012.

Albrecht, B. A., C. S. Bretherton, D. Johnson, W. H. Schubert, and A. S. Frisch, 1995: The Atlantic Stratocumulus Transition Experiment - ASTEX. *Bull. Amer. Meteor. Soc.*, **76,** 889-904.

Astin, I., and B. G. Latter, 1998: A Case for Exponential Cloud Fields? *J. Appl. Meteor.*, **37,** 1375-1382.

Astin, I., and L. Di Girolamo, 1999: A General Formalism for the Distribution of the Total Length of the Geophysical Parameter Along a Finite Transect. *IEEE Trans. Geosci. Remote Sens.*, **37,** 508-512.

Astin, I., L. Di Girolamo, and H. M. van de Poll, 2001: Bayesian conficence intervals for true fractional coverage from finite transect measurements: Implications for cloud studies from space. *J. Geophys. Res.*, **106,** 17,303-317,310.

Augstein, E., H. Schmidt, and F. Ostapoff, 1973: The vertical structure of the atmospheric planetary boundary layer in undisturbed trade winds over the Atlantic Ocean. *Bound.-Layer Meteor.*, **6,** 129-150.

Bacmeister, J. T., M. J. Suarez, and F. R. Robertson, 2006: Rain Reevaporation, Boundary Layer-Convection Interactions, and Pacific Rainfall Patterns in an AGCM. *J. Atmos. Sci.*, **63,** 3383-3403.

Bechtold, P., J.-P. Chaboureau, A. Beljaars, A. K. Betts, M. Köhler, M. Miller, and J.-L. Redelsperger, 2004: The simulation of the diurnal cycle of convective precipitation over land in a global model. *Quart. J. Roy. Meteor. Soc.*, **130,** 3119-3137.

Bretherton, C. S., and M. C. Wyant, 1997: Moisture Transport, Lower-Tropospheric Stability, and Decoupling of Cloud-Topped Boundary Layers. *J. Atmos. Sci.*, **54,** 148-167.

Bretherton, C. S., and Coauthors, 2004: The Epic 2001 Stratocumulus Study. *Bull. Amer. Meteor. Soc.*, **85,** 967-977.

Chepfer, H., M. Chiriaco, R. Vautard, and J. D. Spinhirne, 2007: Evaluation of MM5 Optically Thin Clouds over Europe in Fall Using ICESat Lidar Spaceborne Observations. *Mon. Wea. Rev.*, **135,** 2737-2753.

Chevallier, F., P. Bauer, G. Kelly, C. Jakob, and T. McNally, 2001: Model Clouds over Oceans as Seen from Space: Comparison with HIRS/2 and MSU Radiances. *J. Climate*, **14,** 4216-4229.

Chiriaco, M., and Coauthors, 2006: The Ability of MM5 to Simulate Ice Clouds: Systematic Comparison between Simulated and Measured Fluxes and Lidar/ Radar Profiles at the SIRTA Atmospheric Observatory. *Mon. Wea. Rev.*, **134,** 897-918.

Chou, M.-D., and M. J. Suarez, 1999: A Solar Radiation Parameterization for Atmospheric Studies. *NASA TM-104606 Technical Report Series on Global Modeling and Data Assimilation*, **15,** 40.

Ciesielski, P. E., W. H. Schubert, and R. H. Johnson, 1999: Large-Scale Heat and Moisture Budgets over the ASTEX Region. *J. Atmos. Sci.*, **56,** 3241-3261.

——, 2001: Diurnal Variability of the Marine Boundary Layer during ASTEX. *J. Atmos. Sci.*, **58,** 2355-2375.

Collis, R. T., and P. B. Russel, 1976: Laser Monitoring of the Atmosphere. *Springer-Verlag.*

Deardorff, J. W., 1980: Cloud Top Entrainment Instability. *J. Atmos. Sci.*, **37,** 131-147.

Dessler, A. E., S. P. Palm, W. D. Hart, and J. D. Spinhirne, 2006a: Tropopause-level thin cirrus coverage revealed by ICESat/Geoscience Laser Altimeter System. *J. Geophys. Res.*, **111,** D082003.

Dessler, A. E., S. P. Palm, and J. D. Spinhirne, 2006b: Tropical cloud-top height distributions revealed by the Ice, Cloud and Land Elevation Satellite (ICESat)/ Geoscience Laser Altimeter System (GLAS). *J. Geophys. Res.*, **111,** D12215.

Duynkerke, P. G., and J. Teixeira, 2001: Comparison of the ECMWF Reanalysis with FIRE I Observations: Diurnal Variation of Marine Stratocumulus. *J. Climate*, **14,** 1466-1478.

Gregory, D., and P. R. Rowntree, 1990: A Mass Flux Convection Scheme with Representation of Cloud Ensemble Characteristics and Stability-Dependent Closure. *Mon. Wea. Rev.*, **118,** 1483-1506.

Hart, W. D., J. D. Spinhirne, S. P. Palm, and D. Hlavka, 2005: Height distribution between cloud and aerosol layers from the GLAS spaceborne lidar in the Indian Ocean region. *Geophys. Res. Lett.*, **32,** L22S06.

Holtslag, A. A. M., and B. A. Boville, 1993: Local Versus Nonlocal Boundary-Layer Diffusion in a Global Climate Model. *J. Climate*, **6,** 1825-1842.

Hortal, M., and A. J. Simmons, 1991: Use of reduced Gaussian grids in spectral models. *Mon. Wea. Rev.*, **119,** 1057-1074.

Jakob, C., 1999: Cloud cover in the ECMWF reanalysis. *J. Climate*, **12,** 947-959.

Jakob, C., and A. P. Siebesma, 2003: A New Subcloud Model for Mass-Flux Convection Schemes: Influence on Triggering, Updraft Properties, and Model Climate. *Mon. Wea. Rev.*, **131,** 2765-2778.

Khairoutdinov, M., and Y. Kogan, 2000: A New Cloud Physics Parameterization in a Large-Eddy Simulation Model of Marine Stratocumulus. *Mon. Wea. Rev.*, **128,** 229-243.

Klein, S. A., and D. L. Hartmann, 1993: The Seasonal Cycle of Low Stratiform Clouds. *J. Climate*, **6,** 1587-1606.

Koster, R. D., M. J. Suarez, A. Ducharne, M. Stieglitz, and P. Kumar, 2000: A catchment-based approach to modeling land surface processes in a general circulation model. !. Model structure. *J. Geophys. Res.*, **105,** 24809-24822.

Lenschow, D. H., and Coauthors, 1988: Dynamics and Chemistry of Marine Stratocumulus (DYCOMS) Experiment. *Bull. Amer. Meteor. Soc.*, **69,** 1058-1067.

Lin, S.-J., and R. B. Rood, 1996: Multidimensional Flux-Form Semi-Lagrangian Transport Schemes. *Mon. Wea. Rev.*, **124,** 2046-2070.

Lock, A. P., A. R. Brown, M. R. Bush, G. M. Martin, and R. N. B. Smith, 2000: A New Boundary Layer Mixing Scheme. Part I: Scheme Description and Single-Column Model Tests. *Mon. Wea. Rev.*, **128,** 3187-3199.

Mahesh, A., M. A. Gray, S. P. Palm, W. D. Hart, and J. D. Spinhirne, 2004: Passive and active detection of clouds: Comparisons between MODIS and GLAS observations. *Geophys. Res. Lett.*, **31,** L04108.

McGauley, M., C. Zhang, and N. A. Bond, 2004: Large-Scale Characteristics of the Atmospheric Boundary Layer in the Eastern Pacific Cold Tongue/ITCZ Region. *J. Climate*, **17,** 3907-3920.

Menzel, W. P., R. A. Frey, B. A. Baum, and H. Zhang, 2006: MODIS cloud top properties and cloud phase, Algorithm Theoretical Basis Document, Version 7.

Miller, S. D., G. L. Stephens, and A. C. M. Beljaars, 1999: A Validation Survey of the ECMWF Prognostic Cloud Scheme using LITE. *Geophys. Res. Lett.*, **26,** 1417-1420.

Minnis, P., P. W. Heck, D. F. Young, C. W. Fairall, and J. B. Snider, 1992: Stratocumulus Cloud Properties Derived from Simultaneous Satellite and Island-based Instrumentation during FIRE. *J. Appl. Meteor.*, **31,** 317-339.

Moorthi, S., and M. J. Suarez, 1992: Relaxed Arakawa-Schubert. A Parameterization of Moist Convection for General Circulation Models. *Mon. Wea. Rev.*, **120,** 978-1002.

Naud, C. M., J.-P. Muller, E. E. Clothiaux, B. A. Baum, and W. P. Menzel, 2005: Intercomparison of multiple years of MODIS, MISR and radar cloud-top heights. *Ann. Geophysicae*, **23,** 2415-2424.

Neiburger, M., D. S. Johnson, and C. W. Chien, 1961: Studies of the structure of the atmosphere over the Eastern Pacific Ocean in summer, I, The inversion over the Eastern Nort Pacific Ocean. *Univ. Calif. Publ. Meteor.*, **1**.

Ou, S.-C., and K.-N. Liou, 1995: Ice microphysics and climatic temperature feedback. *Atmos. Res.*, **35,** 127-138.

Palm, S. P., W. Hart, D. Hlavka, E. J. Welton, A. Mahesh, and J. D. Spinhirne, 2002: Algorithm Theoretical Basis Document Version 4.2.

Palm, S. P., A. Benedetti, and J. D. Spinhirne, 2005: Validation of ECMWF global forecast model parameters using GLAS atmosperic channel measurements. *Geophys. Res. Lett.*, **32**.

Platt, C. M. R., 1973: Lidar and Radioimetric Observations of Cirrus Clouds. *J. Atmos. Sci.*, **30,** 1191-1204.

Räisänen, P., H. W. Barker, M. Khairoutdinov, J. Li, and D. A. Randall, 2004: Stockastic generation of subgrid-scale cloudy columns for large-scale models. *Quart. J. Roy. Meteor. Soc.*, **130,** 2047-2067.

Randall, D. A., 1980: Conditional Instability of the First Kind Upside-Down. *J. Atmos. Sci.*, **37,** 125-130.

Rauber, R. M., and Coauthors: Rain in (Shallow) Cumulus over the Ocean - The RICO Campaign. *submitted Bull. Amer. Meteor. Soc.*

SAC, 2004: Review of moist physical processes in the IFS. *ECMWF Scientific Advisory Committee, 32rd Session, Item 7.1.*

Schaefer, J. T., 1990: The Critical Success Index as an Indicator of Warning Skill. *Wea. Forecasting*, **5,** 570-575.

Spinhirne, J. D., S. P. Palm, W. D. Hart, D. Hlavka, and E. J. Welton, 2005: Cloud and aerosol measurements from GLAS: Overview and initial results. *Geophys. Res. Lett.*, **32,** L22S03.

Stevens, B., and Coauthors, 2003: Dynamics and Chemistry of Marine Stratocumulus - DYCOMS-II. *Bull. Amer. Meteor. Soc.*, **84,** 579-593.

Ulaby, F. T., R. K. Moore, and A. K. Fung, 1943: Microwave Remote-Sensing Active and Passive. *Microwave Remote-Sensing Fundamentals and Radiometry. Artech House*, **Vol. 1**.

Wang, L., and A. E. Dessler, 2006: Instantaneous cloud overlap statistics in the tropical area revealed by ICESat/GLAS data. *Geophys. Res. Lett.*, **33,** L15804.

Wielicki, B. A., and J. A. Coakley Jr., 1981: Cloud retrieval using infrared sounder data: Error analysis. *J. Appl. Meteor.*, **20,** 157-169.

Wilkinson, J. M., R. Hogan, J., A. J. Illingworth, and A. Benedetti: Use of a Lidar Forward Model for Global Comparisons of Cloud Fraction between the ICESat Lidr and the ECMWF Model. *submitted Mon. Wea. Rev.*

Winker, D. M., R. H. Couch, and M. P. McCormick, 1996: An overview of LITE: NASA's Lidar in-space Technology Experiment. *Proc. IEEE*, **84,** 164-180.

Wood, R., and C. S. Bretherton, 2004: Boundary Layer Depth, Entrainment, and Decoupling in the Cloud-Capped Subtropical and Tropical Marine Boundary Layer. *J. Climate*, **17,** 3576-3588.

Wyant, M. C., C. S. Bretherton, H. A. Rand, and D. E. Stevens, 1997: Numerical Simulations and a Conceptual Model of the Stratocumulus to Trade Cumulus Transition. *J. Atmos. Sci.*, **54,** 168-192.

Wylie, D. P., E. Eloranta, J. D. Spinhirne, and S. P. Palm, 2007: A Comparison of Cloud Cover Statistics from the GLAS Lidar with HIRS. *J. Climate*, **20,** 4968-4891.

Zhang, C., M. McGauley, and N. A. Bond, 2004: Shallow Meridional Circulation in the Tropical Eastern Pacific. *J. Climate*, **17,** 133-139.

Zwally, H.J., R. Schutz, S. Palm, W. Hart, S. Hlavka, J. Spinhirne, and E. Welton. 2003a. *GLAS/ICESat L2 Global Cloud Heights for Multilayer Clouds V026*, 15 October to 18 November 2003. Boulder, CO: National Snow and Ice Data Center. Digital media.

Zwally, H.J., R. Schutz, S. Palm, W. Hart, S. Hlavka, J. Spinhirne, and E. Welton. 2003b. *GLAS/ICESat L2 Global Planetary Boundary Layer & Elevated Aerosol Layer Heights V026*, 15 October to 18 November 2003. Boulder, CO: National Snow and Ice Data Center. Digital media.